

UNCLASSIFIED
AD 411996

DEFENSE DOCUMENTATION CENTER
FOR
SCIENTIFIC AND TECHNICAL INFORMATION
CAMERON STATION, ALEXANDRIA, VIRGINIA



UNCLASSIFIED

NOTICE: When government or other drawings, specifications or other data are used for any purpose other than in connection with a definitely related government procurement operation, the U. S. Government thereby incurs no responsibility, nor any obligation whatsoever; and the fact that the Government may have formulated, furnished, or in any way supplied the said drawings, specifications, or other data is not to be regarded by implication or otherwise as in any manner licensing the holder or any other person or corporation, or conveying any rights or permission to manufacture, use or sell any patented invention that may in any way be related thereto.

411996

CATALOGED BY DDC

AS AD No.

411996

63-4-4

A STUDY OF
THE FLUID DYNAMICS AND HEAT TRANSFER BEHAVIOR
FOR RADially INWARD FLOW OVER A
SHROUDED ROTATING DISC

BY

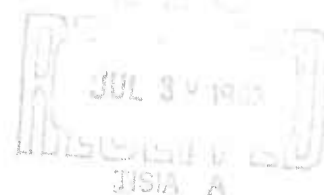
J. W. MITCHELL

TECHNICAL REPORT NO. 57

PREPARED UNDER CONTRACT Nonr 225 (23)
(NR-090-342)
FOR
OFFICE OF NAVAL RESEARCH

DEPARTMENT OF MECHANICAL ENGINEERING
STANFORD UNIVERSITY
STANFORD, CALIFORNIA

APRIL 30, 1963



A STUDY OF THE FLUID DYNAMICS AND HEAT TRANSFER
BEHAVIOR FOR RADially INWARD FLOW OVER A
SHROUDED ROTATING DISK

Technical Report No. 57

Prepared under Contract Nonr 225(23)
(NR-090-342)

For
Office of Naval Research

Reproduction in whole or part is permitted for
any purpose of the United States Government

Department of Mechanical Engineering
Stanford University
Stanford, California

April 30, 1963

Report Prepared By:

J. W. Mitchell

Approved By:

A. L. London

Project Supervisor

ABSTRACT

The present investigation is a study of the modeling of radial flow gas turbine fluid dynamics and heat transfer behavior. A test facility has been constructed for the modeling of turbine flows. Several unconventional experimental techniques have been developed for use in the facility.

A simple model of a radial flow gas turbine has been analyzed and tested. The fluid dynamics and heat transfer behavior of a single radially inward flow of air over a shrouded rotating disk has been experimentally determined. The fluid dynamics behavior is presented as a series of graphs detailing the velocity profiles. The heat transfer is correlated over the operating range of radial flow gas turbines by a simple algebraic relation between the governing nondimensional parameters. An analysis is presented that does not adequately predict the heat transfer. The reasons for the discrepancy between analysis and experiment are discussed.

ACKNOWLEDGEMENTS

The author expresses his gratitude to the Office of Naval Research and to the AiResearch Manufacturing Division of the Garrett Corporation for making possible his graduate study program. Professor A. L. London directed the Stanford investigation. His innumerable ideas and advice are sincerely appreciated. Dr. W. T. Von der Nuell started the project with the Office of Naval Research sponsorship and directed a parallel investigation using actual turbomachinery at AiResearch. Work at AiResearch was done by Dr. J. E. Coppage and Mr. W. U. Rossler. This program contributed materially to the present investigation.

The concept of the garter spring pickup originated with Mr. W. A. Casler, of Aerojet General Corporation, who has graciously helped in developing the pickup for the present application. The design, construction, and testing of the selector switch-pickup assembly was undertaken by Mr. Kosa Miwa, a Japanese engineer studying at Stanford during the 1960-61 school year. In the final stages of the project, Mr. D. E. Metzger assisted with the data taking.

The test facility owes its existence to the efforts of Mr. T. Ikebe, Mr. F. McKinley, and Mr. G. Yoshida, mechanics at Stanford. They have contributed many helpful suggestions concerning the design of the facility, and carried out its construction and assembly.

TABLE OF CONTENTS

	Page
References	x
Nomenclature	xiii
 I Introduction	 1
 II Summary of Work of Previous Investigators	
A. Heat Transfer from Unshrouded Rotating Disks	4
B. Heat Transfer from Shrouded Rotating Disks	7
C. Heat Transfer in Veil-flows	8
 III Governing Nondimensional Parameters	 12
 IV Test Facility	
A. Description of Test Facility	17
B. Rotating Disk	19
C. Inlet Velocity Control	22
D. Infrared Heating System	23
E. Selector Switch and Garter Spring Pickup	24
F. Flow System	26
G. Fluid Dynamics Instrumentation	27

	Page
V Experimental Results	
A. Radial Inflow Flow Results	33
B. Radial Inflow Heat Transfer Results	58
C. Radial Outflow Heat Transfer Results	71
VI Analytical Investigation	78
A. Behavior of the Fluid External to the Boundary Layers	80
B. Hydrodynamic Solution	83
C. Heat Transfer Solution	89
D. Effect of Shroud-to-Disk Spacing on Heat Transfer	96
E. Conclusions	99
VII Discussion of Results	101
VIII Conclusions	107
IX Recommendations for Further Work	108
X Appendices	
Appendix A Experimental Uncertainties	109
Appendix B Fluid Velocity Measurement Errors	113
Appendix C Data Reduction Procedures	116
Appendix D Local Heat Flux Data Reduction	124

	Page
Appendix E Heat Meter Calibration	136
Appendix F Derivation of Integral Equations	140

LIST OF TABLES

I. Radial Inflow Heat Transfer Data	70
II. Radial Outflow Heat Transfer Data	77
III. Analytical Radial Inflow Heat Transfer Results	96

LIST OF FIGURES

Figure		Page
1	Rotating Disk Coordinate System and Geometries	10
2	Comparison of Heat Transfer Results for Unshrouded Rotating Disk Heat Transfer	11
3	Schematic of Rotating Disk Test Facility	29
4	Rotating Disk Test Facility	29
5	Schematic of Disk Cross Section and Instrument Location	30
6	Disk Test Surface and Rotating Screens	30
7	Schematic of Test Facility Inlet Passage	30
8	Infrared Heating System	30
9	Schematic of the Selector Switch and Garter Spring Pickup Assembly	31
10	Cross Section Through Selector Switch and Garter Spring Pickup	31
11	Selector Switch and Garter Spring Pickup Mounted on Disk Drive Shaft	31
12	Shroud and Vaned Diffuser	32
13	Directional Probe and Traversing Mechanism	32
Fluid Velocity Component and Flow Angle Profiles		
14	$N_{R,M}/N_{R,F} = 0.056$	43
15	$N_{R,M}/N_{R,F} = 0.28$	44
16	$N_{R,M}/N_{R,F} = 0.61$	45
17	$N_{R,M}/N_{R,F} = 1.20$	46

		Page
18	$N_{R,M}/N_{R,F} = 1.56$	47
19	Three-Dimensional Velocity Profile Representation	48
20	Flow Pattern Illustrating Backflow in the Center of the Flow Passage	48
21	Fluid Angular Momentum Flux	49
	Resultant Velocity and Flow Angle Profile Variation with Circumferential Position	
22	$N_{R,M}/N_{R,F} = 0.056$	50
23	$N_{R,M}/N_{R,F} = 0.28$	51
24	$N_{R,M}/N_{R,F} = 0.61$	52
25	$N_{R,M}/N_{R,F} = 1.20$	53
26	Tangential Velocity Variation with Circumferential Position	54
	Nondimensional Velocity and Flow Angle Profile Variation with $N_{R,F}$	
27	$N_{R,M}/N_{R,F} = 0.30$	55
28	$N_{R,M}/N_{R,F} = 1.22$	56
29	Wall Static Pressure Variation with Radial Position	57
30	Average Heat Transfer Results for Radial Inflow $N_{St} N_{R,F}^{0.2}$ as a Function of $N_{R,M}/N_{R,F}$	67
31	Average Heat Transfer Results for Radial Inflow N_{St} as a Function of $N_{R,F}$	67

	Page
32 Average Heat Transfer Results for Radial Inflow $N_{St} N_{R,F}^{0.55}$ as a Function of $N_{R,M}/N_{R,F}$	68
33 Local Heat Transfer Results for Radial Inflow	69
34 Comparison of Average Heat Transfer Results for Radial Outflow N_{Nu} as a Function of $N_{R,F}$	76
35 Average Heat Transfer Results for Radial Outflow N_{Nu} as a Function of the Correlation Parameter K	76
36 Predicted Flow Paths with Respect to the Disk	100
37 Analytical Hydrodynamic Solution	100
38 Analytical Heat Transfer Solution	100
 E - 1 Heat Meter Calibration Factor, K, as a Function of Heat Meter Temperature	 139

REFERENCES

1. American Society of Mechanical Engineers Power Test Codes, Chapter 4, "Flow Measurement", New York, 1959.
2. Cobb, E. C., and Saunders, O. A., "Heat Transfer from a Rotating Disk", Proceedings of the Royal Society (London), Series A, No. 236, 1956, p. 343.
3. Davies, D. R., "On the Calculation of Eddy Viscosity and Heat Transfer in a Turbulent Boundary Layer near a Rapidly Rotating Disk", Quarterly Journal of Mechanics and Applied Mathematics, Vol. XII, Part 2, May 1959, p. 211.
4. Dorfman, L. A., "Heat Transfer from a Rotating Disk", Inzhenernofizicheskii Zhurnal, Vol. 1, No. 6, June 1958, p. 3 (in Russian).
5. Eckert, E. R. G., and Diaguila, A. J., "Convection Heat Transfer for Mixed, Free, and Forced Flow Through Tubes", Transactions ASME, Vol. 76, p. 496, 1954.
6. Goldsmith, A., Waterman, T. E. and Hirschorn, H. J., "Handbook of Thermophysical Properties of Solid Materials", Armour Research Institute, Permagon Press, New York, 1962.
7. Hartnett, J. P., Birkebak, R. C., and Eckert, E. R. G., "Velocity Distributions, Temperature Distributions, Effectiveness, and Heat Transfer for Air Injected Through a Tangential Slot Into a Turbulent Boundary Layer", Transactions ASME, Series C, August 1961, p. 293.
8. von Karman, Th., "On Laminar and Turbulent Friction", NACA T. M. 1092, 1946.
9. Keenan, J. H., and Kaye, J., "Gas Tables", John Wiley and Sons, Inc., New York, 1954.
10. Kreith, F., Doughman, E., and Kozlowski, H., "Mass and Heat Transfer From an Enclosed Rotating Disk With and Without Source Flow", ASME Paper 62 - HT - 20.
11. Kreith, F., and Taylor, J. H., "Heat Transfer from a Rotating Disk in Turbulent Flow", ASME Paper 56 - A - 146, Nov. 1956.

12. Kreith, F., Taylor, J. H. and Chong, J. P., "Heat and Mass Transfer from a Rotating Disk", Transactions ASME, Vol. 81, Series C, No. 2, May 1959, p. 95.
13. Millsaps, K., and Pohlhausen, K., "Heat Transfer by Laminar Flow from a Rotating Disk", Journal of Aeronautical Sciences, Vol. 19, 1952, p. 120.
14. Nicoll, W. B., and Kays, W. M., "The Influence of Temperature Dependent Properties on Gas Flow Heat Transfer in Circular Tubes", Dept. of Mech. Engr. TR No. 43, Stanford University, Sept. 1959.
15. Relton, F. E., "Applied Bessel Functions", Blackie and Son Limited, London, 1949.
16. Rossler, W. U., and Mitchell, J. W., "Investigation of Veil Cooling for Radial Flow Turbines", AiResearch Manufacturing Division, The Garrett Corp., AiResearch Report No. K - 451 - R, May 1961.
17. Schlichting, H., "Boundary Layer Theory", McGraw-Hill Book Co., New York, 1955.
18. Seban, R. A., "Heat Transfer and Effectiveness for a Turbulent Boundary Layer with Tangential Fluid Injection", Transactions ASME, Series C, Vol. 82, 1960, p. 389.
19. Smith, R. D., "Heat Transfer in a Cooled Radial Flow Turbine with an Aluminum Rotor", Purdue Gas Turbine Laboratory Report I - 56 - 1, Feb. 1956.
20. Soo, S. L., "Flow Over an Enclosed Rotating Disk", Transactions ASME, Vol. 80, 1958, p. 287.
21. Soo, S. L., Besant, R. W., and Sarafa, Z. N., "The Nature of Heat Transfer from an Enclosed Rotating Disk", M.E. Technical Note 9725 - 3, Engineering Experiment Station, University of Illinois, Jan. 1961.
22. Wagner, C., "Heat Transfer from a Rotating Disk to Ambient Air", Journal of Applied Physics, Vol. 19, 1948, p. 837.

23. Zaloudek, F. R., "An Investigation of the Heat Transfer and Recovery Factors for a Rotating Disk", PhD Thesis, Purdue University, 1959.
24. Bjorklund, I. S., and Kays, W. M., "Heat Transfer Between Concentric Rotating Cylinders", Transactions ASME, Vol. 81, Series C, No. 3, 1959, p. 175.

NOMENCLATURE

English Letter Symbols:

C_p	fluid specific heat, BTU/lb F
g	gravitational acceleration, ft/sec ²
h	average heat transfer coefficient, BTU/hr ft ² F
$J_n(x)$	nth order Bessel function of first kind with argument x
K	correlation parameter defined by Eq. [17] heat meter calibration factor, $\frac{(\text{BTU/hr ft}^2)}{mv}$
k	thermal conductivity, BTU/(hr ft ² F/ft)
p	fluid pressure, #/in ²
q''	average heat flux, BTU/hr ft ²
r	radial coordinate, ft
r_o	disk radius, ft
T	temperature, R
t	temperature, F
u	fluid radial velocity component, ft/sec
V	fluid resultant velocity, ft/sec
v	fluid tangential velocity component, ft/sec
W	mass flow rate, lb/hr
w	fluid axial velocity component, ft/sec
z	axial coordinate, ft
z_o	disk-to-shroud spacing, ft

Greek Letter Symbols:

α	thermal diffusivity, ft^2/sec
α_m	eigenvalues, zeros of $J_1(x)$
β	Reynolds number ratio; air coefficient of thermal expansion, $1/F$
δ	hydrodynamic boundary layer thickness, ft
Δ	thermal boundary layer thickness, ft
ϵ_H	eddy diffusivity for heat, ft^2/sec
ϵ_M	eddy diffusivity for momentum, ft^2/sec
η	dummy variable of integration
θ	tangential coordinate, radians
μ	fluid dynamic viscosity, lb/hr ft
ν	fluid kinematic viscosity, ft^2/sec
ρ	fluid density, lb/ft^3
τ	shear stress, \#/ft^2
ω	disk angular velocity, rad/sec

Nondimensional Parameters:

$$N_{Gr} = \frac{g \beta r_o^3 \rho^2 (\Delta t)}{\mu^2}, \text{ Grashof number}$$

$$N_{Nu} = \frac{h r_o}{k}, \text{ average Nusselt number}$$

$$N_{R,F} = \frac{W}{z_o \mu}, \text{ mass flow Reynolds number}$$

$$N_{R,M} = \frac{r_o^2 \omega \rho}{\mu}, \text{ machine Reynolds number}$$

$$N_{St} = \frac{h}{\left(\frac{W}{2\pi r_o z_o}\right) C_p}, \text{ average Stanton number}$$

$$N_{St,l} = \frac{h_l}{\left(\frac{W}{2\pi r_o z_o}\right) C_p}, \text{ local Stanton number}$$

$$r^* = \frac{r}{r_o}, \text{ nondimensional radial coordinate}$$

$$z^* = \frac{z}{r_o}, \text{ nondimensional axial coordinate}$$

$$z_o^* = \frac{z_o}{r_o}, \text{ nondimensional disk-to-shroud spacing}$$

$$\beta = \frac{2\pi N_{R,M}}{N_{R,F}}, \text{ ratio of machine Reynolds number to mass flow Reynolds number}$$

$$\delta^* = \frac{\delta}{r_o}, \text{ nondimensional hydrodynamic boundary layer thickness}$$

$$\Delta^* = \frac{\Delta}{r_o}, \text{ nondimensional thermal boundary layer thickness}$$

$$\sigma = \frac{\Delta}{\delta}, \text{ boundary layer thickness ratio}$$

Subscripts:

r denotes value in the radial direction

R denotes relative, evaluated with respect to the rotating disk

δ denotes value at the edge of the hydrodynamic boundary layer

in denotes fluid inlet value
l denotes local value as opposed to the average value

Superscripts:

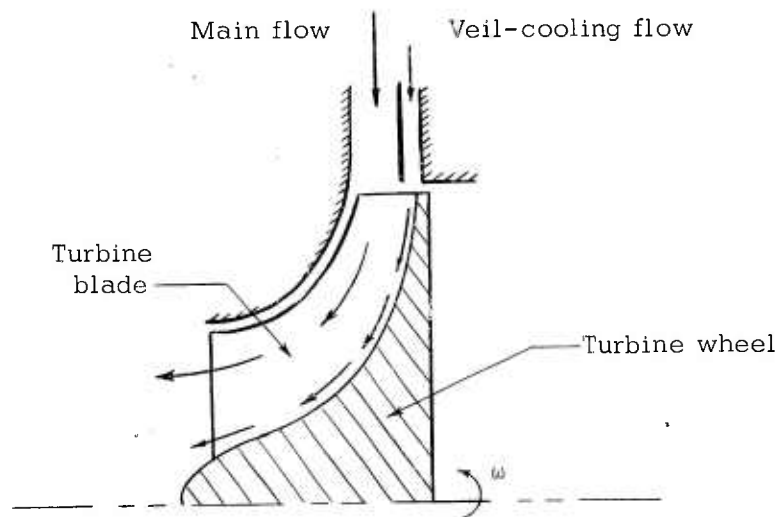
* denotes a nondimensional quantity

Miscellaneous

denotes pounds force
lb denotes pounds mass
 Δ on t denotes a temperature difference

I INTRODUCTION

In recent years there have been increasing applications of radial flow gas turbines as prime mover and auxiliary power sources in the aircraft and automotive industries. High performance levels in these units are attained with high turbine inlet temperatures. These high temperatures necessitate the use of high temperature alloys in the turbine wheels. A proposed method of reducing the metallurgical requirements is to insulate the turbine wheel from the hot gas stream by a veil-flow blanket of cold air, as shown in the following figure:



A heat transfer investigation of the veil-flow method has been undertaken jointly by the AiResearch Manufacturing Division of the Garrett Corporation, Los Angeles, California, and by Stanford University. AiResearch has conducted a prototype study of a veil-cooled

radial flow turbine (16)¹. The present investigation is concerned with model studies of radial flow turbines.

The present model consists of a shrouded rotating disk to which vanes may be added. The main air stream flows radially inward from the disk periphery. The veil-flow is introduced next to the disk at the periphery, and also flows radially inward. The disk and veil-flow are heated relative to the colder main stream. The heat transfer results obtained from the model tests will be extended to radial flow turbines where the main flow is hot relative to the colder disk and veil-flow.

Because of the complex flow and heat transfer behavior expected in the veil-flow studies, the initial investigation is concerned with a single air stream flowing radially inward over a shrouded unvaned rotating disk. The fluid dynamics and heat transfer behavior for this model will serve as a datum for the later investigations.

The study of a shrouded rotating disk is also of general interest. Many heat transfer studies have been conducted on unshrouded disks, and several on shrouded disks with radial outflow. The present investigation is another phase of the rotating disk problem.

The present investigation has as its specific objectives to:

1. Design, construct, instrument, and evaluate a test facility

¹Numbers in parentheses refer to references.

for determining the fluid dynamics and heat transfer behavior of a rotating disk for various flow configurations.

2. Analytically and experimentally obtain the fluid dynamics and heat transfer behavior for a single radial inflow of air over a shrouded unvaned rotating disk.

The present investigation has satisfied the first objective and, to some extent, the second. A test facility has been constructed that allows testing of various rotating disk flow configurations. Several unconventional experimental techniques have been developed. The disk is heated by a controlled infrared radiation source. Heat meters are used to measure the heat flow through the disk. A novel method of transferring the thermocouple and heat meter electrical outputs from the rotating disk to stationary recording instruments has been developed.

The rotating disk fluid dynamics and heat transfer behavior has been experimentally determined over the operating range of radial flow gas turbines. The flow pattern is unexpectedly complex, showing a strong influence of the presence of the disk and the shroud. The heat transfer results are correlated by a simple algebraic relation between the governing nondimensional parameters. An analytical attempt to predict the heat transfer is also presented. The discrepancies between analysis and experiment are discussed.

II SUMMARY OF WORK OF PREVIOUS INVESTIGATORS

A survey of the available literature pertinent to the model study was undertaken to help satisfy the project objectives. Considerable information exists for heat transfer from unshrouded disks, but very little for shrouded disks. There is also some information on heat transfer in veil-flows over flat plates which may possibly be extended to veil-flows over rotating disks. A comparison of the analytical heat transfer results in the literature has proved helpful in evaluating the various analytical methods.

A. Heat Transfer from Unshrouded Rotating Disks

Numerous studies of the heat transfer from an isothermal unshrouded rotating disk to an infinite medium have been conducted. The unshrouded disk geometry and flow pattern is shown in Fig. 1, and the heat transfer results are summarized in Fig. 2. The experimental laminar heat transfer results of Cobb and Saunders (2) and Kreith, Taylor, and Chong (12) are in good agreement with the analytical results of Dorfman (4), Millsaps and Pohlhausen (13), and Wagner (22). The experimental results of (2) are obtained directly from a heated disk, while those of (12) are established by applying the heat and mass transfer analogy to the mass transfer from a naphthalene disk. The agreement between analysis and experiment in the laminar regime establishes confidence in the experimental

results in the turbulent regime.

As shown in Fig. 2, there is considerable disagreement in the turbulent regime between the analytical attempts of Davies (3), Dorfman (4), and Kreith and Taylor (11), and the experimental results of Cobb and Saunders (2), Kreith, Taylor, and Chong (12), and Zaloudek (23). It should be noted that all of the experimental results contain the effect of a laminar core at the disk center; the flow does not become turbulent until a local Reynolds number, $(r^2 \omega \rho / \mu)$, of 2×10^5 is reached. At a machine Reynolds number of 10^6 , the flow is turbulent over 80% of the disk surface. As the analytical solutions are for turbulent flow over the entire disk, the experimental results should approach the analyses as $N_{R,M}$ increases.

The result of Davies (3) was obtained from an integral analysis using a very approximate evaluation of the heat and momentum diffusivities. The analysis of Dorfman (4) is based on the von Karman analogy, where the universal velocity profile for turbulent boundary layer flows is assumed and the turbulent diffusivities for heat and momentum are equated. Kreith and Taylor (11) present two analyses. Their integral analysis result is obtained from the integrated energy equation. The hydrodynamic and thermal boundary layer thicknesses are assumed equal. The analytical hydrodynamic solution of von Karman (8) is employed. In their Reynolds analogy result, the sum

of the laminar and turbulent diffusivities for heat and momentum is assumed equal over the entire boundary layer. The Stanton number is thus equal to one-half the friction factor. All of the analytical solutions are of the same form, $N_{Nu} = C N_{R,M}^{0.8}$, with the value of C dependent on the analysis employed.

The data of Cobb and Saunders (2) and Kreith, Taylor, and Chong (12) are in good agreement. The results of Zaloudek (23) are obtained for a constant heat flux surface condition. On the basis of turbulent flat plate heat transfer experience, the heat transfer coefficients for constant heat flux would be expected to be about 5 per cent higher than those for constant surface temperature, instead of 15 to 20 per cent higher as reported.

The analysis of Dorfman (4) and the Reynolds analogy result of Kreith and Taylor (11) compare best with the experimental results. The analysis of (4) is the most thorough and the assumptions made concerning the velocity profiles and the diffusivities are the most plausible. In both of the results of (11), the hydrodynamic and thermal boundary layer thicknesses are assumed equal. This is evidently a poor assumption for the integral method approach, and casts doubts on the accuracy of either method when applied to the shrouded disk problem. The relation of Davies (2) is in disagreement due to an inaccurate representation of the eddy diffusivity.

The best analytical approach to use in solving shrouded rotating disk problems appears to be the von Karman analogy approach. However, this is the most complicated mathematically. If the proper relation between the hydrodynamic and thermal boundary layer thicknesses could be found to make the results of the two methods compatible, both results of (11) would probably lie closer to the data. Unfortunately, this approach is mathematically impossible for the $1/7$ th power profiles chosen; however, it is possible for cases involving a shrouded disk. The general conclusions from this comparison are that if reasonable velocity and temperatures profiles are chosen, all methods determine the Reynolds number dependency to the correct power and evaluate the constant to within an order of magnitude. For the shrouded disk problem, a combination of the Reynolds analogy and integral method approaches was employed.

B. Heat Transfer from Shrouded Rotating Disks:

Considerably less information is available for shrouded rotating disks. Soo (20) has determined analytically the laminar flow pattern for radial in- and outflow, and Soo, Besant, and Sarafa (21) have analyzed the corresponding heat transfer. Kreith, Doughman, and Kozlowski (10) have determined the shrouded disk radial outflow heat transfer experimentally using the analogy between heat and mass transfer. Smith (19) has experimentally evaluated the heat transfer from a shrouded disk both for turbulent radial in- and outflow, but

the accuracy of the results is questionable due to the experimental technique employed. A comparison of the present radial outflow results with those of (10) and (19) is presented in Fig. 34.

C. Heat Transfer in Veil-flows

The AiResearch investigation of a veil-cooled radial flow turbine is summarized in (16). Temperatures on the turbine wheel were measured, and the veil-cooling flow temperature effectiveness was established. Sizable turbine wheel temperature reductions were obtained for low veil-cooling flows relative to the main flow. It is hoped that the veil-flow model studies will provide a more complete understanding of these results.

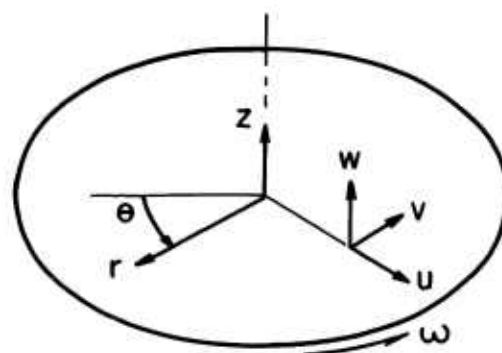
There have been several experimental heat transfer investigations of turbulent veil-flows over flat plates. Seban (18) reports temperature decays for a heated veil-flow bounded by an adiabatic wall and a cold free stream. Heat transfer coefficients for the heat transfer between a constant heat flux wall and a veil-flow for various veil-flow-to-main-stream velocity ratios and for equal initial veil and main stream temperatures are also presented. Hartnett, Birkebak, and Eckert (7) summarize and compare the temperature decay results of several investigators. Heat transfer coefficients for the heat transfer between a constant heat flux wall and a veil-flow with various ratios of veil-to-main-stream temperature for a fixed velocity

are also presented. These results will be of value in helping interpret the experimental veil-flow results and in formulating analyses.

FIGURE 1

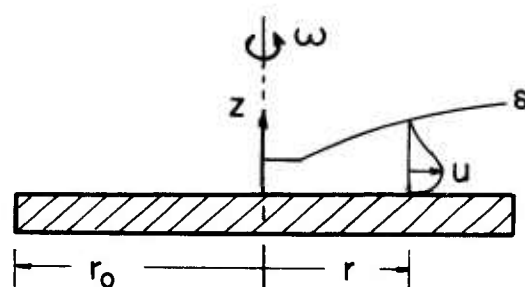
ROTATING DISK COORDINATE SYSTEM
AND GEOMETRIES

- (a) ROTATING DISK COORDINATE SYSTEM
- (b) COORDINATE SYSTEM AND FLOW PATTERN
FOR AN UNSHROUDED ROTATING DISK
WITH RADIAL OUTFLOW
- (c) COORDINATE SYSTEM AND FLOW PATTERN
FOR A SHROUDED ROTATING DISK
WITH RADIAL INFLOW

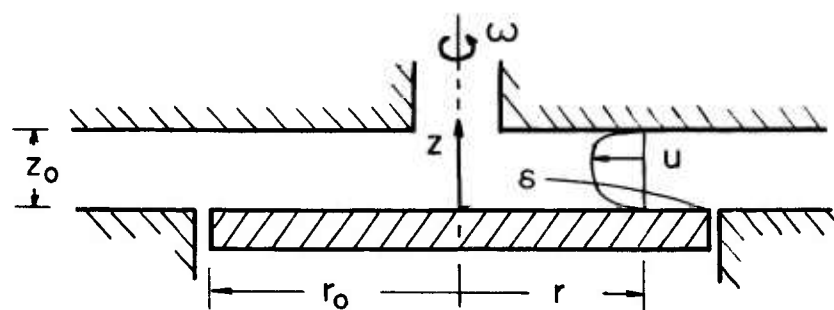


$u, v,$ AND w ARE
FLUID VELOCITIES

(a)



(b)



(c)

FIGURE 2
COMPARISON OF HEAT TRANSFER RESULTS
FOR UNSHROUDED ROTATING DISK HEAT
TRANSFER

Average Nusselt number N_{Nu} plotted as a function of machine Reynolds number $N_{R,M}$. The numbers in parentheses correspond to the references from which the heat transfer results are taken.

Laminar Regime:

- (2) Cobb and Saunders, experimental
- (4) Dorfman, analytical
- (12) Kreith, Taylor, and Chong, experimental
- (13) Millsaps and Pohlhausen, analytical
- (22) Wagner, analytical

Turbulent Regime:

- (2) Cobb and Saunders, experimental
- (3) Davies, analytical
- (4) Dorfman, analytical
- (11) Kreith and Taylor, analytical
- (12) Kreith, Taylor, and Chong, experimental
- (23) Zaloudek, experimental

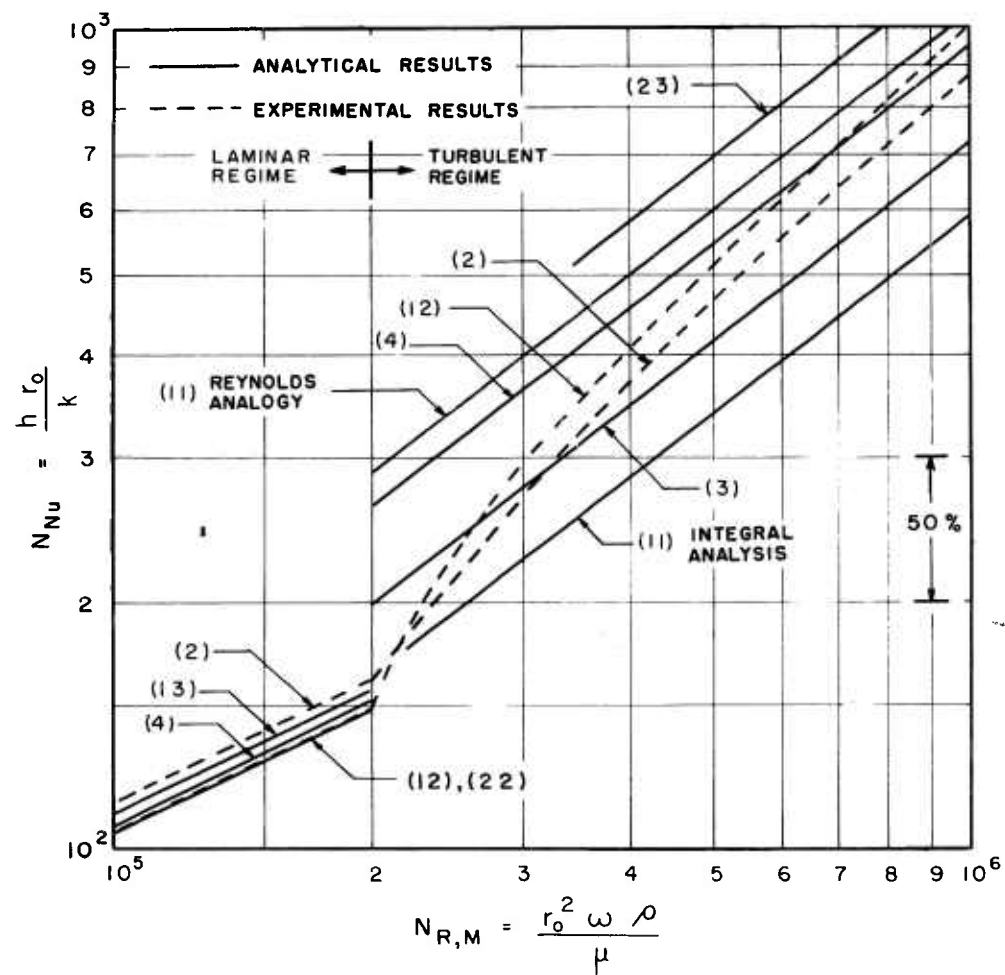


FIG.2

III GOVERNING NONDIMENSIONAL PARAMETERS

The ultimate aim of the present project is to model radial flow gas turbine heat transfer behavior. To correlate the model and prototype behavior, the correspondence between the governing nondimensional parameters of each field must be established. The gas turbine parameters are established in the literature. The rotating disk parameters must be determined from the governing differential equations and boundary conditions.

The rotating disk coordinate system is shown in Fig. 1. The differential equations and boundary conditions are written for a stationary control volume located in the fluid. The disk-to-shroud spacing is assumed small, so that the fluid pressure is a function of radius only. The heat transfer is assumed to be in the axial direction only. The fluid entering at the disk periphery is assumed to have one-dimensional velocity and temperature profiles. The fluid and disk tangential velocities are equal at the disk periphery.

Continuity equation:

$$\frac{\partial u}{\partial r} + \frac{u}{r} + \frac{\partial w}{\partial z} = 0 \quad [1]$$

Momentum equation in the radial direction:

$$u \frac{\partial u}{\partial r} + w \frac{\partial u}{\partial z} - \frac{v^2}{r} = \gamma \frac{\partial^2 u}{\partial z^2} - \frac{g_c}{\rho} \cdot \frac{dp}{dr} \quad [2]$$

Momentum equation in the tangential direction:

$$u \frac{\partial v}{\partial r} + w \frac{\partial v}{\partial z} + \frac{uv}{r} = v \frac{\partial^2 v}{\partial z^2} \quad [3]$$

Energy equation:

$$u \frac{\partial t}{\partial r} + w \frac{\partial t}{\partial z} = \alpha \frac{\partial^2 t}{\partial z^2} \quad [4]$$

The boundary conditions corresponding to both radial flow gas turbines and the present model are:

<u>At $r = r_0$:</u>	$u(r_0, z)$	$=$	$\frac{W}{2 \pi r_0 z_0 \rho}$
	$v(r_0, z)$	$=$	$r_0 \omega$
	$w(r_0, z)$	$=$	0
	$t(r_0, z)$	$=$	t_{in}
<u>At $z = 0$:</u>	$u(r, 0)$	$=$	0
	$v(r, 0)$	$=$	$r \omega$
	$w(r, 0)$	$=$	0
	$t(r, 0)$	$=$	t_w

The variables p , u , v , w , and t and the coordinates r and z are normalized as follows:

$$u^* = \frac{u}{u(r_0, z)} = \frac{u}{\left(\frac{W}{2 \pi r_0 z_0 \rho} \right)}$$

$$v^* = \frac{v}{v(r_0, z)} = \frac{v}{r_0 \omega}$$

$$\begin{aligned}
w^* &= \frac{w}{u(r_0, z)} = \frac{w}{\left(\frac{W}{2\pi r_0 z_0 \rho} \right)} \\
p^* &= \frac{g_c p}{\rho [u(r_0, z)]^2} = \frac{g_c p}{\left(\frac{W}{2\pi r_0 z_0 \rho} \right)^2 \rho} \\
t^* &= \frac{t - t_{in}}{t_w - t_{in}} \\
r^* &= \frac{r}{r_0} \\
z^* &= \frac{z}{z_0}
\end{aligned}$$

The normalized differential equations [1] through [4] become:

Continuity equation:

$$\frac{\partial u^*}{\partial r^*} + \frac{u^*}{r^*} + \left(\frac{r_0}{z_0} \right) \frac{\partial w^*}{\partial z^*} = 0 \quad [5]$$

Momentum equation in the radial direction:

$$\begin{aligned}
u^* \frac{\partial u^*}{\partial r^*} + \left(\frac{r_0}{z_0} \right) w^* \frac{\partial u^*}{\partial z^*} - \left[\frac{r_0 W}{\left(\frac{W}{2\pi r_0 z_0 \rho} \right)} \right]^2 \frac{v^{*2}}{r^*} = \\
\left(\frac{2\pi}{z_0 \mu} \right) \left(\frac{r_0}{z_0} \right)^2 \frac{\partial^2 u^*}{\partial z^{*2}} - \frac{dp^*}{dr^*} \quad [6]
\end{aligned}$$

Momentum equation in the tangential direction:

$$\begin{aligned}
u^* \frac{\partial v^*}{\partial r^*} + \left(\frac{r_0}{z_0} \right) w^* \frac{\partial v^*}{\partial z^*} + \frac{u^* v^*}{r^*} = \\
\left(\frac{2\pi}{z_0 \mu} \right) \left(\frac{r_0}{z_0} \right)^2 \frac{\partial^2 v^*}{\partial z^{*2}} \quad [7]
\end{aligned}$$

Energy equation:

$$u^* \frac{\partial t^*}{\partial r^*} + \left(\frac{r_o}{z_o} \right) w^* \frac{\partial t^*}{\partial z^*} = \frac{\left(\frac{k}{C_p \mu} \right) \left(\frac{2 \pi}{z_o \mu} \right) \left(\frac{r_o}{z_o} \right)^2}{\frac{\partial^2 t^*}{\partial z^{*2}}} \quad [8]$$

There are seen to be four groups that govern the fluid dynamics and heat transfer:

$$\frac{z_o}{r_o} \triangleq z_o^* \quad \text{nondimensional geometry for the rotating disk}$$

$$\frac{W}{z_o \mu} \triangleq N_{R,F} \quad \text{nondimensional flow rate; a flow Reynolds number}$$

$$\left[\frac{r_o \omega}{\left(\frac{W}{2 \pi r_o z_o \rho} \right)} \right] \triangleq \beta \quad \text{ratio of disk peripheral velocity to the entering fluid radial velocity}$$

By defining the conventional disk, or machine, Reynolds number as:

$$N_{R,M} = \frac{r_o^2 \omega \rho}{\mu}$$

the velocity ratio can be written as:

$$2 \pi \frac{N_{R,M}}{N_{R,F}} \triangleq \beta$$

and

$$\frac{C_p \mu}{k} = N_{Pr} \quad \text{the fluid Prandtl number}$$

The correspondence between the gas turbine and the rotating disk parameters can be established. Due to the nature of the model,

there are no disk parameters relating to power. This does not affect the modeling of the heat transfer behavior.

There is a gas turbine parameter relating the turbine tip speed to the speed of sound in the working fluids. This parameter does not appear in the model groups as the differential equations are written for essentially incompressible flow. The effect of high velocities is to produce variations in the fluid properties normal to the flow direction. For the model, the variations are small, and the fluid properties are essentially constant. For extension to high velocity flow, the results can be modified using the temperature dependent property correlations of (14). Therefore, the disk peripheral Mach number is not a significant parameter for the model tests.

A survey of the radial flow gas turbine field reveals the following nondimensional parameter ranges to be of interest:

$$\begin{array}{rcl} N_{R,F} & = & 10^5 \text{ to } 10^6 \\ N_{R,M} & = & 10^5 \text{ to } 5 \times 10^6 \\ \frac{N_{R,M}}{N_{R,F}} & = & 0.2 \text{ to } 1 \\ z_O^* & = & 0.1 \text{ to } 0.3 \\ N_{Pr} & = & 0.7 \end{array}$$

IV TEST FACILITY

A. Description of Test Facility

The present model is a rotating disk without vanes over which air flows radially inward. The disk is heated relative to the colder air flow. The fluid behavior and the heat transfer coefficients have been determined for this model. An overall description of the test facility follows, with the major components described in detail in the later sections.

A schematic of the test facility is shown in Fig. 3, and the actual test facility in Fig. 4. The disk is driven through a flat belt pulley drive by a variable speed d-c motor, and spins about a vertical axis. The disk is heated by the radiant energy emitted from the tubular quartz infrared heaters (Fig. 8). The distribution of the radiant energy is controlled by the vane reflectors to produce a uniform disk test surface temperature. The radiant energy is absorbed by the upper surface of the disk, conducted through the disk, and convected to the air flowing over the test surface. The heat flow through the laminated aluminum disk is measured by the heat meters bonded in the transite center disk (Fig. 5). The disk test surface temperature is measured by thermocouples embedded in the test surface (Fig. 6).

The air stream is induced over the test surface by a centrifugal blower. Provisions are made for a heated veil-flow over the test

surface. The screens affixed to the disk periphery (Fig. 6) accelerate the air flows to the disk peripheral velocity; the air leaves the screens in the radial direction with respect to the disk. The air mass flow rate is measured in the metering section upstream of the blower inlet.

The output leads of the heat meters and thermocouples mounted on the disk lead up through the hollow drive shaft to the rotating selector switch (Figs. 9, 10 and 11). The selector switch outputs go to the garter spring pickup.¹ The pickup transfers the output voltages from the rotating shaft to a stationary potentiometer for measurement of the heat meter and thermocouple voltages.

The air stream velocity and direction are measured in the flow passage between the rotating disk and the shroud. A three-hole total pressure and yaw probe is moved across the flow passage by a traversing mechanism (Fig. 13). The yaw probe angle is measured by a protractor attached to the traversing mechanism. The fluid static pressure is obtained from static pressure taps located in the plexiglass shroud (Fig. 12).

The heat transfer and fluid dynamics parameters are determined from these measured quantities. The disk speed is measured with a Strobotac. The air mass flow rate is measured at the metering section by the A.S.M.E. standard orifice installation. The fluid velocity

¹Developed on the suggestion of Mr. W. A. Casler of Aerojet General Corporation. Patents on the garter spring pickup are pending.

and flow direction are computed from the measured angles and dynamic pressures. The air properties are determined from temperature and pressure measurements and standard tabulated equation of state information (9). Heat transfer coefficients are evaluated from the heat flux measured by the heat meters and the temperature difference between the disk test surface and the incoming air.

In the following sections, the major components of the test facility are described in more detail.

B. Rotating Disk

The disk design was governed by model laws and heat transfer considerations. The design $N_{R,M}$ operating range is 10^5 to 2×10^6 , a range representative of gas turbine operations. A disk diameter of 16" and a maximum speed of 8000 RPM were chosen as having a low operating centrifugal stress and of convenient size for construction. Aluminum was chosen for the disk material as the stress level is the lowest and the factor of safety the highest relative to other conventional materials.

The disk thickness was dictated by the chosen method of determining the local heat transfer coefficients. The local heat flux at the disk test surface is determined from the heat meter surface heat flux and the test surface temperature distribution using the analytical solution to this heat conduction problem (Appendix D). A uniform test surface temperature relative to the temperature difference

between the disk and air was desired. The final disk thickness was 1.682 inches.

Preliminary calibration tests selected as the most satisfactory heat meters those manufactured by National Instrument Laboratories, Inc., Washington, D.C. The heat meter consists of a silver-tellurium wafer (0.4 inches in diameter and 0.06 inches thick) with a fine mesh copper screen bonded to each side. The temperature difference between the two copper and silver-tellurium junctions due to heat flow normal to the wafer produces a net EMF proportional to the heat flux. The calibration factors of these meters are in the range 600 - 800 (BTU/hr ft²)/mv. (A detailed description of the calibration is given in Appendix E.)

The upper surface of the thick aluminium disk was instrumented with five heat meters. (See Fig. 5 for a detail of the heat meter placement and disk construction.) The heat meters are placed at the area-average radius of each of five equal area annular sections. The heat meters are mounted on a transite disk, a material of about the same thermal conductivity as the heat meters. This insures that the thermal resistance normal to the disk will be uniform over the disk surface. To protect the heat meter section, a thin aluminum disk was bonded over the transite disk. Copper-constantan thermocouples were mounted in this disk to measure the heat meter temperatures. The disk assembly was bonded together with an epoxy resin

(Armstrong A-12). The heat meters were calibrated after bonding (Appendix E).

The disk test surface was instrumented with five copper-constantan thermocouples placed at the same radii as the heat meters. The test surface is shown in Fig. 6. The thermocouples are placed in grooves milled along isotherms (circumferential lines) to reduce heat conduction along the leads. The thermocouple end is peened into the groove to insure good thermal contact with the disk. The leads are electrically insulated from the disk by a coat of Glyptal cement.

The assembled disk specifications are:

Aluminum Alloy No. 2024 - T4

Yield Stress (0.2% offset)	47,000 psi
----------------------------	------------

Maximum Stress (computed at 8000 RPM)	9,000 psi
---------------------------------------	-----------

Disk Diameter	15.958 "
---------------	----------

Disk Thickness: Test disk	1.682 "
---------------------------	---------

Heat meter section	0.063
--------------------	-------

Epoxy resin	0.006
-------------	-------

Protective disk	<u>0.065</u>
-----------------	--------------

Total thickness	1.816 "
-----------------	---------

Thermal Conductivity:

Disk (6)	72 BTU/(hr ft ² F/ft)
----------	----------------------------------

Heat meter section	0.37 BTU/(hr ft ² F/ft)
--------------------	------------------------------------

C. Inlet Velocity Control

The design objective for the inlet velocity control was to produce a flow that was radial with respect to the disk at the disk periphery. This flow condition is representative of radial flow gas turbine operation. Preliminary tests showed that a simple variable pitch vane system installed in the inlet passage could not turn the flow sufficiently for large ratios of disk tangential velocity to through flow velocity (large $N_{R,M}/N_{R,F}$). It was decided that more elaborate methods using vanes would not have the flexibility desired for the test facility.

Preliminary tests also showed that screens wound around the disk periphery and extending over the air inlet passage would produce the desired flow condition. The air flow would be accelerated by the screens to the disk tangential velocity, and leave the screens in the radial direction relative to the disk. A design using 10 layers of 50 mesh aluminum screen 0.009 inches in diameter was chosen. Aluminum was used because of its low mass and consequent low centrifugal forces. A fine mesh minimized the heat transfer from the disk along the screen to the air stream.

A continuous 4.5" wide strip of screen was wound over the disk and inner lower hoop. The two outer hoops were then placed over the screen and bolted to the disk and inner hoop respectively. These hoops are made of 4130 aircraft steel (98,000 psi yield stress)

to withstand the centrifugal loading of both hoop and screen. The resulting air inlet passage height is 2.4 inches; the maximum z_o^* obtainable is 0.3. The screens installed are shown in Fig. 6. The inlet velocity passage is shown schematically in Fig. 7.

The disk screen assembly was balanced on a commercial balancing machine to 4000 RPM. The unbalance is within 8 gm-in, corresponding to an eccentricity of 0.0005 inches. The runout of the lower hoops is ± 0.050 inches. The natural frequency of the disk assembly mounted in the test facility is in the range 2800 - 3000 RPM.

D. Infrared Heating System

The design requirement for the disk heating system was that a heat flux varying with radius in a controlled manner could be applied to the disk. Preliminary tests showed that the infrared heating method would satisfy the design objective, with the advantage over more conventional heating methods that an airtight seal at the disk periphery would not be necessary. The installed heating system is shown in Fig. 8.

Heating is accomplished by four General Electric Tubular Quartz heaters producing a total of 6400 watts. The reflectors are gold-plated copper sheet; gold-plating is needed to obtain a high reflectivity in the infrared spectrum. A seal on the disk drive shaft minimizes the airflow through the reflector system.

The radiant energy absorbed at the upper surface of the disk can be controlled in three ways. The heater power intensity is controlled by varying the heater voltage. The radiant energy distribution impinging on the disk is controlled by varying the vane reflector angle. The energy absorbed by the disk can be controlled by selectively painting the disk with a high absorbtivity paint. For the present model, the upper surface was covered with a uniform coating of blackboard slating with an absorbtivity of approximately 0.9. The radiant energy distribution absorbed by the disk was thus controlled by voltage control and vane angle.

E. Selector Switch and Garter Spring Pickup

The use of thermoelectric elements mounted on the rotating disk necessitated the development of a select or switch and pickup assembly for transmitting the electrical outputs to stationary recording instruments. The unit developed for this purpose is depicted in Figs. 9 and 10. In Fig. 11, the unit is shown installed on the disk drive shaft. The 30 leads from the disk instruments (two each from the five heat meters and two each from ten thermocouples) are brought up through the hollow disk drive shaft to the copper pins of the connector (Fig. 11). The copper leads from the connector sockets are soldered to the copper selector contacts bonded in the selector switch housing (Fig. 9). Four circular segment contacts are located at each axial position to accommodate four leads from two thermoelectric elements. The selector rod

is moved axially to obtain outputs from any one of the eight sets of contacts. Copper leads (not shown in Fig. 9) from the copper foil contacts are brought through the hollow selector rod to the rotating vee-groove garter spring contacts.

The outputs are transferred from the rotating to the stationary garter spring contacts through the garter springs. These springs are made from beryllium copper wire wound to form a helical spring, with the ends of the spring soldered together to form a circle. The spring rolls between the rotating and stationary vee-groove contacts in the manner of a planetary gear train. Leads from the four stationary garter spring contacts are taken to a potentiometer for measurement of the element outputs.

The circuit for measurement of disk thermocouple outputs is modified to account for the constantan-copper junctions in the connector. A stationary copper-constantan compensation junction is introduced in the circuit to oppose the connector constantan-copper junctions. The compensation junction is maintained at the same temperature as the connector junctions by a small blower that continuously circulates air over the junctions. The ventilated connector, compensation junction, and blower are also seen in Fig. 11. An ice junction is used as the reference junction for the thermocouple output measurement.

The primary advantage of the garter spring pickup over

conventional slip ring or mercury pool units is the lack of significant extraneous EMF production at high rotative speeds. This is due to the absence of slipping, with consequent rubbing and heating, between the spring and the vee-grooves. Test showed that a maximum noise level of ± 5 microvolts (± 0.2 F) was produced at speeds up to 8000 RPM. Observations of the spring motion with a Strobotac verified the lack of slippage, and showed that the spring remains in contact with the vee-grooves at all speeds. The simplicity of construction and operation are also very desirable features.

F. Flow System

An airflow system was designed, constructed, and instrumented to provide metered main and veil-flows (Fig. 3). A suction system with a 13 stage centrifugal vacuum cleaner is used for the main flow system to eliminate the large plenum chamber that would be needed in a pressure system. A compressor is used to supply the veil-flow so that the flowrate may be varied independently of the main flow. Both flows are metered by calibrated A.S.M.E. standard orifice installations.

Preliminary testing revealed that the main airflow pressure drop through the test section became prohibitively high at high disk speeds (high $N_{R,M}/N_{R,F}$), with a resulting decrease in flow rate. This was attributed to the fluid kinetic energy dissipation in the

right angle turn from the passage between the disk and the shroud to the main flow ducting. At the higher disk speeds the tangential velocities were on the order of 400 ft/sec (Section V), and pressure measurements showed that all of the kinetic energy was dissipated.

To take the swirl out of the air and recover some kinetic energy before the turn into the ducting, a vaned diffuser was designed and installed. The diffuser mounted on the shroud is shown in Fig. 12. With the diffuser, the flow rate at the maximum test speed was doubled, and a nearly constant flow rate was obtainable over the test range. The change in flow pattern affected about 10 per cent of the disk heat transfer area. However, the effect on the mean heat transfer results is insignificant (Section VII).

G. Fluid Dynamics Instrumentation

The fluid dynamics was determined from measurements of the fluid velocity, flow angle, and wall static pressure. The wall static pressure was measured through wall taps located on the shroud (Fig. 12). As the pressure tap diameter was fairly large (0.128 inches), inserts were made to increase the length of the pressure tap hole to 2.5 diameters in accordance with the A.S.M.E. recommendations (1). The inserts were removed when the probe was entered through the tap for measurement of the fluid velocity.

The fluid velocity and flow angle were measured by a two-dimensional directional probe manufactured by the United Sensor

and Control Corporation, Glastonbury, Conn. (Fig. 13). The probe tip consists of three parallel open-ended tubes 0.030 inches in diameter. The two side tubes are chamfered 30° , and all tubes are bent 90° so as to measure pressures perpendicular to the probe axis, as shown in the following figure. The center tube is used to measure the fluid total pressure. The dynamic pressure is measured as the difference between the total pressure and the wall static pressure. The fluid resultant velocity was computed from this dynamic pressure.

The pressures in the two side tubes were balanced by probe rotation to determine the flow angle. A protractor affixed to the traversing mechanism allowed measurement of the amount of rotation. The fluid velocity components were computed from the resultant velocity and flow angle.

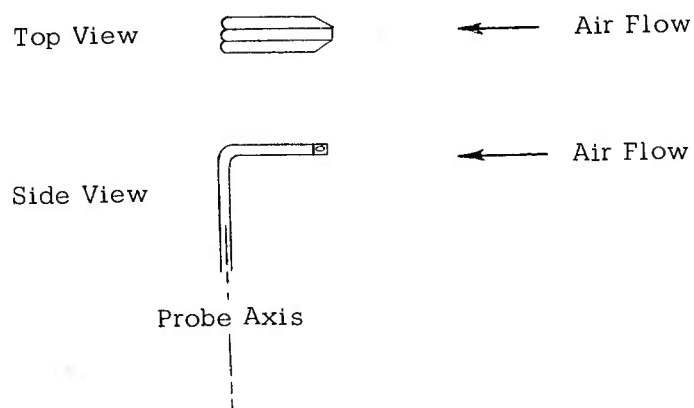


FIGURE 3

SCHEMATIC OF ROTATING DISK TEST FACILITY

FIGURE 4

ROTATING DISK TEST FACILITY

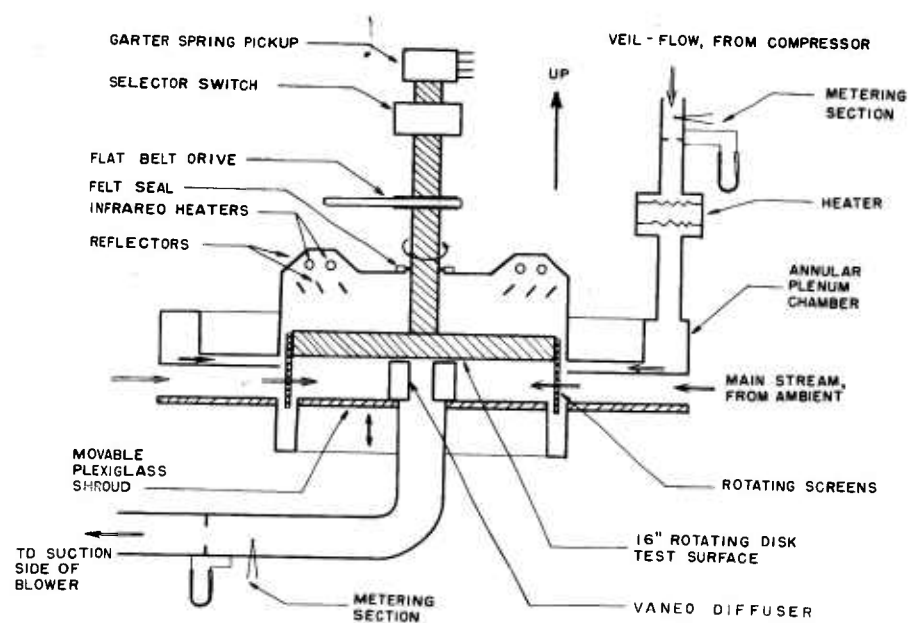


FIG. 3

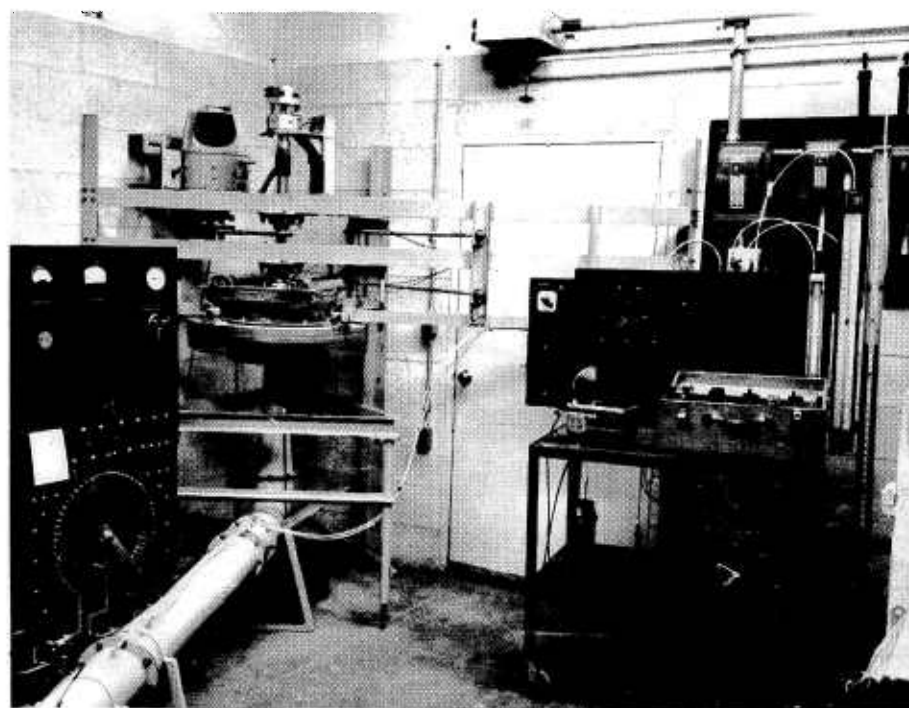


FIG. 4

FIGURE 5

SCHEMATIC OF DISK CROSS SECTION AND
INSTRUMENT LOCATIONS

FIGURE 6

DISK TEST SURFACE AND ROTATING SCREENS

FIGURE 7

SCHEMATIC OF TEST FACILITY INLET PASSAGE

FIGURE 8

INFRARED HEATING SYSTEM

FIGURE 9

SCHEMATIC OF THE SELECTOR SWITCH AND
GARTER SPRING PICKUP ASSEMBLY

1. Switch and Pickup Support
2. Selector Switch Housing
3. Selector Switch Contacts
4. Copper Foil Contacts
5. Selector Rod
6. Garter Spring Housing
7. Garter Spring
8. Garter Spring Contacts
9. Ball Bearing
10. Guide Rod for Sliding the Garter Spring Housing

FIGURE 10

CROSS SECTION THROUGH SELECTOR SWITCH
AND GARTER SPRING PICKUP

FIGURE 11

SELECTOR SWITCH AND GARTER SPRING PICKUP
MOUNTED ON DISK DRIVE SHAFT

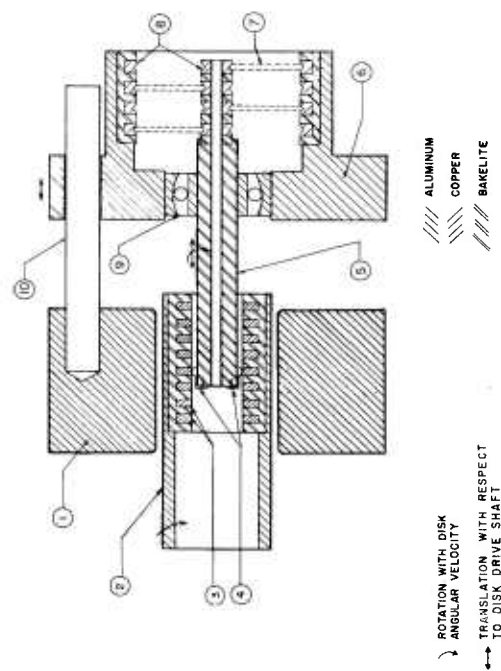


FIG. 9

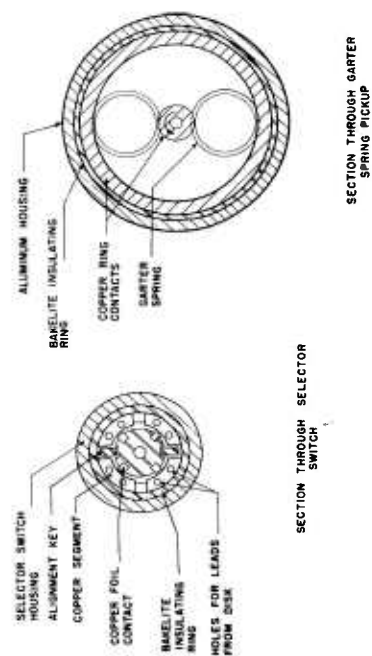


FIG. 10

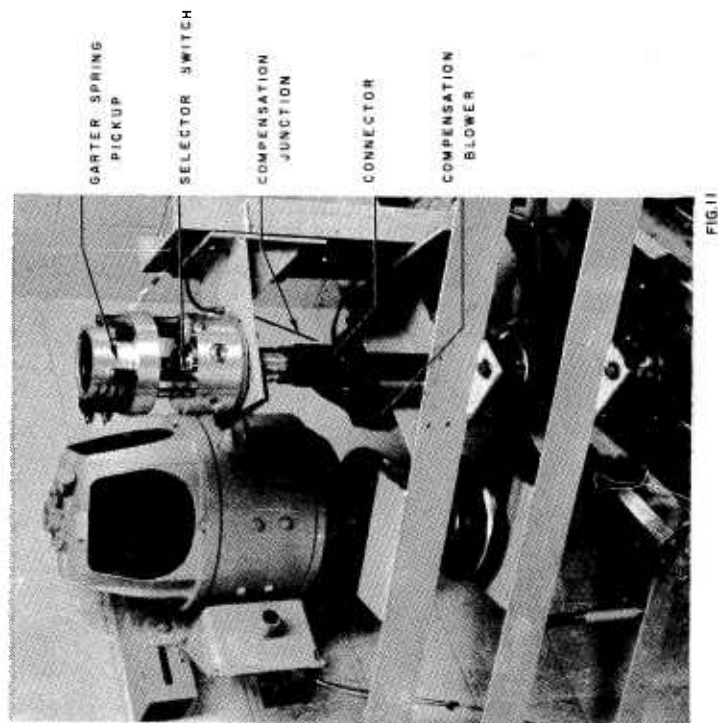


FIGURE 12

SHROUD AND VANED DIFFUSER

FIGURE 13

DIRECTIONAL PROBE AND TRAVERSING
MECHANISM

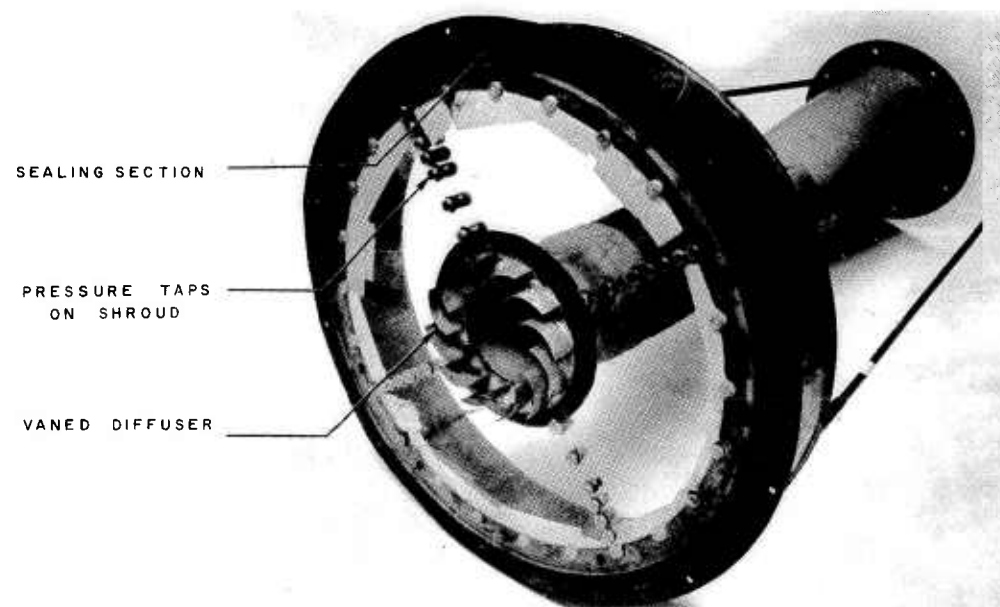


FIG.12

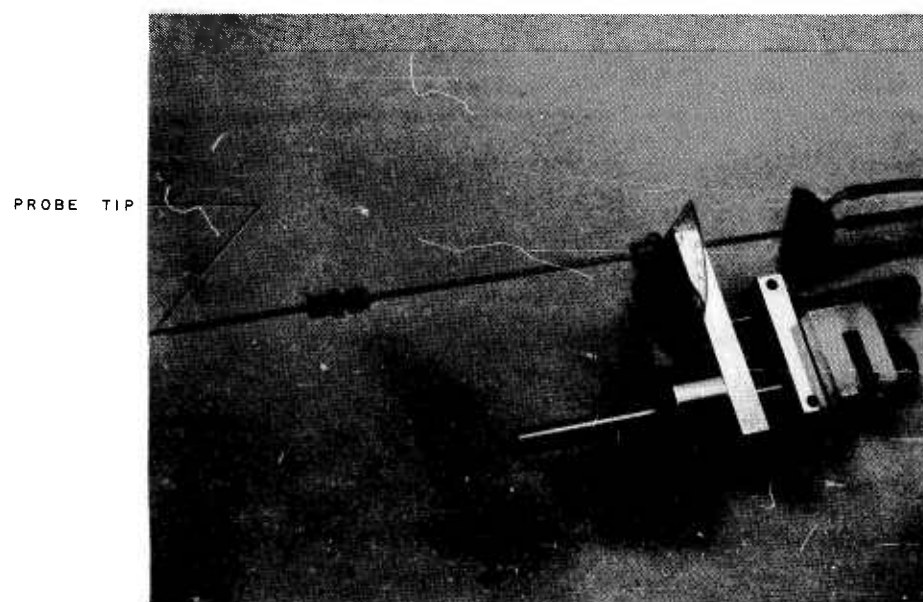


FIG.13

V EXPERIMENTAL RESULTS

A. Radial Inflow Flow Results

The objectives of the flow investigation are to:

1. Evaluate the performance of the rotating screens and sealing section.
2. Experimentally determine the fluid dynamics behavior.
3. Compare the experimentally determined fluid dynamics behavior with the behavior predicted by the analysis (Section VI).

The component performance was evaluated during the radial inflow tests. Therefore, the experimental flow results will be presented so as to answer the objectives concurrently.

The flow behavior was studied at a single disk-to-shroud clearance ratio of $z_0^* = 0.113$ over a machine Reynolds number range $N_{R,M} = 3.0 \times 10^4$ to 7.5×10^5 and a flow Reynolds number range $N_{R,F} = 3.4 \times 10^5$ to 5.8×10^5 . The test $N_{R,M}/N_{R,F}$ range was 0.05 to 1.6. Four types of flow results were obtained:

1. Tangential and radial component velocity profiles and flow angle profiles were determined at five radial positions for five $N_{R,M}/N_{R,F}$ ratios.
2. Total velocity and flow angle profiles were determined at four circumferential positions for two radial positions

and four $N_{R,M}/N_{R,F}$ ratios.

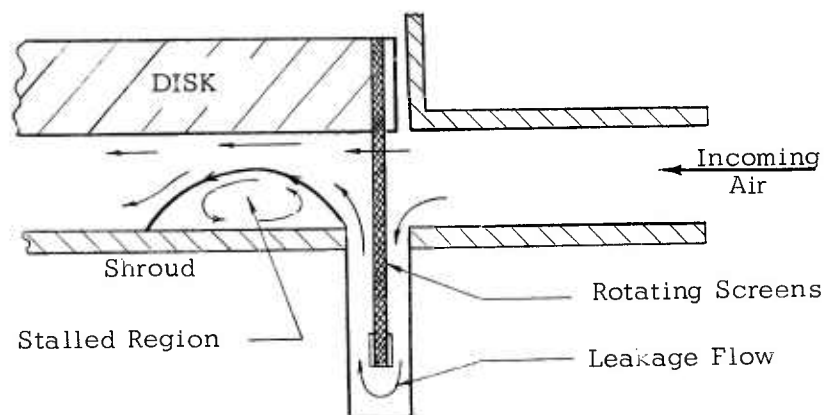
3. Total velocity and flow angle profiles were determined at two radial positions for four to six values of $N_{R,F}$ at two $N_{R,M}/N_{R,F}$ ratios. This was done to experimentally verify that the nondimensional parameters correlated the fluid dynamics behavior.
4. Wall static pressure variations with radial position were measured at four circumferential positions for five $N_{R,M}/N_{R,F}$ ratios.

The fluid velocity and flow angle was measured with the two-dimensional directional probe. The tangential and radial components were computed from the flow angle and the resultant velocity. The wall static pressure was measured with the static pressure taps located in the shroud.

The radial and tangential velocity profiles and the flow angle profiles for five radial positions are presented in Figs. 14 to 18 for five $N_{R,M}/N_{R,F}$ ratios. The corresponding profiles predicted from the one-dimensional flow analysis (Analytical Investigation, Section VI, Eq. [22], [23] and [24]) are also indicated on the figures. The profiles are predicted to be uniform across the flow passage.

The measured profiles at $r^* = 0.893$ show that the entering velocity profile is not uniform as desired. The shape of the profile

results from flow leakage around the edge of the rotating screen in the sealing section (Fig. 7). The leakage flow enters the main flow passage along the screens, creating a stalled region around the circumference of the plexiglass shroud. As the leakage flow has not been accelerated to the disk tangential velocity by the screens, a backflow in both the radial and tangential directions is created in the stalled region. Schematically, the flow picture near the test section inlet is:



The extent of the stalled region is greatest at low $N_{R,M}/N_{R,F}$ (0.056, 0.28). At high $N_{R,M}/N_{R,F}$ (1.20, 1.56), the effect of the leakage flow is considerably less; the stalled region does not extend as far radially inward and the entering profiles are more uniform.

The inlet profile appears to affect the flow pattern only near the outer edge of the disk. This is especially evident in Fig. 16,

where the $r^* = 0.893$ profile is completely unlike the shape of the other profiles, while the $r^* = 0.768$ profile is very similar to the remaining profiles. It appears that the effects of the disk, shroud, and flow area decrease outweigh the effect of the entering profile. The effect of the entering profile is further lessened at higher $N_{R,M}/N_{R,F}$.

A striking feature of the flow pattern is that at high $N_{R,M}/N_{R,F}$ the air is flowing radially inward near the disk and shroud, yet outward near the passage center. As seen in Figs. 17 and 18 for $N_{R,M}/N_{R,F}$ of 1.20 and 1.56 respectively, the radial outflow velocity is about equal to the radial inflow velocity near the disk, and one-fifth that near the shroud. This anomalous behavior was not predicted by the analysis. A three-dimensional representation of a profile illustrating this radial outflow is presented in Fig. 19.

The existence of backflow in the passage center can be rationalized. As the air flows radially inward, the angular momentum of the air is essentially conserved (as shown in Fig. 21 and discussed later). Consequently, the air tangential velocity increases in the radially inward direction. The disk tangential velocity decreases in the radially inward direction, and is less than the fluid tangential velocity. As a result, the wall shearing stresses on both the disk and the shroud act to decrease the air tangential velocity and create boundary layers of low tangential velocity fluid.

The centrifugal force field acting on the air, proportional to the square of the tangential velocity, is consequently greatest in the flow passage center. At high $N_{R,M}/N_{R,F}$, this force is evidently high enough to force the fluid itself to flow radially outward. The lower centrifugal force field in the regions near the disk and shroud allow the fluid to flow radially inward. As the disk is rotating, the centrifugal force is higher near the disk than the shroud. Consequently, the radial inflow in the region near the shroud is greater than that near the disk.

In Fig. 20, a cross section of the flow pattern is shown for $N_{R,M}/N_{R,F} = 1.20$. This flow pattern is somewhat similar to the flow pattern created by water draining from a tank. In this case, the angular momentum of the water is conserved as the water flows radially inward. At some radius, the resulting centrifugal force is high enough to prevent further radial inflow, resulting in a hollow vortex core.

The flow rates obtained from the integrated radial velocity profiles were compared to the flow rate measured at the flow metering section. The difference was within the accuracy of determining the radial velocity profiles. The uncertainty in the profiles is very high at large $N_{R,M}/N_{R,F}$ (the velocity uncertainty ranges are ± 0.5 per cent at $N_{R,M}/N_{R,F} = 0.056$, ± 6.5 per cent at 0.61, and ± 20 per cent at 1.57). The flow angle is near 90° , and the radial velocity

is computed as the cosine of the flow angle times the measured resultant velocity. Consequently, small errors in flow angle produce large errors in the radial velocity component. Nevertheless, the agreement between integrated and metered flows, and the self-consistency of the velocity profiles, strengthens the experimentally determined picture of the flow pattern.

The tangential velocity profiles are consistently lower than the profiles predicted by the analysis. This is a result of flow bypassing the rotating screens. As a measure of the performance of the screens, the angular momentum flux for the four highest $N_{R,M}/N_{R,F}$ ratios was evaluated. The angular momentum flux is related to the shearing stresses on the disk and shroud by the following equation (Analytical Investigation, Section VI):

$$(\tau_{\theta \text{ disk}} - \tau_{\theta \text{ shroud}}) r^2 = \frac{d}{dr^*} \left[\frac{\rho}{g_c} z_o r_o r^* \int_0^l u v dz^* \right] \quad [9]$$

where

$$\text{angular momentum flux} = \left[\frac{\rho}{g_c} z_o r_o r^* \int_0^l u v dz^* \right] \quad [10]$$

The angular momentum flux is presented as a function of radius for the four $N_{R,M}/N_{R,F}$ ratios in Fig. 21a. The flux is constant within the experimental uncertainty, showing that the disk and

shroud shear stresses are small relative to the momentum fluxes. The constant value of momentum flux provides a check on the instrumentation. Any significant increase in momentum flux in the radially inward direction would violate the laws of motion, and therefore be a result of inaccuracies in measuring velocity.

The ratio of the actual angular momentum flux to that predicted is plotted as a function of $N_{R,M}/N_{R,F}$ in Fig. 21b. The values of 0.70 - 0.75 indicate that 25 - 30% of the main flow bypasses the rotating screens, and is not accelerated to the disk tangential velocity. The apparent increase in the ratio could be due to the experimental inaccuracy of determining the radial velocity component. The uncertainty is highest at high $N_{R,M}/N_{R,F}$, and the integrated profiles tended to yield higher flow rates than those measured at the orifice metering section. However, an increase in the momentum flux ratio with increased $N_{R,M}/N_{R,F}$ is supported by comparing the measured pressure drop across the screens to the pressure drop computed for no bypass flow; these results indicate that less bypass flow occurs at higher disk speeds (higher $N_{R,M}/N_{R,F}$).

The variation of velocity and flow angle profile with circumferential position for four $N_{R,M}/N_{R,F}$ ratios is shown in Figs. 22 to 25. In Fig. 26, the tangential velocity variation with circumferential position is shown for two $N_{R,M}/N_{R,F}$. Axial symmetry is seen to be best at the higher $N_{R,M}/N_{R,F}$. The lack of axial symmetry probably

results from the eccentricity of the sealing section with respect to the disk axis. The bypass flow area, and therefore the bypass flow, would then vary around the shroud periphery. This would result in an asymmetric main flow. It is doubtful that the asymmetry was caused by variations in the shroud-to-disk clearance, as the variation in clearance around the periphery was less than ± 0.7 percent.

In conclusion, at $N_{R,M}/N_{R,F}$ of 0.61 and greater, the flow is essentially axisymmetric. This is consistent with the previous velocity profile results, where the effect of the inlet is less at higher $N_{R,M}/N_{R,F}$.

Nondimensional velocity and flow angle profiles were compared to help verify that the nondimensional parameters chosen govern the fluid dynamics. In Figs. 27 and 28, comparisons are made with $N_{R,F}$ as a parameter for various $N_{R,M}/N_{R,F}$ ratios. The nondimensional profiles are all similar in shape. The discrepancy between the profiles exceeds the estimated uncertainty, and does not vary systematically with $N_{R,F}$. It is possible that additional errors in velocity measurement are introduced when $N_{R,F}$ is a variable. (See Appendix B for a discussion of velocity measuring errors.) The similarity in profile shape supports the choice of nondimensional parameters, but a definite verification awaits further tests.

The flow angle profiles of Figs. 27 and 28 are in good agreement with the exception of the results for $r^* = 0.768$ and $N_{R,M}/N_{R,F} = 0.30$. The discrepancies exist, and are probably caused by increased

flow leakage past the rotating screens at low flows ($N_{R,F}$). Again, the inlet effect is mitigated at the inner radii by the flow area decrease. At the higher $N_{R,M}/N_{R,F}$, the effects of the disk, shroud, and area change predominate. This agreement between the flow angle profiles supports the choice of nondimensional parameters.

The variation of the wall static pressure with radius is presented in Fig. 29. Data was obtained at all r^* for only one circumferential position, and supplemented by some data at other circumferential positions. The axial symmetry as indicated by the static pressures is not as good as that indicated by the velocity profile results. This is partially a result of small uncertainties in the pressure tap location. The tap location uncertainty due to shroud eccentricity with the disk axis is about ± 0.080 inches, or $\pm 0.01 r_0$.

At small radii, the pressure variation with radius follows the trend of the predicted variation (Analytical Investigation, Section VI, Eq. [25]). The discrepancies at the disk inlet are due to the stall created by the leakage flow. The inlet effect is again felt only at the outer radii, and is less at higher $N_{R,M}/N_{R,F}$.

Some limited nondimensional static pressure variations for two $N_{R,M}/N_{R,F}$ are presented in Figs. 29c and 29d. The correlation is quite good. This helps support the choice of $N_{R,F}$ and $N_{R,M}/N_{R,F}$ as the nondimensional parameters governing the fluid dynamics.

The following conclusions can be drawn from the radial inflow fluid dynamics investigation:

1. The performance of the rotating screen and seal is less than desired. The rotating screens accelerate only 70 - 75 per cent of the main flow to the disk tangential velocity. The remaining 25 - 30 per cent of the flow bypasses the rotating screens. To accurately establish the flow picture, this defect must be remedied.
2. The flow that bypasses the rotating screens affects the flow behavior only near the edge of the disk. The inlet effect diminishes as $N_{R,M}/N_{R,F}$ increases.
3. The fluid dynamics behavior is described in Figs. 14 - 18, and differs considerably from that predicted by the analysis (Section VI). The reasons for the discrepancies between experiment and analysis are discussed in Section VII.
4. The radial inflow velocities are greatest in the regions nearest the disk and the shroud. At $N_{R,M}/N_{R,F}$ of 0.61 and higher, the flow is radially outward in the passage center.
5. Within the experimental uncertainties, the fluid angular momentum is conserved as the fluid flows radially inward.
6. The predicted nondimensional parameters, $N_{R,F}$ and $N_{R,M}/N_{R,F}$, appear to govern the fluid dynamics. A definite verification awaits additional tests.

FIGURE 14

FLUID VELOCITY COMPONENT AND FLOW
ANGLE PROFILES

$$N_{R,F} = 5.6 \times 10^5$$

$$N_{R,M} = 3.2 \times 10^4$$

$$N_{R,M}/N_{R,F} = 0.056$$

- (a) Tangential Velocity Profiles
- (b) Radial Velocity Profiles
- (c) Flow Angle Profiles

DATA

- $r^* = 0.893$
- $r^* = 0.768$
- △ $r^* = 0.642$
- ◇ $r^* = 0.517$
- ▽ $r^* = 0.391$

- Disk tangential velocity at $r^* = 0.893$
- ▼ Disk tangential velocity at $r^* = 0.391$

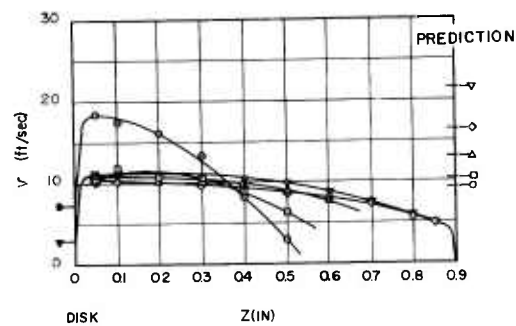
ANALYSIS (SECTION VI)

Tangential velocity, v , predicted by Eq. [23]

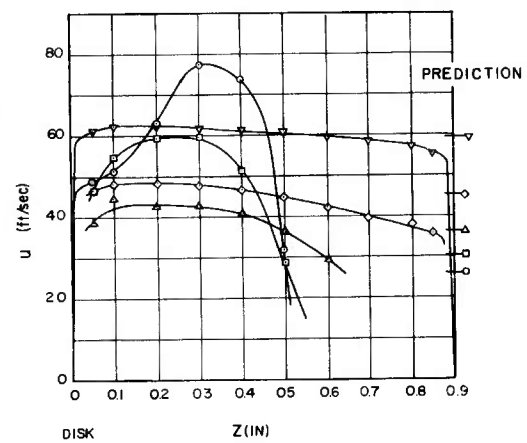
Radial velocity, u , predicted by Eq. [22]

Flow angle predicted by Eq. [24]

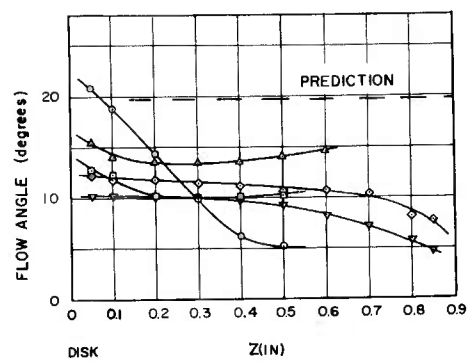
—○, □, △, ◇, ▽



(a)



(b)



(c)

FIGURE 15

FLUID VELOCITY COMPONENT AND FLOW
ANGLE PROFILES

$$\begin{aligned} N_{R,F} &= 5.6 \times 10^5 \\ N_{R,M} &= 1.59 \times 10^4 \\ N_{R,M}/N_{R,F} &= 0.28 \end{aligned}$$

- (a) Tangential Velocity Profiles
- (b) Radial Velocity Profiles
- (c) Flow Angle Profiles

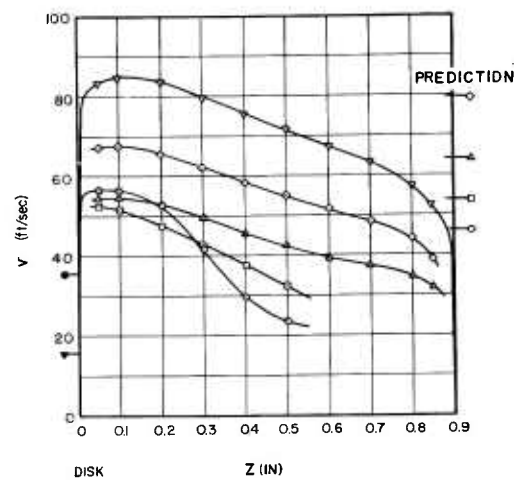
DATA

$$\begin{aligned} \odot \ r^* &= 0.893 \\ \square \ r^* &= 0.768 \\ \triangle \ r^* &= 0.642 \\ \diamond \ r^* &= 0.517 \\ \nabla \ r^* &= 0.391 \end{aligned}$$

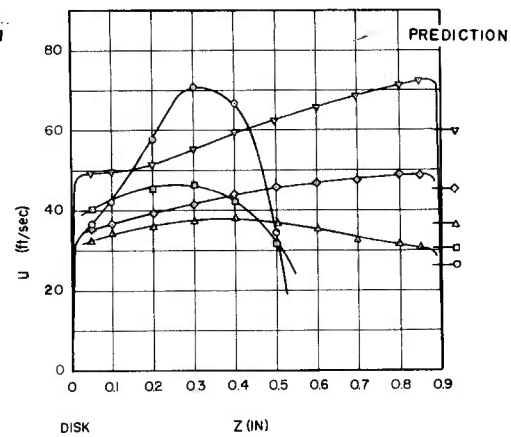
- Disk tangential velocity at $r^* = 0.893$
- ▼ Disk tangential velocity at $r^* = 0.391$

ANALYSIS (SECTION VI)

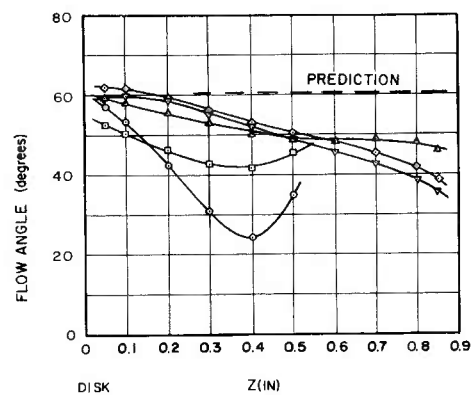
Tangential velocity, v , predicted by Eq. [23]
 Radial velocity, u , predicted by Eq. [22]
 Flow angle predicted by Eq. [24]
 —○, □, △, ◇, ▽



(a)



(b)



(c)

FIGURE 16

FLUID VELOCITY COMPONENT AND FLOW
ANGLE PROFILES

$$N_{R,F} = 5.6 \times 10^5$$

$$N_{R,M} = 3.4 \times 10^4$$

$$N_{R,M}/N_{R,F} = 0.61$$

(a) Tangential Velocity Profiles

(b) Radial Velocity Profiles

(c) Flow Angle Profiles

DATA

$$\odot r^* = 0.893$$

$$\square r^* = 0.768$$

$$\triangle r^* = 0.642$$

$$\diamond r^* = 0.517$$

$$\nabla r^* = 0.391$$

● Disk tangential velocity at $r^* = 0.893$

▼ Disk tangential velocity at $r^* = 0.391$

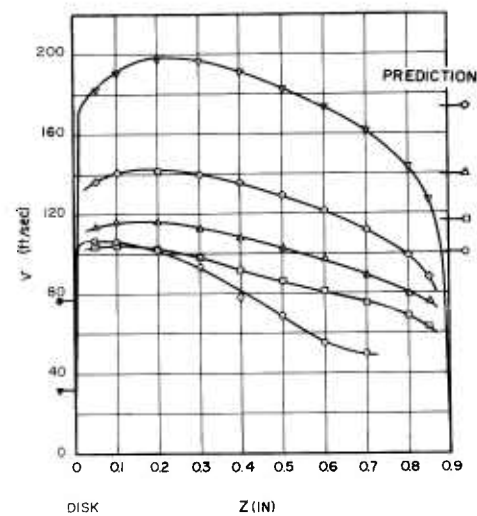
ANALYSIS (SECTION VI)

Tangential velocity, v , predicted by Eq. [23]

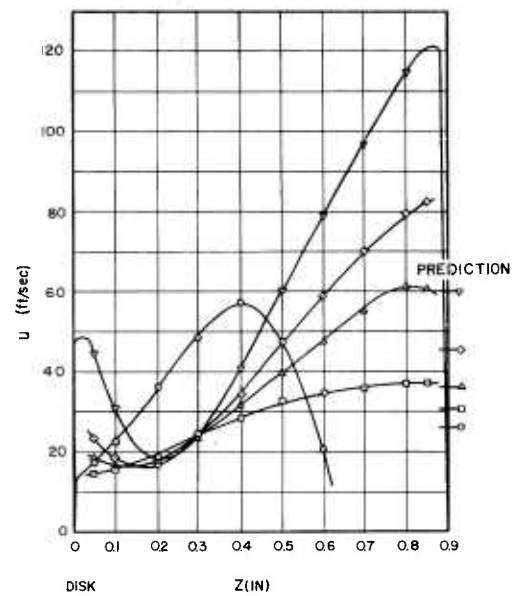
Radial velocity, u , predicted by Eq. [22]

Flow angle predicted by Eq. [24]

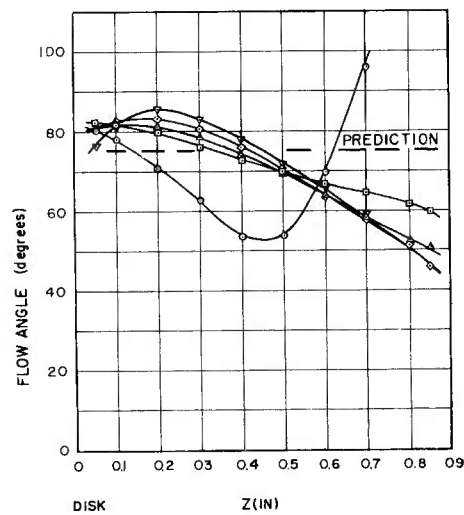
—○, □, △, ◇, ▽



(a)



(b)



(c)

FIGURE 17

FLUID VELOCITY COMPONENT AND FLOW
ANGLE PROFILES

$$\begin{aligned} N_{R,F} &= 5.2 \times 10^5 \\ N_{R,M} &= 6.2 \times 10^5 \\ N_{R,M}/N_{R,F} &= 1.20 \end{aligned}$$

- (a) Tangential Velocity Profile
- (b) Radial Velocity Profile
- (c) Flow Angle Profile

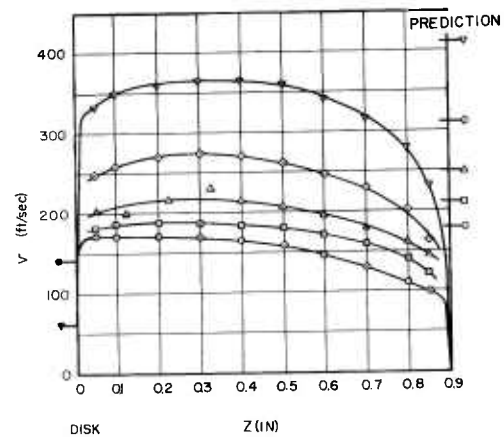
DATA

$$\begin{aligned} \odot r^* &= 0.893 \\ \square r^* &= 0.768 \\ \triangle r^* &= 0.642 \\ \diamond r^* &= 0.517 \\ \nabla r^* &= 0.391 \end{aligned}$$

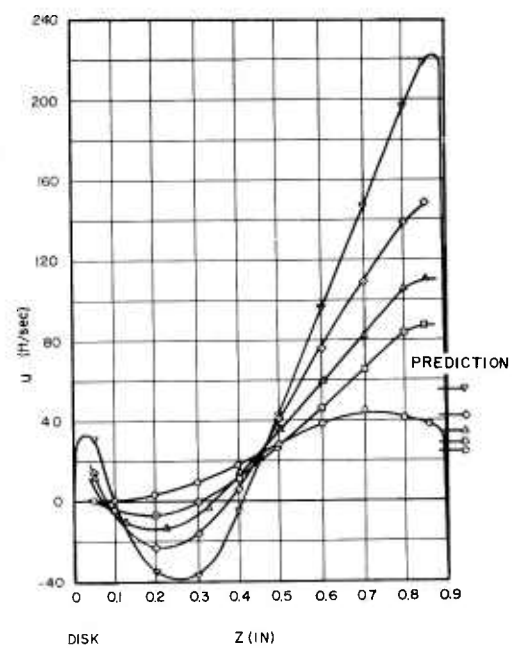
- Disk tangential velocity at $r^* = 0.893$
- ▼ Disk tangential velocity at $r^* = 0.391$

ANALYSIS (SECTION VI)

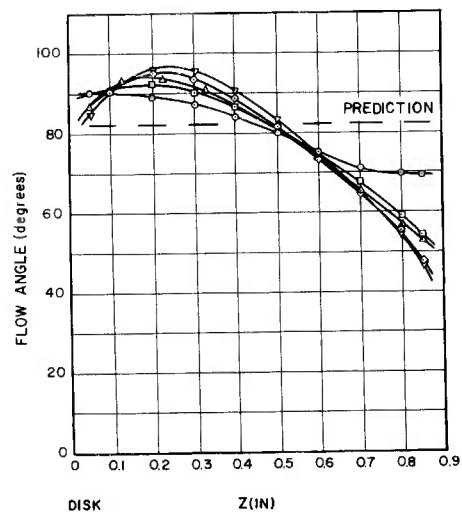
Tangential velocity, v , predicted by Eq. [23]
 Radial velocity, u , predicted by Eq. [22]
 Flow angle predicted by Eq. [24]
 —○, □, △, ◇, ▽



(a)



(b)



(c)

FIGURE 18

FLUID VELOCITY COMPONENT AND FLOW ANGLE
PROFILES

$$\begin{aligned} N_{R,F} &= 4.8 \times 10^5 \\ N_{R,M} &= 7.5 \times 10^5 \\ N_{R,M}/N_{R,F} &= 1.56 \end{aligned}$$

(a) Tangential Velocity Profiles

(b) Radial Velocity Profiles

(c) Flow Angle Profiles

DATA

$$\begin{aligned} \odot \ r^* &= 0.893 \\ \square \ r^* &= 0.768 \\ \triangle \ r^* &= 0.642 \\ \diamond \ r^* &= 0.517 \\ \nabla \ r^* &= 0.391 \end{aligned}$$

- Disk tangential velocity at $r^* = 0.893$
- ▼ Disk tangential velocity at $r^* = 0.391$

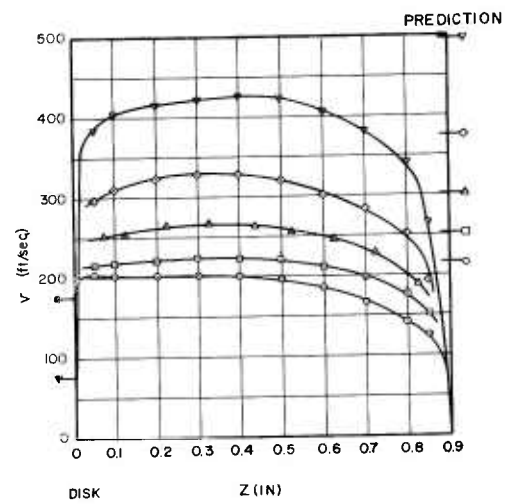
ANALYSIS (SECTION VI)

Tangential velocity, v , predicted by Eq. [23]

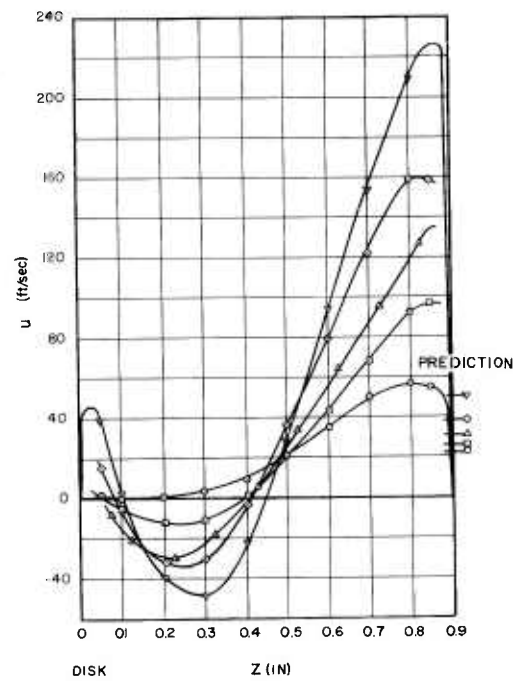
Radial velocity, u , predicted by Eq. [22]

Flow angle predicted by Eq. [24]

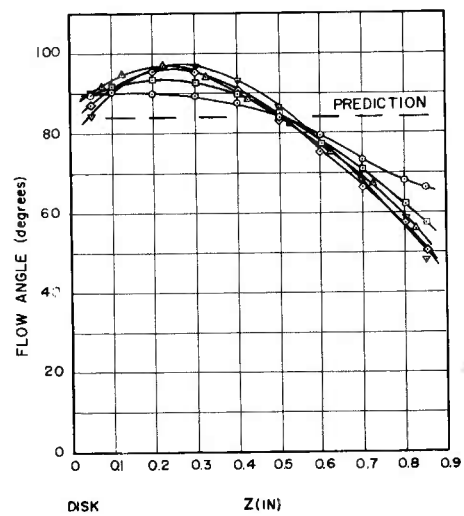
—○, □, △, ◇, ▽



(a)



(b)



(c)

FIGURE 19

THREE-DIMENSIONAL VELOCITY PROFILE
REPRESENTATION

FIGURE 20

FLOW PATTERN ILLUSTRATING BACKFLOW
IN THE CENTER OF THE FLOW PASSAGE

$$\frac{N_{R,M}}{N_{R,F}} = 1.20, \quad r^* = 0.517$$

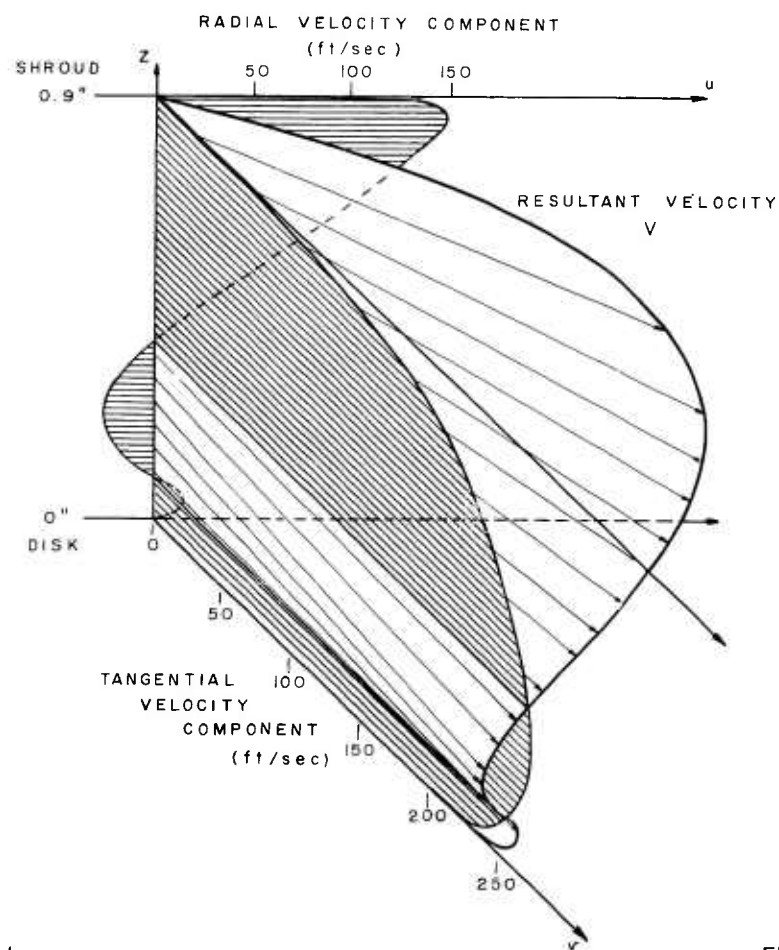


FIG. 19

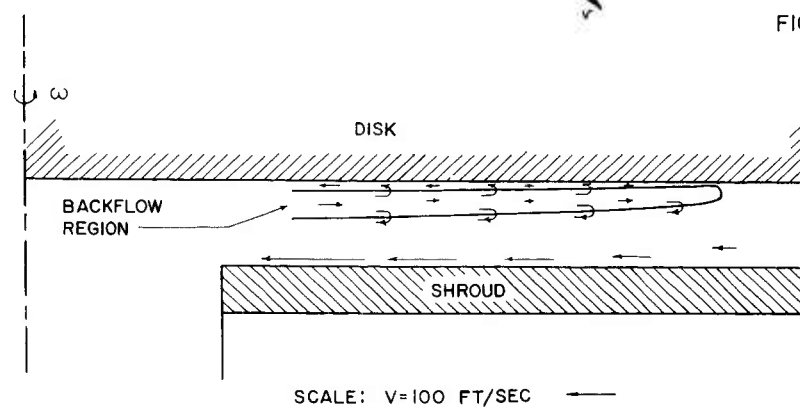
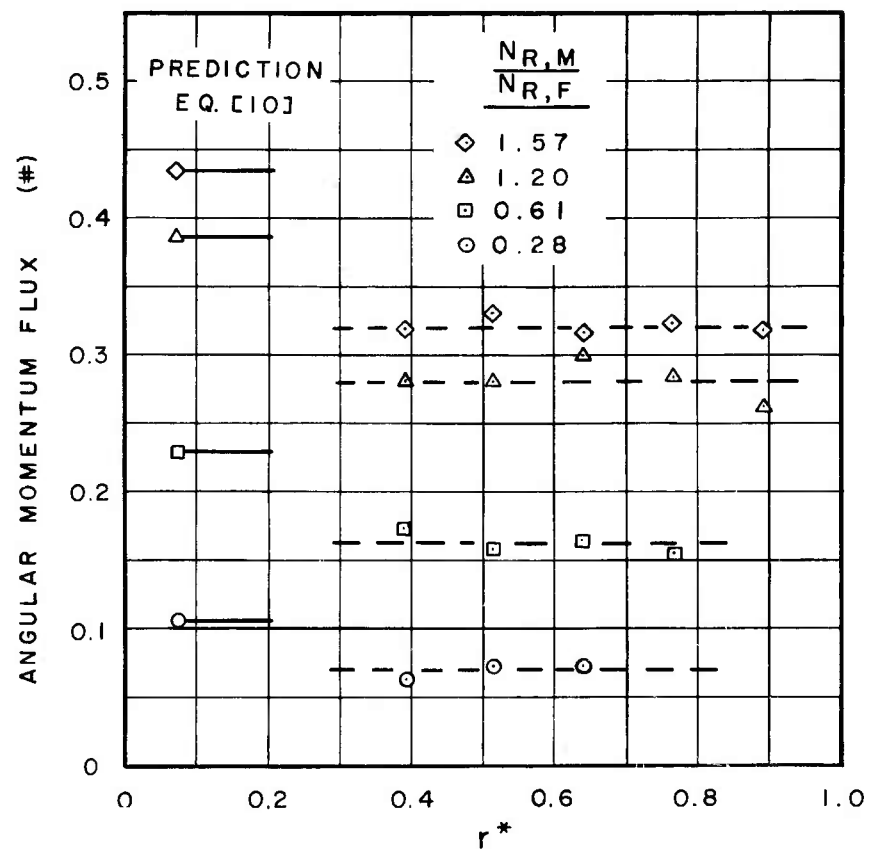


FIG. 20

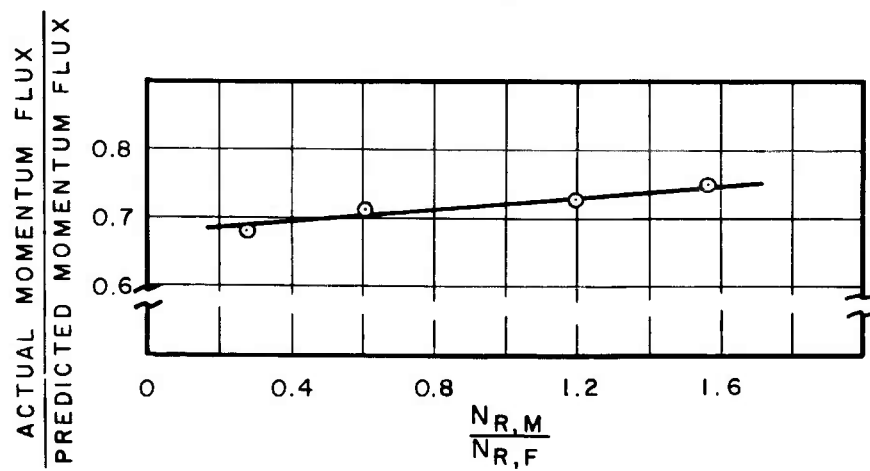
FIGURE 21

FLUID ANGULAR MOMENTUM FLUX

- (a) Angular Momentum Flux as a Function
of Radius
- (b) Ratio of Actual Momentum Flux to that
Predicted as a Function of $N_{R,M}/N_{R,F}$



(a)



(b)

FIGURE 22

RESULTANT VELOCITY AND FLOW ANGLE PROFILE
VARIATION WITH CIRCUMFERENTIAL POSITION

$$N_{R,F} = 5.6 \times 10^5$$

$$N_{R,M} = 3.2 \times 10^4$$

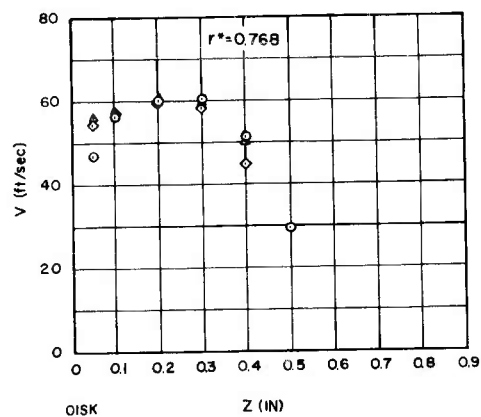
$$N_{R,M}/N_{R,F} = 0.056$$

(a) Resultant Velocity, $r^* = 0.768$

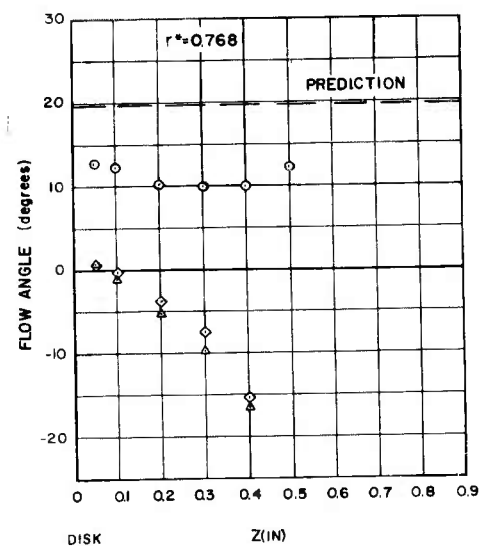
(b) Flow Angle, $r^* = 0.768$

(c) Resultant Velocity, $r^* = 0.517$

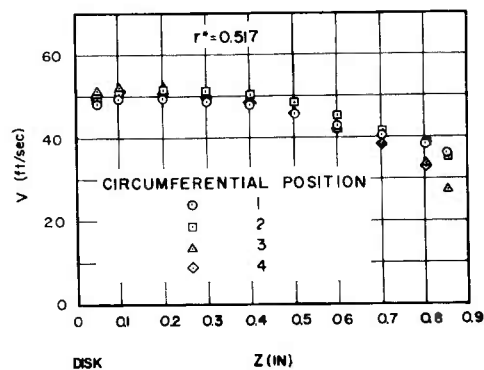
(d) Flow Angle, $r^* = 0.517$



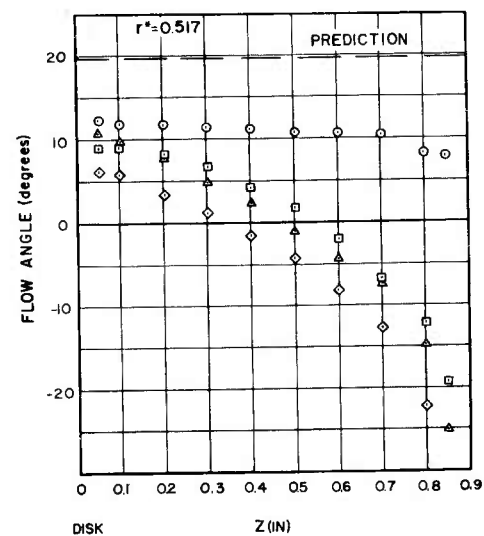
(a)



(b)



(c)



(d)

FIGURE 23

RESULTANT VELOCITY AND FLOW ANGLE PROFILE
VARIATION WITH CIRCUMFERENTIAL POSITION

$$N_{R,F} = 5.6 \times 10^5$$

$$N_{R,M} = 1.59 \times 10^5$$

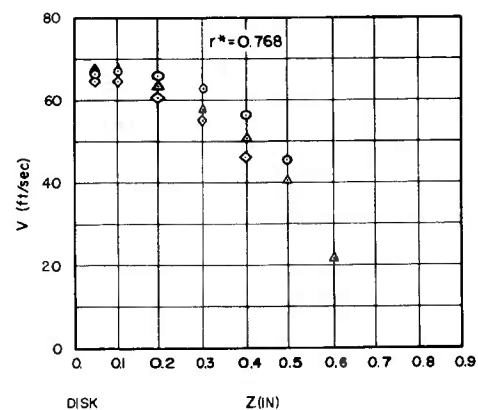
$$N_{R,M}/N_{R,F} = 0.28$$

(a) Resultant Velocity, $r^* = 0.768$

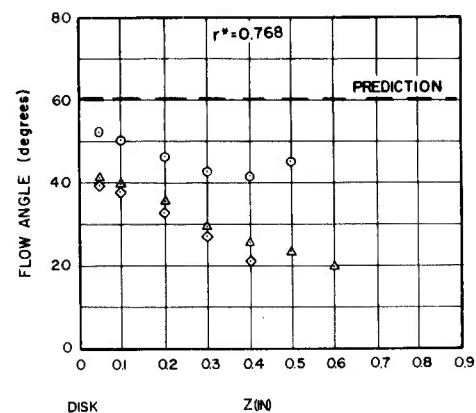
(b) Flow Angle, $r^* = 0.768$

(c) Resultant Velocity, $r^* = 0.517$

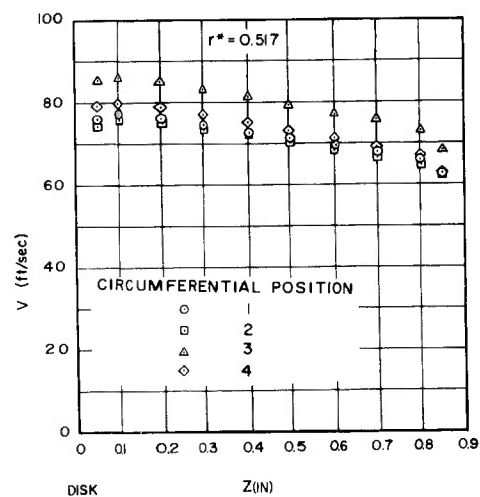
(d) Flow Angle, $r^* = 0.517$



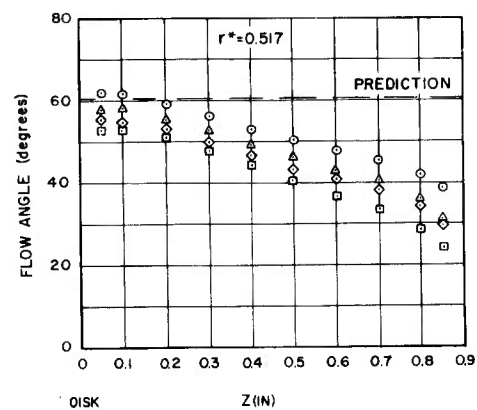
(a)



(b)



(c)



(d)

FIGURE 24

RESULTANT VELOCITY AND FLOW ANGLE PROFILE
VARIATION WITH CIRCUMFERENTIAL POSITION

$$N_{R,F} = 5.6 \times 10^5$$

$$N_{R,M} = 3.4 \times 10^5$$

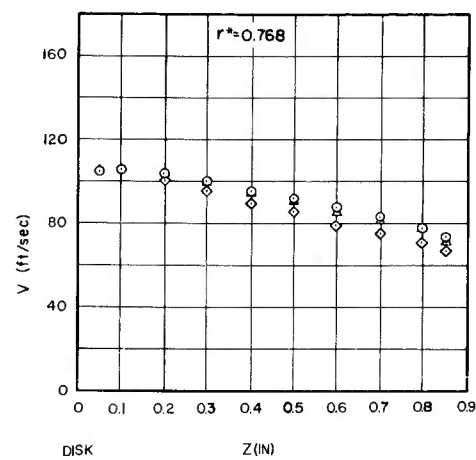
$$N_{R,M}/N_{R,F} = 0.61$$

(a) Resultant Velocity, $r^* = 0.768$

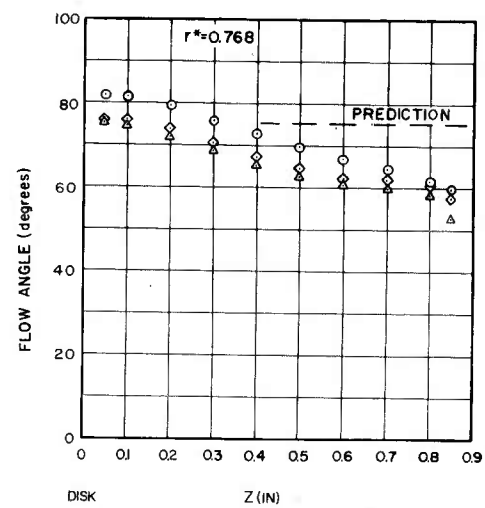
(b) Flow Angle, $r^* = 0.768$

(c) Resultant Velocity, $r^* = 0.517$

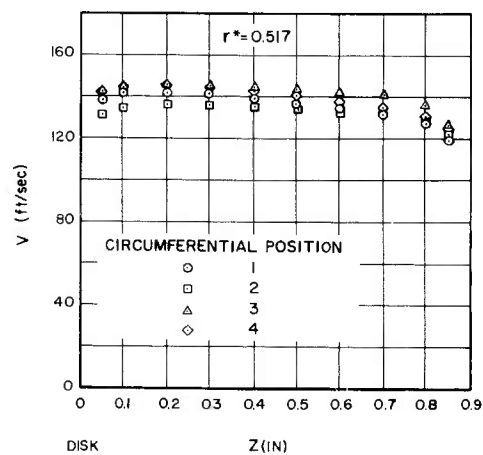
(d) Flow Angle, $r^* = 0.517$



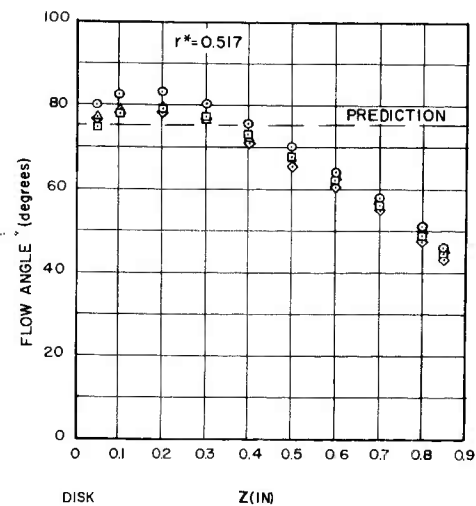
(a)



(b)



(c)



(d)

FIGURE 25

RESULTANT VELOCITY AND FLOW ANGLE PROFILE
VARIATION WITH CIRCUMFERENTIAL POSITION

$$N_{R,F} = 5.2 \times 10^5$$

$$N_{R,M} = 6.2 \times 10^5$$

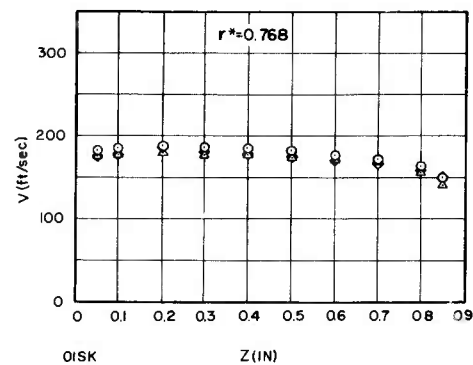
$$N_{R,M}/N_{R,F} = 1.20$$

(a) Resultant Velocity, $r^* = 0.768$

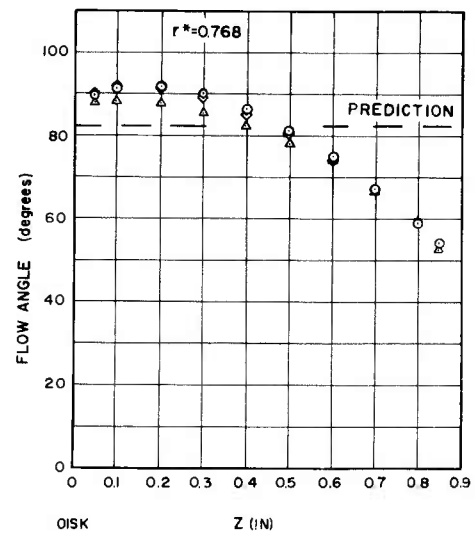
(b) Flow Angle, $r^* = 0.768$

(c) Resultant Velocity, $r^* = 0.517$

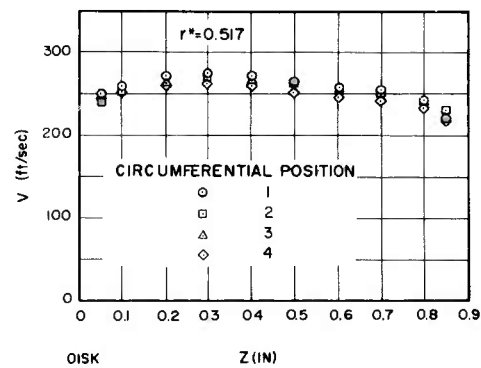
(d) Flow Angle, $r^* = 0.517$



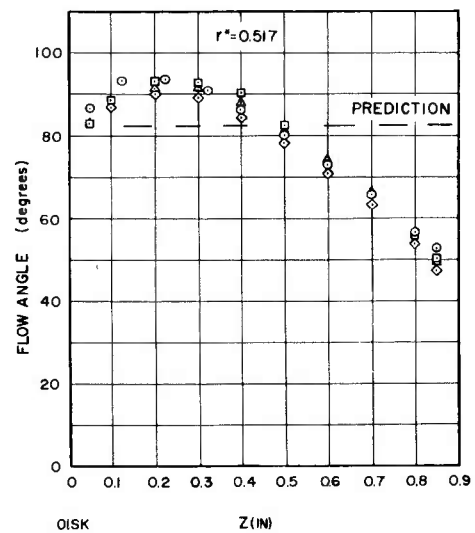
(a)



(b)



(c)



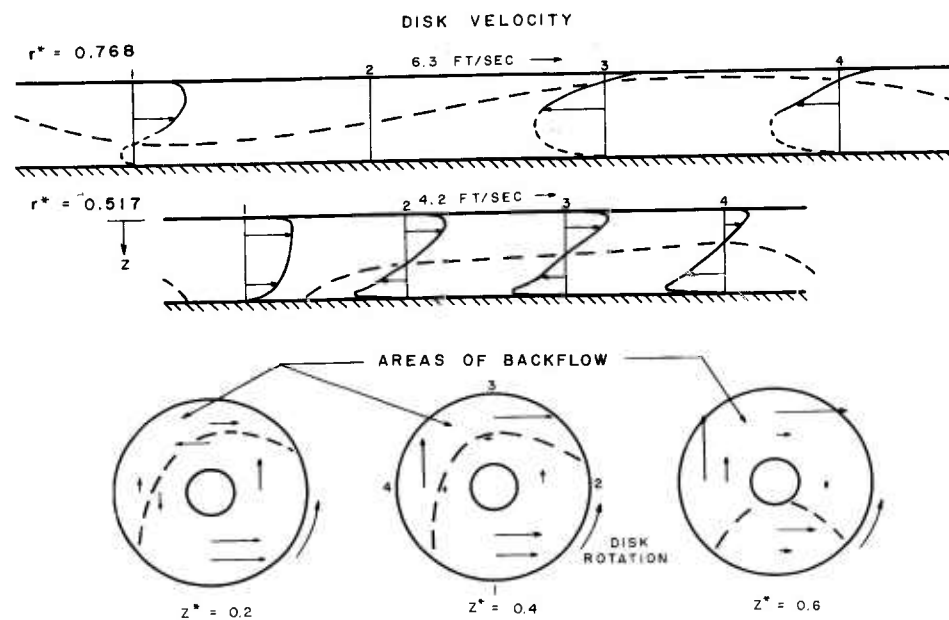
(d)

FIGURE 26

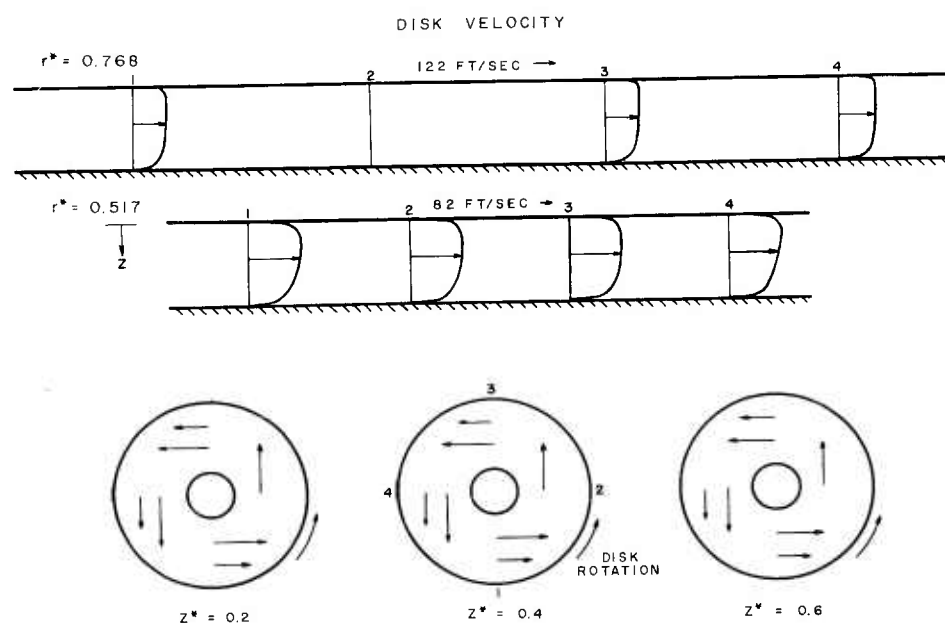
TANGENTIAL VELOCITY VARIATION WITH
CIRCUMFERENTIAL POSITION

$$(a) \ N_{R,M}/N_{R,F} = 0.056$$

$$(b) \ N_{R,M}/N_{R,F} = 1.20$$



(a)



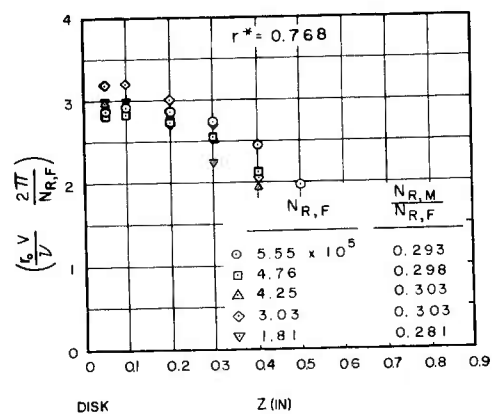
(b)

FIGURE 27

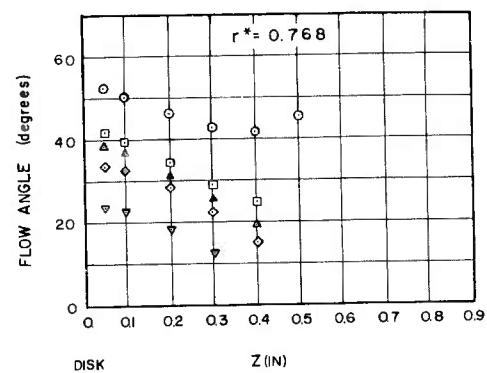
NONDIMENSIONAL VELOCITY AND FLOW ANGLE
PROFILE VARIATION WITH $N_{R,F}$

$$N_{R,M}/N_{R,F} = 0.30$$

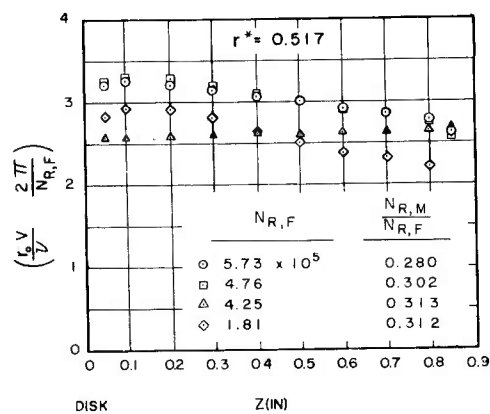
- (a) Nondimensional Velocity, $r^* = 0.768$
- (b) Flow Angle, $r^* = 0.768$
- (c) Nondimensional Velocity, $r^* = 0.517$
- (d) Flow Angle, $r^* = 0.517$



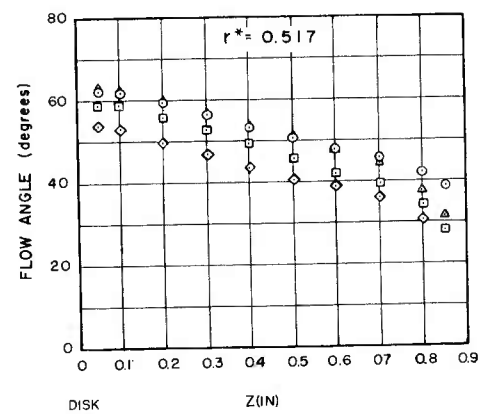
(a)



(b)



(c)



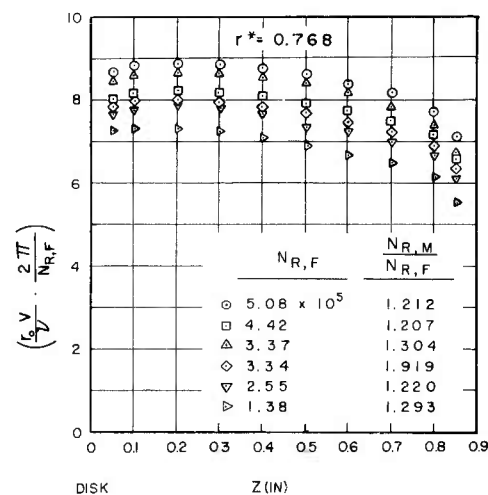
(d)

FIGURE 28

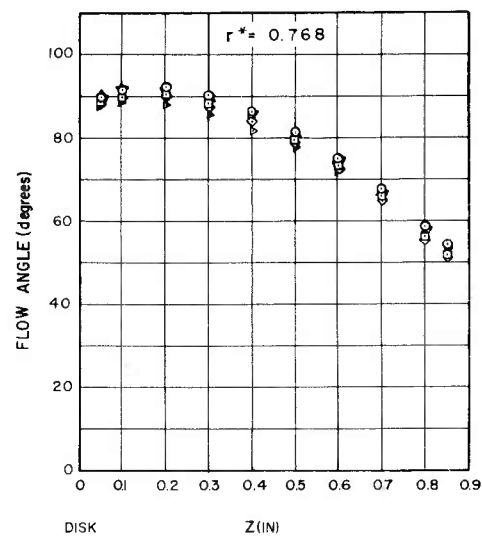
NONDIMENSIONAL VELOCITY AND FLOW
ANGLE PROFILE VARIATION WITH $N_{R,F}$

$$N_{R,M}/N_{R,F} = 1.22$$

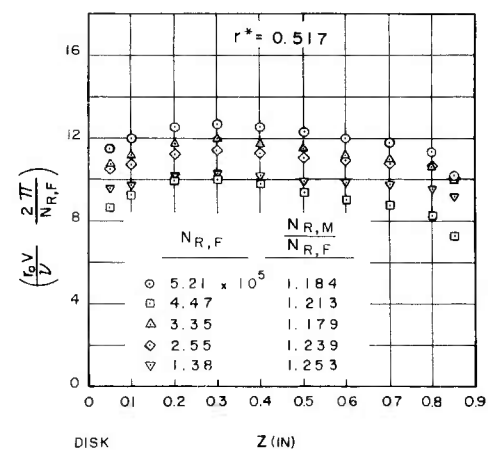
- (a) Nondimensional Velocity, $r^* = 0.768$
- (b) Flow Angle, $r^* = 0.768$
- (c) Nondimensional Velocity, $r^* = 0.517$
- (d) Flow Angle, $r^* = 0.517$



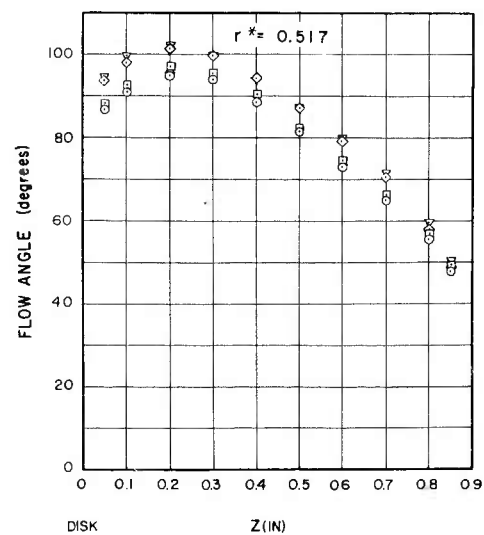
(a)



(b)



(c)



(d)

FIGURE 29

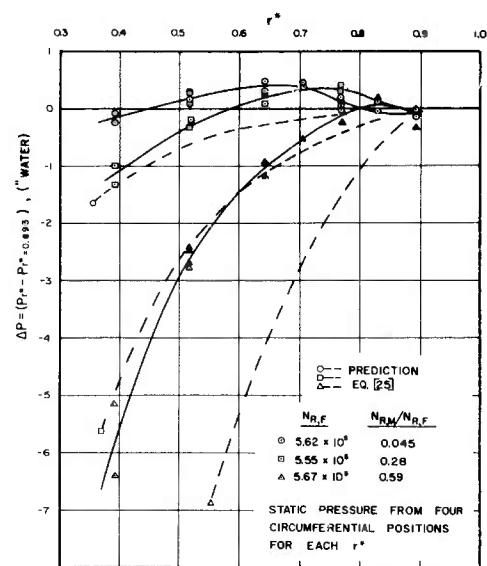
WALL STATIC PRESSURE VARIATION WITH
RADIAL POSITION

(a) Static Pressure, $N_{R,M}/N_{R,F} = 0.045,$
0.28, and 0.59

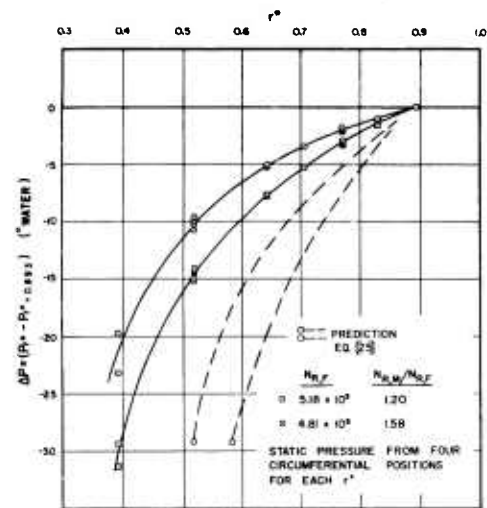
(b) Static Pressure, $N_{R,M}/N_{R,F} = 1.20$
and 1.58

(c) Nondimensional Static Pressure,
 $N_{R,M}/N_{R,F} = 0.29$

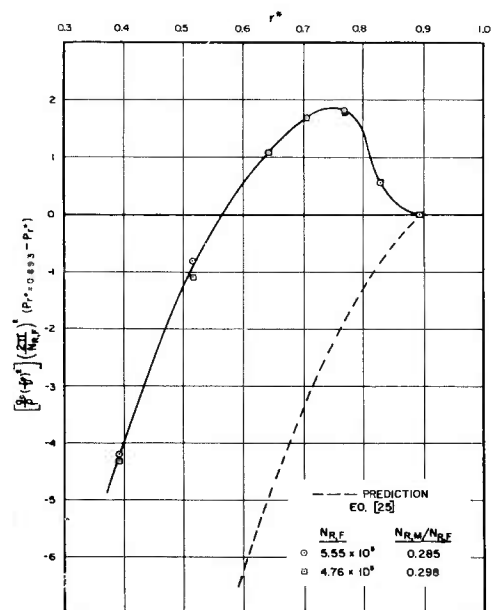
(d) Nondimensional Static Pressure,
 $N_{R,M}/N_{R,F} = 1.19$



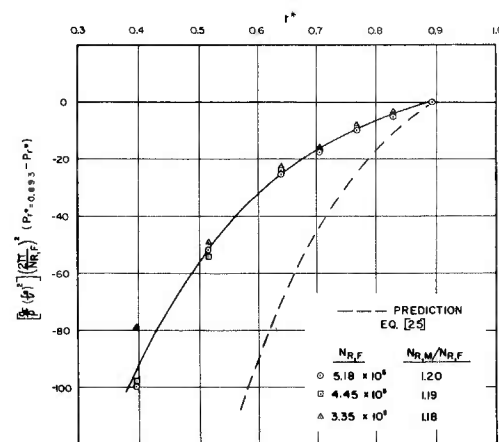
(a)



(b)



(c)



(d)

B. Radial Inflow Heat Transfer Results

The objectives of the heat transfer study are to:

1. Evaluate the technique for determining the local and average heat transfer coefficients.
2. Experimentally determine the heat transfer behavior.
3. Compare the experimentally determined heat transfer behavior with the predicted behavior.

The experimental technique was evaluated during radial inflow heat transfer tests. Therefore, the results will be presented so as to answer the objectives concurrently.

The heat transfer behavior was studied at a single shroud-to-disk clearance ratio of $z_o^* = 0.113$ over a flow Reynolds number range $N_{R,F} = 1.5 \times 10^5$ to 6.6×10^5 , and over a Reynolds number ratio range $N_{R,M}/N_{R,F} = 0.1$ to 1.7 . Average heat transfer coefficients were calculated. Local heat transfer coefficients could not be satisfactorily determined.

The average heat transfer behavior is represented by the average Stanton number, N_{St} . The following procedure was used to compute N_{St} . The average heat flux through the disk was taken as the area average of the heat fluxes measured by the heat meters. The temperature potential for heat transfer was taken as the difference between the area average disk surface temperature and the air inlet temperature. The mass velocity was determined from the air mass flow rate and the test

section inlet area, $2 \pi r_o z_o$. The average Stanton number is thus defined as:

$$N_{St} = \frac{h}{G C_p} = \frac{q'' / (t_{disk} - t_{air in})}{\left(\frac{W}{2 \pi r_o z_o} \right) C_p} \quad [11]$$

The local Stanton numbers $N_{St, l}$, were determined using the calculated local heat flux distribution at the disk test surface which is determined from the measured heat meter heat flux and the test surface temperature distribution using Eq. [D 35], Appendix D:

$$q_o'' \left(\frac{r}{r_o} \right) = 2 \int_0^1 \eta q_b''(\eta) d\eta + 2 \sum_1^{\infty} \frac{J_0 \left(\alpha_m \frac{r}{r_o} \right)}{\cosh \left(\frac{\alpha_m b}{r_o} \right) J_0^2(\alpha_m)} \\ \int_0^1 \left[q_b''(\eta) - \sinh \left(\frac{\alpha_m b}{r_o} \right) \left(\frac{\alpha_m k}{r_o} \right) t_o(\eta) \right] \eta J_0(\alpha_m \eta) d\eta \quad [12]$$

where:

- $q_o'' \left(\frac{r}{r_o} \right)$ is the test surface heat flux distribution
- $t_o(\eta)$ is the test surface temperature distribution
- $q_b''(\eta)$ is the heat meter heat flux distribution

The Burroughs 220 Digital Computer at Stanford was employed to calculate $q_o'' \left(\frac{r}{r_o} \right)$ from Eq. [12].

In the evaluation of the local Stanton numbers, the definitions of temperature difference and mass velocity are the same as those for the average Stanton numbers. The local Stanton number is thus given by:

$$N_{St,l} = \frac{h_l}{G C_p} = \frac{q_o'' \left(\frac{r}{r_o} \right) / (t_{disk} - t_{air in})}{\left(\frac{W}{2 \pi r_o z_o} \right) C_p}$$

The average heat transfer data and results are tabulated in Table I. The results are grouped according to the nominal test value of $N_{R,M}/N_{R,F}$. Runs 1 - 11 and 19 - 22 are data taken during a preliminary evaluation of the test facility. Following this evaluation, a labyrinth seal was added to the inlet section to reduce the amount of flow bypassing the rotating screens and the vaned diffuser was installed. The reason for including this earlier data will be discussed later.

The heat transfer results are presented in Fig. 30. The coordinates, $N_{St} N_{R,F}^{0.2}$ and $N_{R,M}/N_{R,F}$, are those predicted by the analysis. The data is not correlated by these parameters, as can be seen by the spread in $N_{St} N_{R,F}^{0.2}$ at any given $N_{R,M}/N_{R,F}$. The data appears to follow the trend of the analysis, showing increased heat transfer as $N_{R,M}/N_{R,F}$ increases. However, the analysis appears 50 to 100 per cent low.

Correlation of the data is obtained using a different exponent of the flow Reynolds number. This exponent is determined from cross plots of N_{St} as a function of $N_{R,F}$ for a given nominal value of $N_{R,M}/N_{R,F}$. The data are presented in this manner in Fig. 31a and Fig. 31b. The data of runs 1 - 4 and 19 - 22 were not included in the curve fitting. It was felt that the difference in inlet geometry

between the preliminary runs and the remainder of the data produced a significantly different flow pattern and precluded a comparison of the data. However, it is very interesting to note that the high $N_{R,M}/N_{R,F}$ data of runs 5 - 11 are compatible with the later data. This reinforces the flow investigation conclusions that the effect of the inlet decreases as $N_{R,M}/N_{R,F}$ increases.

Least squares straight lines were passed through the data of Fig. 31. The exponent of $N_{R,F}$ (equal to the negative of the slope) is tabulated below:

$N_{R,M}/N_{R,F}$	M (-slope)
0.15	0.598
0.31	0.592
0.50	0.591
0.66	0.536
0.99	0.546
1.27	0.525
1.66	0.458

There is a definite decrease in exponent as $N_{R,M}/N_{R,F}$ increases. While an exponent of $N_{R,F}$ that varied with $N_{R,M}/N_{R,F}$ could have been used in the correlation, it was felt that this was an unnecessary refinement. An average value of $M = 0.55$ was found to correlate the data within the experimental uncertainty.

The heat transfer results using the correlation parameter

$N_{St}N_{R,F}^{0.55}$ are presented in Fig. 32. The four to one variation in $N_{R,F}$ is seen to be very well correlated. Additionally, a least squares straight line can be passed through all of the data (excluding runs 1 - 4 and 19 - 22 as discussed previously). The heat transfer is described by the relation:

$$N_{St}N_{R,F}^{0.55} = 23.81 + 4.068 (N_{R,M}/N_{R,F}) \quad [14]$$

The standard deviation of the data about the correlation is ± 2 per cent. The 95 per cent confidence limits are ± 1.3 per cent. These values are well within the estimated experimental uncertainty of ± 4.0 per cent on $N_{St}N_{R,F}^{0.55}$ (Appendix A).

The predicted heat transfer results (Table III, p. 96), evaluated at the extremes of the $N_{R,F}$ range tested, are also shown on Fig. 32. The data is 50 to 100 per cent higher than the predicted. The effect of disk speed ($N_{R,M}$) is much less than predicted, as over the range $N_{R,M}/N_{R,F} = 0$ to 0.7, the predicted heat transfer increases by 230 per cent, while the actual rise is only 13 per cent. The actual heat transfer is surprisingly insensitive to disk speed.

The effect of adding the labyrinth seal at the sealing section and the vaned diffuser is significant only at low $N_{R,M}/N_{R,F}$. The earlier data (Runs 1 - 11 and 19 - 22) are 15 to 20 per cent low at $N_{R,M}/N_{R,F} = 0.1$, but are not measurably different at $N_{R,M}/N_{R,F} = 0.5$. This reinforces the acceptance of the present data as representative of rotating disk heat transfer.

At the higher $N_{R,M}/N_{R,F}$, the fact that flow does bypass the rotating screens has probably a small effect on the heat transfer. The effect of the bypass flow is to reduce the fluid angular momentum, producing lower relative tangential velocities between the disk and the air stream. This is analogous to testing at a disk speed ($N_{R,M}$) lower than the actual value, and the heat transfer is relatively insensitive to $N_{R,M}$ changes (Fig. 32). For the present tests, the actual angular momentum is about 70 per cent of that for no bypass flow. A corresponding 30 per cent reduction in the test value of $N_{R,M}/N_{R,F}$ would decrease the heat transfer by about 6 per cent. Complete elimination of the bypass flow would then be expected to increase the heat transfer coefficients on the order of 5 to 10 per cent over the test range.

The heat transfer coefficients of Smith (19) for radial inflow are on the order of one-tenth as large as the present results. The exponent on $N_{R,F}$ is - 0.35, compared to the present correlation exponent of + 0.55. As Smith tends to disclaim his radial inflow results, a detailed comparison of the heat transfer results was not made.

In Fig. 33, local heat transfer results for two values of $N_{R,M}/N_{R,F}$ are plotted as a function of radius (r^*). The predicted behavior for $N_{R,M}/N_{R,F} = 0.1$ is shown for comparison. The data are not self-consistent, and show little agreement with

the magnitudes and trend of the analysis. These results are typical of the attempts to obtain local heat transfer results.

These discrepancies in local heat transfer behavior are the result of inaccuracies in evaluating the terms in the series solution for the test surface heat flux. The term in Eq. [12]

$$\int_0^1 \left[q_b''(\eta) - \sinh\left(\frac{\alpha_m b}{r_o}\right) \left(\frac{\alpha_m k}{r_o}\right) t_o(\eta) \right] \eta J_0(\alpha_m \eta) d\eta$$

contains the test data. If the second term in the integrand is small relative to $q_b''(\eta)$ for the first few eigenvalues (α_m), the value of the integral will be small and the series will converge rapidly. This condition was not met for the heat transfer tests, and the higher order terms predominated. The uncertainty in the numerical integration for these higher order terms was large, and the series could not be accurately summed. The convergence would be satisfactory and the local heat transfer could be evaluated if:

- a) The test surface temperature variation $t_o(\eta)$ could be reduced to ± 0.2 F from the present test variation of ± 1 F. However, this reduction was not feasible with the present method of incident radiant energy control and the present surface temperature measurement uncertainty of ± 0.3 F.
- b) The heat flux could be increased to 5000 to 7000 BTU/hr ft² from the test values of 1000 to 1400 BTU/hr ft². The

present temperature limitations of the disk and the air flows obtainable precluded such an increase.

- c) The test disk thickness could be reduced to 0.1 to 0.2" from the present thickness of 1.682".

The following conclusions can be drawn from the radial inflow heat transfer results:

1. The experimental technique for obtaining average heat transfer coefficients is satisfactory.
2. The heat transfer did not correlate as predicted. However, the data was correlated over the entire test range by the relation:

$$N_{St} N_{R,F}^{0.55} = 23.81 + 4.068 (N_{R,M}/N_{R,F}) \quad [14]$$

The spread of the data using this correlation is less than the estimated experimental uncertainty of ± 4.0 per cent.

3. The experimentally determined heat transfer is higher and less sensitive to $N_{R,M}/N_{R,F}$ than that predicted. The possible reasons for these differences are discussed in Section VII.
4. The effects of the test section inlet and bypass flow are small, and confined to low $N_{R,M}/N_{R,F}$.

5. Local heat transfer coefficients could not be satisfactorily obtained. An increase in test heat flux or a decrease in disk thickness would be necessary to obtain local heat transfer behavior.

FIGURE 30

AVERAGE HEAT TRANSFER RESULTS FOR
RADIAL INFLOW

$N_{St} N_{R,F}^{0.2}$ AS A FUNCTION OF $N_{R,M}/N_{R,F}$

FIGURE 31

AVERAGE HEAT TRANSFER RESULTS FOR
RADIAL INFLOW

N_{St} AS A FUNCTION OF $N_{R,F}$

(a) $N_{R,M}/N_{R,F} = 0.095, 0.31, 0.66, \text{ and } 1.27$

(b) $N_{R,M}/N_{R,F} = 0.15, 0.50, 0.99, \text{ and } 1.66$

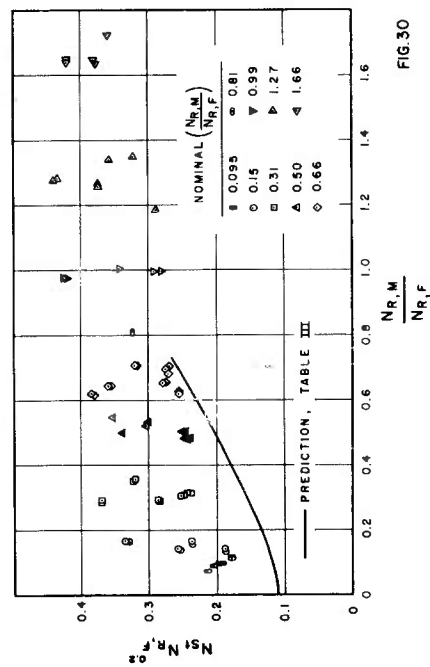


FIG 30

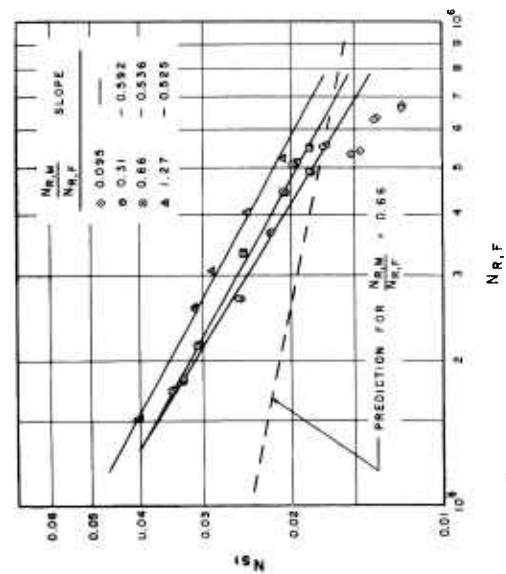


FIG 31(a)

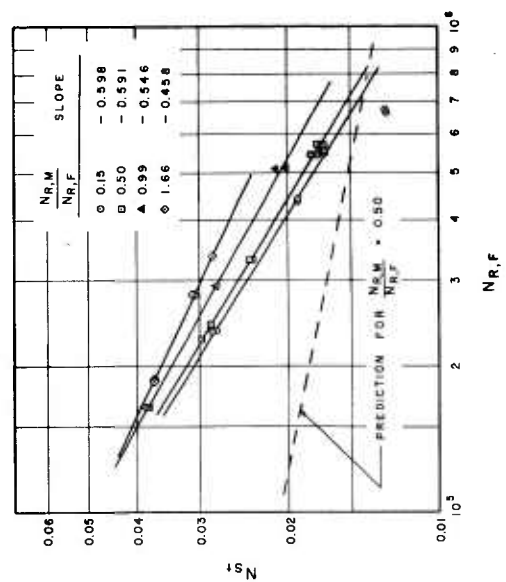


FIG 31(b)

FIGURE 32

AVERAGE HEAT TRANSFER RESULTS FOR
RADIAL INFLOW

$N_{St} N_{R,F}^{0.55}$ AS A FUNCTION OF $N_{R,M}/N_{R,F}$

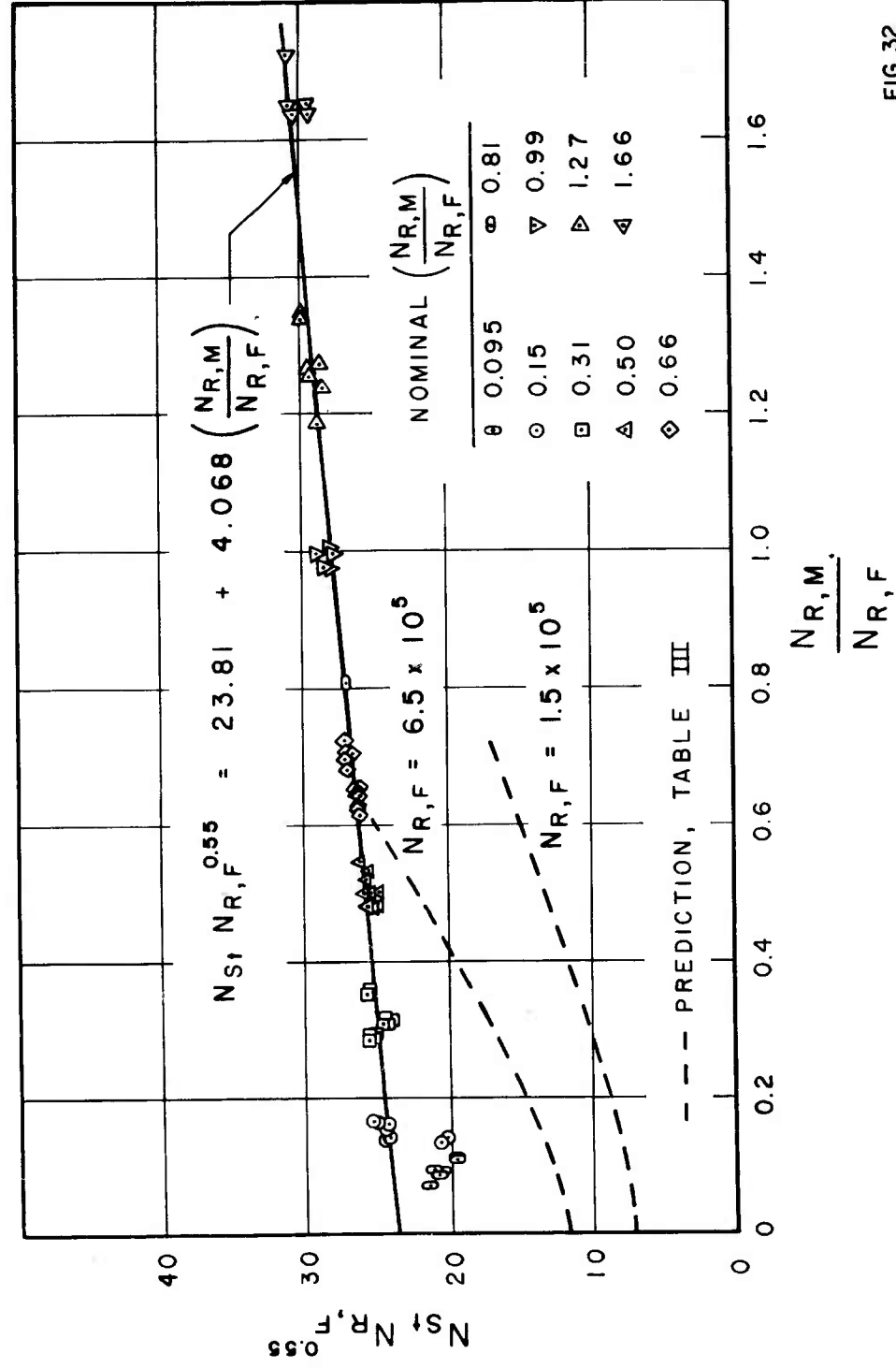


FIG. 32

FIGURE 33

LOCAL HEAT TRANSFER RESULTS
FOR RADIAL INFLOW

$N_{St,l} N_{R,F}^{0.2}$ AS A FUNCTION OF r^*

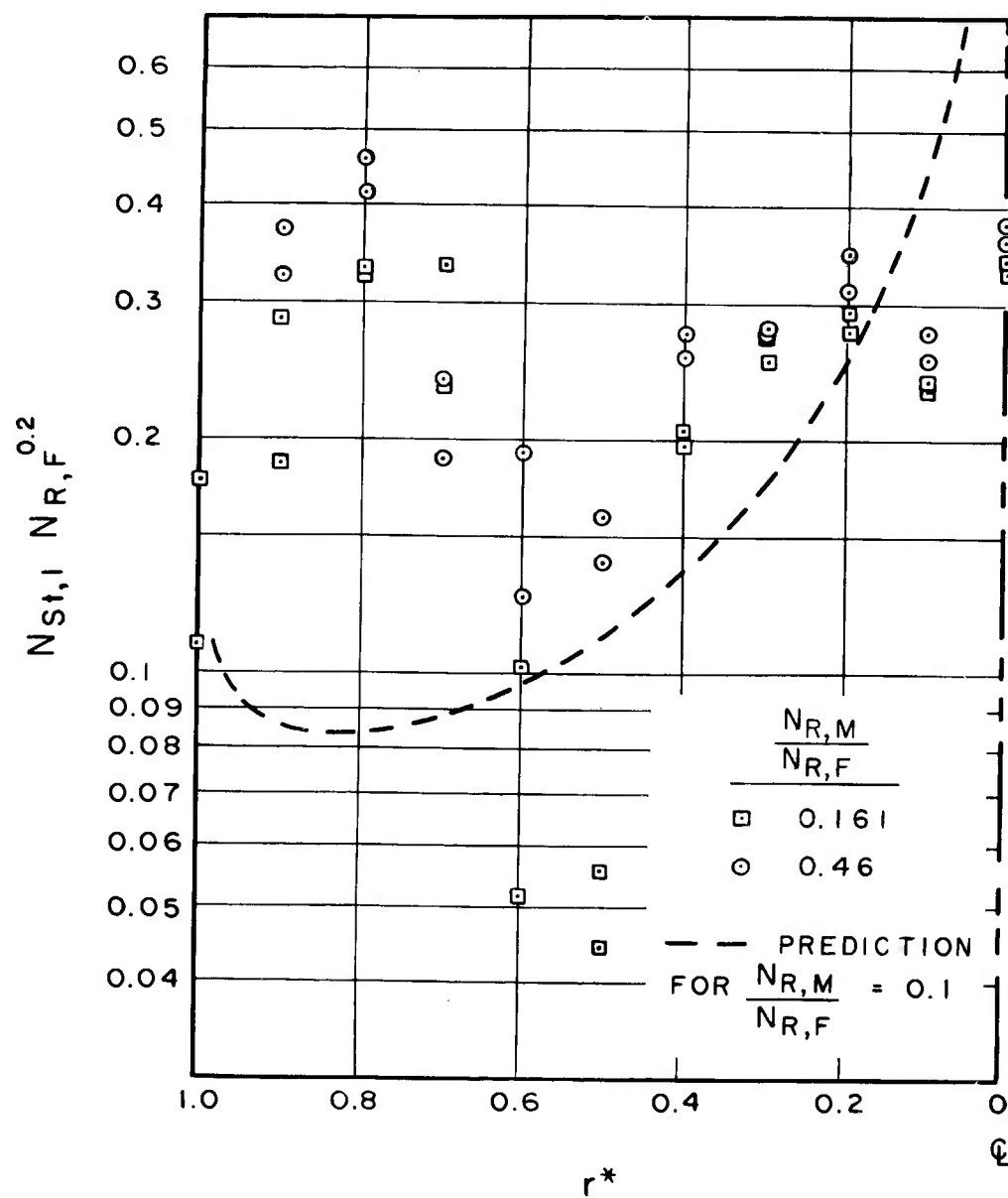


FIG. 33

TABLE I
RADIAL INFLOW HEAT TRANSFER DATA
 $z_o = 0.90"$

RUN	W	ρ	ω	t_{air}	t_{disk}	h	$N_{R,F}$	$N_{R,M}$	$\frac{N_{R,M}}{N_{R,F}}$	N_{St}	$N_{St} N_{R,F}^{0.2}$	$N_{St} N_{R,F}^{0.55}$
	lb/hr	lb/ft ³	RPM	F	F	$\frac{BTU}{hr ft^2 F}$	$\times 10^{-5}$	$\times 10^{-5}$				
19	1691	0.0736	174	76.1	125.3	20.18	5.40	0.479	0.089	0.01462	0.205	20.8
20	1680	0.0730	140	80.8	134.8	20.92	5.33	0.380	0.071	0.01526	0.214	21.5
21	1982	0.0729	220	78.1	133.9	21.91	6.31	0.600	0.095	0.01356	0.1960	21.0
22	1974	0.0728	218	79.4	135.5	22.04	6.27	0.592	0.094	0.01369	0.1975	21.1
1	2099	0.0721	275	83.1	139.7	20.77	6.64	0.736	0.111	0.01212	0.1771	19.31
2	2091	0.0720	280	84.3	140.1	20.70	6.60	0.747	0.113	0.01214	0.1770	19.30
207	796	0.0736	140	77.4	128.4	16.74	2.36	0.385	0.164	0.0277	0.329	25.0
208	795	0.0734	143	78.8	129.0	17.00	2.35	0.392	0.167	0.0282	0.335	25.4
218	1489	0.0732	220	77.8	118.3	21.43	4.41	0.602	0.137	0.01899	0.255	24.2
219	1485	0.0730	225	78.7	121.7	21.47	4.39	0.613	0.140	0.01905	0.256	24.2
220	1872	0.0725	324	80.8	125.7	23.98	5.51	0.874	0.159	0.01689	0.237	24.4
221	1866	0.0723	330	82.3	127.4	23.88	5.49	0.886	0.162	0.01686	0.237	24.2
3	2110	0.0730	332	78.4	123.8	22.00	6.72	0.905	0.135	0.01278	0.1872	20.6
4	2090	0.0726	345	80.8	126.5	21.59	6.63	0.932	0.141	0.01270	0.1869	20.2
170	623	0.0726	196	83.4	138.5	15.47	1.829	0.528	0.289	0.0328	0.369	25.7
169	623	0.0726	194	83.4	138.4	15.50	1.828	0.523	0.286	0.0328	0.369	25.7
168	915	0.0726	352	83.1	138.4	18.26	2.69	0.948	0.353	0.0263	0.320	25.5
167	916	0.0726	349	82.8	137.8	18.39	2.69	0.941	0.350	0.0265	0.322	25.7
166	1250	0.0727	396	80.8	136.2	20.83	3.68	1.072	0.291	0.0220	0.286	25.4
165	1251	0.0729	394	79.4	134.9	20.79	3.69	1.071	0.290	0.0219	0.284	25.3
164	1655	0.0730	549	77.4	129.6	22.77	4.90	1.498	0.306	0.01815	0.250	24.5
165	1658	0.0731	550	76.3	128.1	23.00	4.91	1.506	0.307	0.01830	0.252	24.7
161	1871	0.0726	645	78.0	129.3	24.50	5.53	1.750	0.316	0.01726	0.243	24.4
160	1873	0.0727	640	77.0	129.0	24.13	5.55	1.742	0.314	0.01700	0.239	24.0
209	773	0.0730	458	82.0	133.3	17.38	2.27	1.243	0.547	0.0297	0.352	26.2
210	827	0.0728	449	83.0	133.3	17.72	2.43	1.214	0.500	0.0283	0.338	26.0
211	1130	0.0725	642	84.2	131.5	20.43	3.31	1.726	0.521	0.0238	0.302	25.8
212	1128	0.0725	654	84.9	132.8	20.18	3.31	1.754	0.531	0.0236	0.300	25.6
222	1860	0.0720	1025	84.4	130.5	24.68	5.45	2.73	0.501	0.01749	0.246	24.8
223	1858	0.0719	1028	85.1	130.2	25.21	5.44	2.73	0.502	0.01789	0.252	25.4
9	1795	0.0729	1008	78.0	124.0	25.52	5.71	2.75	0.480	0.01744	0.247	25.6
10	1789	0.0729	1010	78.0	125.8	24.72	5.70	2.75	0.483	0.01694	0.240	24.8
11	1790	0.0724	1005	81.3	131.8	25.12	5.67	2.71	0.477	0.01721	0.243	25.2
172	589	0.0735	389	78.0	137.7	15.25	1.741	1.069	0.614	0.0342	0.382	26.1
173	587	0.0734	392	79.0	138.5	15.35	1.734	1.074	0.619	0.0345	0.385	26.3
174	729	0.0732	505	80.2	137.6	16.85	2.15	1.377	0.641	0.0305	0.355	26.1
175	728	0.0731	507	80.9	137.7	17.04	2.14	1.379	0.643	0.0308	0.360	26.4
176	1123	0.0736	852	77.0	130.6	21.12	3.33	2.34	0.705	0.0248	0.318	27.0
177	1122	0.0734	872	77.9	131.2	21.16	3.32	2.39	0.721	0.0249	0.318	27.1
178	1519	0.0727	1078	81.6	134.9	23.79	4.47	2.92	0.652	0.0207	0.279	26.5
179	1516	0.0726	1083	82.8	136.4	23.68	4.45	2.92	0.655	0.0206	0.276	26.4
5	1611	0.0736	1310	77.0	131.4	25.99	5.15	3.62	0.703	0.01941	0.270	26.8
6	1594	0.0731	1295	78.1	132.9	25.78	5.07	3.53	0.697	0.01980	0.274	27.2
7	1604	0.0729	1275	79.8	134.4	25.60	5.09	3.46	0.680	0.01957	0.271	27.0
180	1862	0.0720	1282	85.0	133.6	25.83	5.45	3.42	0.627	0.01830	0.257	26.2
181	1859	0.0719	1275	85.8	134.3	25.80	5.44	3.39	0.623	0.01830	0.257	26.2
171	609	0.0737	528	83.4	138.5	16.00	1.805	1.457	0.807	0.0347	0.324	27.0
213	563	0.0727	598	85.2	139.4	16.42	1.648	1.608	0.975	0.0385	0.425	28.5
214	563	0.0727	599	85.2	140.4	16.12	1.650	1.610	0.976	0.0378	0.418	28.0
215	994	0.0727	1087	83.8	132.9	20.86	2.92	2.93	1.005	0.0277	0.343	28.1
224	1744	0.0719	1912	85.7	127.4	27.87	5.10	5.08	0.996	0.0211	0.292	29.1
225	1744	0.0719	1915	85.2	128.8	26.63	5.11	5.10	0.998	0.0201	0.279	27.8
190	514	0.0733	705	79.9	134.6	15.77	1.515	1.926	1.271	0.0405	0.440	28.6
189	515	0.0733	688	79.8	135.0	15.63	1.519	1.880	1.238	0.0400	0.435	28.3
188	863	0.0737	1170	75.8	127.5	20.32	2.56	3.23	1.262	0.0311	0.375	29.4
187	866	0.0739	1163	74.6	126.5	20.40	2.57	3.23	1.255	0.0311	0.375	29.4
186	1043	0.0728	1518	80.9	134.7	22.63	3.07	4.12	1.339	0.0286	0.358	29.8
183	1363	0.0730	2000	78.3	127.9	25.43	4.05	5.45	1.346	0.0245	0.324	29.8
182	1738	0.0733	2242	74.3	120.7	27.59	5.22	6.17	1.183	0.0207	0.288	28.8
191	634	0.0731	1125	81.1	136.5	17.81	1.868	3.06	1.638	0.0370	0.420	29.4
192	634	0.0731	1132	80.9	136.3	17.81	1.867	3.08	1.649	0.0370	0.420	29.4
216	945	0.0728	1710	82.3	130.6	22.42	2.81	4.62	1.648	0.0310	0.381	30.8
217	955	0.0728	1698	82.2	130.9	22.23	2.81	4.59	1.636	0.0307	0.378	30.5
8	1064	0.0727	2147	81.4	131.8	24.46	3.37	5.81	1.721	0.0282	0.360	30.9

C. Radial Outflow Heat Transfer Results

At the conclusion of the radial inflow studies, a brief investigation of the heat transfer for forced radial outflow was conducted. The purpose of this study was to obtain heat transfer coefficients and compare them with the recently available data of Kreith, Doughman, and Kozlowski (10). A correlation obtained by Smith (19) also affords a comparison. These comparisons help in the test facility evaluation.

To obtain a radially outward flow of air through the test section, the blower connections were reversed. The blower induced air from the atmosphere and discharged into the metering section. The vaned diffuser was removed as it would have imparted a swirl to the air entering the test section. No other modifications were made.

Heat transfer coefficients were obtained at a single shroud-to-disk clearance ratio of $z_o^* = 0.113$ over a flow Reynolds number range $N_{R,F} = 1.5 \times 10^5$ to 6.5×10^5 for Reynolds number ratios of $N_{R,M}/N_{R,F} = 0.30, 0.58, \text{ and } 1.14$. The average heat transfer coefficient was determined in the same manner as for radial inflow. To afford a direct comparison with the results of (10), the heat transfer was characterized by the average Nusselt number. The average Nusselt number is defined as:

$$N_{Nu} \triangleq \frac{h r_o}{k} = \frac{r_o q''}{k (t_{\text{disk}} - t_{\text{air in}})} \quad [15]$$

The average heat transfer data and results are tabulated in Table II. The results are grouped according to the nominal test value of $N_{R,M}/N_{R,F}$. The correlation parameter suggested in (10) is designated as K.

In Fig. 34, the average Nusselt number, N_{Nu} , is presented as a function of $N_{R,F}$. The equation of the least squares straight line passing through all of the data is

$$N_{Nu} = 0.312 N_{R,F}^{0.626} \quad [16]$$

The confidence limit of the data about this line is ± 3.5 per cent. This is about equal to the estimated experimental uncertainty in N_{Nu} of ± 3.4 per cent. While there does appear to be a slight decrease in N_{Nu} with increased $N_{R,M}/N_{R,F}$, the magnitude of the decrease is about equal to the experimental uncertainty.

In Fig. 13 of (10), Sherwood number (the mass transfer parameter corresponding to the Nusselt number) is plotted as a function of $N_{R,F}/(2\pi)$ with $N_{R,M}$ as a parameter. The shroud-to-disk spacing is $z_O^* = 0.025$. These results were crossplotted to obtain N_{Nu} as a function of $N_{R,F}$ for the present nominal test values of $N_{R,M}/N_{R,F}$, and are also shown in Fig. 34.

The present results are seen to be 10 to 50 per cent lower than those of (10) over the test range. The slope of the present correlation is 0.626, while those from (10) are 0.76, 0.84, and 1.05 for

$N_{R,M}/N_{R,F} = 0.30, 0.58, \text{ and } 1.14$, respectively. The present heat transfer results are less sensitive to $N_{R,F}$ changes than those of (10).

It is surprising that there is no effect of disk rotation ($N_{R,M}$) on the present heat transfer results. Increased disk speeds would be expected to increase the heat transfer. The results of (10) show that the heat transfer increases 25 to 50 per cent over the $N_{R,M}$ range tested.

Over the z_o^* range (0.012 to 0.025) of (10), the heat transfer is correlated by $z_o^{*0.55}$. Extending this correlation to the present data where $z_o^* = 0.113$ indicated that the present heat transfer is still 25 to 80 per cent low. These discrepancies must be resolved by further tests.

The radial outflow correlation obtained by Smith (19) was evaluated for the present test conditions and is also presented in Fig. 34. The present data is again seen to be low. The agreement in slope is better; the heat transfer of (19) varies as $N_{R,F}^{0.75}$, while the present variation is $N_{R,F}^{0.626}$. A detailed comparison is not too meaningful, however, due to the large uncertainties surrounding the test procedure of Smith (19).

In (10), all of the results are correlated by the relation:

$$N_{\text{Sherwood}} (= N_{\text{Nu}}) = K = \left(\frac{z_o^*}{2} \right)^{0.55} \left[1.36 + 1.29 \left(\frac{N_{R,M}}{10^5} \right) + 3.57 \left(\frac{N_{R,M}}{10^5} \right)^2 - 3.51 \left(\frac{N_{R,M}}{10^5} \right)^3 + 1.84 \left(\frac{N_{R,M}}{10^5} \right)^4 \right] \cdot \left(\frac{N_{R,F}}{2\pi} \right)^{(0.83 - 0.12 \frac{N_{R,M}}{10^5})} \quad [17]$$

The results are presented as N_{Nu} as a function of K in Fig. 35, and are again seen to be 50 to 70 per cent low. This is compatible with the previous data comparisons.

The heat transfer behavior using the correlation parameter K of Eq. [17] is rather peculiar. This was seen by evaluating N_{Nu} using the present correlation, Eq. [16], for $N_{R,M}/N_{R,F} = 1$. This result is also shown on Fig. 35, and it is seen that for a given value of K , there are two possible values of N_{Nu} . While the present results are at some variance with those of (10), they do show the same trends on N_{Nu} and $N_{R,F}$ coordinates. These discrepancies are magnified using the correlation parameter of Eq. [17]. This reduces the usefulness of such a correlation for comparison purposes.

The possible reasons for the discrepancy between the present results and those of Kreith, et al (10) are:

- a) The present z_o^* is about four times the maximum tested in (10). The effect of z_o^* as determined in (10) may not extend outside the test range.

- b) The inlet conditions may differ. In the present test flow facility, the air flow passage had a right angle bend six diameters upstream of the test section inlet. This could affect the flow pattern entering the test section.
- c) The flow pattern in the present test section is undoubtedly different from that of (10) due to the presence of the rotating screens and sealing section. The screens probably reduce the air velocity next to the disk, while the bypass flow in the sealing section probably increases the air velocity next to the shroud. As a result, the heat transfer would be low as indicated.

The conclusions that can be drawn from the radial outflow heat transfer investigations are:

1. The present results show no effect of disk rotation ($N_{R,M}$) on the heat transfer. The heat transfer is correlated by

$$N_{Nu} = 0.312 N_{R,F}^{0.626} \quad [16]$$

2. The heat transfer coefficients are 25 - 80 per cent lower than those of (10).
3. To accurately establish the radial outflow heat transfer behavior, additional results must be obtained. The effects of the inlet, screens, and sealing section must be determined.

FIGURE 34

COMPARISON OF AVERAGE HEAT TRANSFER
RESULTS FOR RADIAL OUTFLOW

N_{Nu} AS A FUNCTION OF $N_{R,F}$

FIGURE 35

AVERAGE HEAT TRANSFER RESULTS FOR
RADIAL OUTFLOW

N_{Nu} AS A FUNCTION OF THE CORRE-
LATION PARAMETER, K

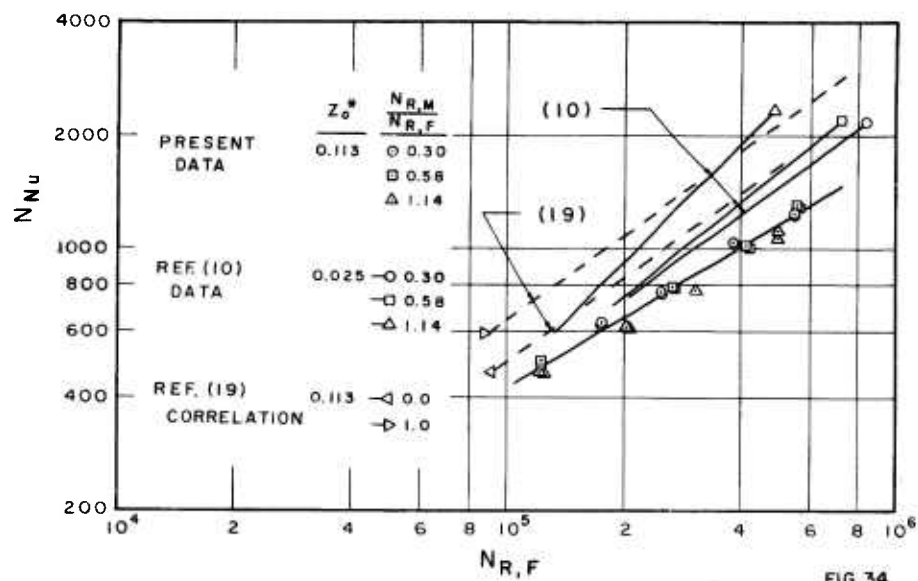
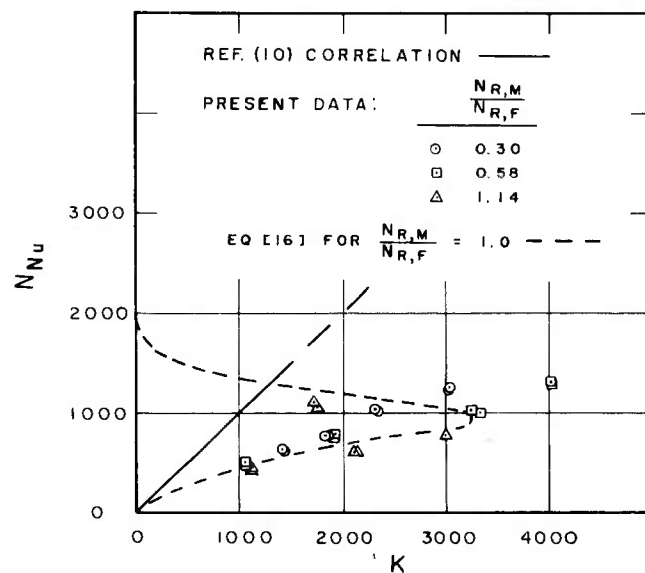


FIG. 34



$$K = \left(\frac{Z_0^*}{2}\right)^{0.55} \left[1.36 + 1.29\left(\frac{N_{R,M}}{10^5}\right) + 3.57\left(\frac{N_{R,M}}{10^5}\right)^2 - 3.51\left(\frac{N_{R,M}}{10^5}\right)^3 + 1.84\left(\frac{N_{R,M}}{10^5}\right)^4 \right] \left(\frac{N_{R,F}}{2 \cdot 10^4}\right)^{0.83} - 0.12\left(\frac{N_{R,M}}{10^5}\right)$$

FIG. 35

TABLE II
RADIAL OUTFLOW HEAT TRANSFER DATA

$z_o = 0.90"$

RUN	w	ρ	ω	t_{air}	t_{disk}	h	$N_{R,F}$	$N_{R,M}$	$\frac{N_{R,M}}{N_{R,F}}$	N_{Nu}	K
	lb/hr	lb/ft ³	RPM	F	F	$\frac{BTU}{hr ft^2 F}$	$\times 10^{-5}$	$\times 10^{-5}$			
236	609	0.0712	201	97.2	147.2	14.85	1.756	0.521	0.297	636	1420
237	609	0.0711	203	98.0	148.3	14.76	1.753	0.525	0.299	632	1417
238	873	0.0709	296	99.9	142.5	17.86	2.51	0.762	0.304	762	1814
239	883	0.0709	294	100.0	142.8	17.77	2.54	0.756	0.298	757	1831
232	1331	0.0725	440	88.9	130.1	23.53	3.88	1.175	0.303	1019	2336
233	1314	0.0722	442	91.3	131.4	24.19	3.82	1.171	0.307	1042	2311
226	1917	0.0712	620	101.3	134.5	29.32	5.49	1.600	0.291	1249	3028
227	1913	0.0712	620	101.8	135.5	28.90	5.48	1.598	0.292	1230	3023
240	427	0.0709	263	98.6	152.4	11.73	1.228	0.678	0.552	501	1076
241	427	0.0710	258	98.2	151.8	11.56	1.228	0.666	0.542	494	1076
242	937	0.0707	615	88.5	135.5	18.53	2.69	1.580	0.586	791	1911
243	932	0.0704	626	91.2	138.2	18.53	2.67	1.594	0.597	788	1908
234	1448	0.0719	965	93.8	134.4	23.24	4.19	2.54	0.606	1000	3321
235	1444	0.0716	938	96.1	135.8	23.78	4.17	2.45	0.588	1018	3247
228	1930	0.0711	1240	102.3	134.4	30.09	5.52	3.19	0.577	1280	4002
229	1929	0.0710	1240	102.6	134.0	30.77	5.52	3.18	0.577	1309	4004
244	435	0.0694	577	91.8	151.0	11.11	1.233	1.435	1.164	468	1108
245	434	0.0693	584	92.8	151.0	11.07	1.229	1.450	1.180	466	1110
246	717	0.0698	913	94.5	144.2	14.45	2.04	2.29	1.124	611	2094
247	716	0.0698	920	94.7	143.5	14.71	2.04	2.31	1.133	622	2109
249	1086	0.0699	1467	97.9	139.9	18.35	3.09	3.69	1.193	776	2993
230	1727	0.0705	2152	105.0	138.9	25.03	4.93	5.47	1.109	1060	1748
231	1739	0.0710	2147	100.9	134.1	26.12	4.99	5.52	1.107	1112	1702

K is the correlation parameter of (10).

$$K = \left(\frac{z_o}{2}\right)^{0.55} \left[1.36 + 1.29 \left(\frac{N_{R,M}}{10^5}\right) + 3.57 \left(\frac{N_{R,M}}{10^5}\right)^2 - 3.51 \left(\frac{N_{R,M}}{10^5}\right)^3 + 1.84 \left(\frac{N_{R,M}}{10^5}\right)^4 \right] \times$$

$$\left(\frac{N_{R,F}}{2\pi}\right)^{0.83 - 0.12 \left(\frac{N_{R,M}}{10^5}\right)}$$

VI ANALYTICAL INVESTIGATION

The specific objective of the analytical investigation is to predict the heat transfer behavior. As achievement of such a goal is optimistic, it is hoped that at least the study will generate the parameters governing the heat transfer, indicate the expected trends, and allow some insight into the experimentally determined fluid dynamics and heat transfer behavior.

Integral methods will be used to solve the differential equations governing the fluid dynamics and heat transfer. The Reynolds analogy will be used to relate the transfer of heat to the transfer of momentum. Boundary layers will be assumed to exist on the disk and shroud. The procedure will be to first solve for the fluid behavior external to the boundary layers. The momentum integral equation will then be solved to yield the hydrodynamic boundary layer growth and the wall shear stress. The Reynolds analogy and the energy integral equation will then be solved to evaluate the heat transfer from the rotating disk.

The following assumptions are made in the analysis:

1. The flow and heat transfer patterns are axisymmetric and steady; there are no property variations in the tangential direction.
2. The fluid behaves as an uncompressed gas; density changes due to pressure and temperature changes are small.
3. The flow is turbulent.

4. The boundary layer thickness is small compared to the disk-to-shroud spacing. The boundary layers are thin enough so that the fluid pressure varies with radius only.
5. The fluid velocity external to the boundary layers is not influenced by the boundary layers (essentially $z_o^* = \infty$).
6. The wall shear stress is given by the Blasius relation. This relation has been found to adequately describe the wall shear stress for many boundary layer flows.
7. The velocity and temperature profiles are described by 1/7th power profiles. The 1/7th power profile has been found to adequately describe the boundary layer profile in many boundary layer flows, and is compatible with the Blasius relation for wall shear stress.
8. The eddy diffusivities for heat (ϵ_H) and momentum (ϵ_M) are equal over the boundary layer. This implies that $N_{Pr} = 1$.
9. The fluid temperature at the edge of the thermal boundary layer and the disk surface temperature do not vary with radius.

These assumptions are similar to those usually made in studies of boundary layer flows. The most questionable ones are those concerning the shear stress relations and the velocity and temperature profiles. The present assumptions are made as no information is

available on the profiles for radial inflow over a rotating disk.

In an integral analysis, the heat transfer is not too sensitive to the choice of profile as the profiles are integrated over the boundary layers. The solution is more sensitive to the shear stress relation and external flow pattern. The solution and assumptions will have to be verified experimentally.

A. Behavior of the Fluid External to the Boundary Layers

The fluid behavior external to the boundary layers on the disk and shroud is described by the following equations derived for a stationary control volume located in the fluid. The coordinate system is described in Fig. 1, p. 10.

Geometry:

$$d\theta = \frac{v}{u} \frac{dr}{r} \quad [18a]$$

Continuity equation:

$$\frac{1}{r} \frac{\partial}{\partial r} (ru) = 0 \quad [19]$$

Momentum equation in the radial direction:

$$\frac{1}{g_c} \left(u \frac{\partial u}{\partial r} - \frac{v^2}{r} \right) = - \frac{1}{\rho} \frac{\partial p}{\partial r} \quad [20]$$

Momentum equation in the tangential direction:

$$\frac{1}{g_c} \left(\frac{u}{r} \frac{\partial (rv)}{\partial r} \right) = 0 \quad [21]$$

Boundary conditions:

$$\text{At } r = r_0 \quad u(r_0, z) = - \frac{W}{2 \pi r_0 z_0 \rho}$$

$$v(r_0, z) = r_0 \omega$$

$$\text{At } z = 0 \quad u(r, 0) = 0$$

$$v(r, 0) = r \omega$$

The boundary conditions correspond to those both for radial inflow turbines and for the present model. The relative fluid velocity is radial with respect to the disk at the disk periphery.

Eqs. [19] and [21] can be integrated directly. Using the boundary conditions, the fluid velocities are written as:

$$u = \frac{1}{r} \left(\frac{-W}{2 \pi z_0 \rho} \right) = - \frac{N_{R,F}}{2 \pi} \left(\frac{v}{r_0} \right) \frac{1}{r^*} \quad [22]$$

$$v = \frac{1}{r} (r_0^2 \omega) = N_{R,M} \left(\frac{v}{r_0} \right) \frac{1}{r^*} \quad [23]$$

The tangential velocity component, v , exhibits what is called free vortex flow. The angle of the resultant velocity with respect to the radial direction is

$$\tan(\alpha) = \frac{v}{u} = 2 \pi \frac{N_{R,M}}{N_{R,F}} \triangleq \beta \quad [24]$$

These results, [22], [23], and [24], are presented in Figs. 14 to 28 in comparison with the experimental results. The pressure

gradient is obtained from [20] using the fluid velocities [22]

and [23]:

$$\frac{g_C}{\rho} \frac{dp}{dr} = \left[\left(\frac{N_{R,F}}{2\pi} \right)^2 + (N_{R,M})^2 \right] \left(\frac{v}{r_O} \right)^2 \frac{1}{r^{*3}}$$

or:

$$\frac{g_C}{\rho r_O} \frac{dp}{dr^*} = \left(\frac{N_{R,F}}{2\pi} \right)^2 (1 + \beta^2) \left(\frac{v}{r_O} \right)^2 \frac{1}{r^{*3}} \quad [25]$$

Eq. [25] is presented in Fig. 29 in comparison with the experimentally determined wall static pressure variation. Eq. [18] can now be solved to compute the path of the fluid as it flows radially inward. It is more illuminating, though, to study the fluid path with respect to the disk. The relative tangential velocity and relative flow angle are related by:

$$d\theta_R = \frac{v_R}{u} \frac{dr}{r} \quad [18b]$$

where

$$v_R = v - r\omega = N_{R,M} \left(\frac{v}{r_O} \right) \frac{(1 - r^{*2})}{r^*} \quad [26]$$

The relative angle is then given by:

$$\theta_R = - \frac{2\pi N_{R,M}}{N_{R,F}} \left[\frac{r^{*2} - 1}{2} + \ln \frac{1}{r^*} \right] \quad [27]$$

Eq. [27] is plotted in Fig. 36 for various values of $N_{R,M}/N_{R,F}$. For $N_{R,M}/N_{R,F} < 0.1$, there is little effect of disk rotation on the fluid path.

B. Hydrodynamic Solution

The velocities and pressure gradient obtained for the fluid external to the boundary layer can now be used to help solve the hydrodynamic problem inside of the boundary layer. The governing equation is the radial momentum differential equation integrated over the hydrodynamic boundary layer (the integration is carried out in Appendix F). This equation is written for a stationary control volume located in the fluid:

$$\begin{aligned} \frac{-g_c}{\rho} \left[\tau_{rw} + \delta^* \frac{dp}{dr^*} \right] &= \frac{1}{r^*} \frac{d}{dr^*} \int_0^{\delta^*} r^* u^2 dz^* \\ &- \frac{u_\delta}{r^*} \frac{d}{dr^*} \int_0^{\delta^*} u r^* dz^* - \int_0^{\delta^*} \frac{v^2}{r^*} dz^* \end{aligned} \quad [28]$$

where the coordinates and the boundary layer thickness are normalized by the disk radius.

The pressure gradient is given by [25]. The fluid velocities inside of the boundary layer are assumed to vary from their absolute value at the disk to their absolute value at the edge of the boundary layer with the 1/7th power of distance:

$$u = - \frac{N_{R,F}}{2\pi} \left(\frac{v}{r_o} \right) \frac{1}{r^*} \left(\frac{z^*}{\delta^*} \right)^{1/7} \quad [29]$$

$$v = N_{R,M} \left(\frac{v}{r_o} \right) \left[r^* + \frac{(1 - r^{*2})}{r^*} \left(\frac{z^*}{\delta^*} \right)^{1/7} \right] \quad [30]$$

and the relative tangential velocity is

$$v_R = N_{R,M} \left(\frac{v}{r_0} \right) \frac{(1 - r^{*2})}{r^*} \left(\frac{z^*}{\delta^*} \right)^{1/7} \quad [31]$$

The Blasius relation for the shear stress at the disk surface in terms of the relative velocities at the edge of the boundary layer and the boundary layer thickness is assumed (Schlichting (17), p. 404). The shear stress is given as

$$\frac{g_C \tau_w}{\rho} = 0.0225 \left(\sqrt{u^2 + v_R^2} \right)_\delta^{7/4} \left(\frac{v}{\delta} \right)^{1/4} \quad [32]$$

The component of the shear stress in the radial direction is:

$$\tau_{r_w} = \tau_w \left[\frac{u}{\sqrt{u^2 + v_R^2}} \right]_w \quad [33]$$

The radial velocity is given by [29] and the relative tangential velocity by [31]. The radial component of the wall shear stress becomes:

$$\frac{g_C \tau_{r_w}}{\rho} = - \frac{0.0225}{(2\pi)^{7/4}} \left(\frac{v}{r_0} \right)^2 N_{R,F}^{7/4} \frac{\left[1 + \beta^2 (1 - r^{*2})^2 \right]^{3/8}}{r^{*7/4} \delta^{*1/4}} \quad [34]$$

The three integrals of [28] can now be evaluated using the velocity profiles [29] and [30]. Absolute velocities are used as these are momentum terms:

$$\frac{1}{r^*} \frac{d}{dr^*} \int_0^{\delta^*} r^* u^2 dz^* =$$

$$\frac{1}{r^*} \left(\frac{N_{R,F}}{2\pi} \right)^2 \left(\frac{v}{r_0} \right)^2 \frac{7}{9} \frac{d}{dr^*} \left(\frac{\delta^*}{r^*} \right)$$

[35]

$$\frac{-u_\delta}{r^*} \frac{d}{dr^*} \int_0^{\delta^*} r^* u dz^* =$$

$$-\frac{1}{r^{*2}} \left(\frac{N_{R,F}}{2\pi} \right)^2 \left(\frac{v}{r_0} \right)^2 \frac{7}{8} \frac{d\delta^*}{dr^*}$$

[36]

$$-\int_0^{\delta^*} \frac{v^2}{r^*} dz^* =$$

$$-(N_{R,M})^2 \left(\frac{v}{r_0} \right)^2 \frac{\delta^*}{36} \left[r^* + \frac{7}{r^*} + \frac{28}{r^{*3}} \right]$$

[37]

The differential equation for δ^* can be obtained by substituting [25], [34], [35], [36], and [37] into [28]. After multiplying by r^{*2} and dividing by $\left(\frac{N_{R,F}}{2\pi} - \frac{v}{r_O}\right)^2$, Eq. [28] becomes:

$$\begin{aligned} & 0.0225 \left(\frac{2\pi}{N_{R,F}}\right)^{1/4} \frac{r^{*1/4}}{\delta^{*1/4}} \left[1 + \beta^2 (1 - r^{*2})^2\right]^{3/8} \\ & - \frac{\delta^*}{r^*} (1 + \beta^2) = \frac{1}{r^*} \frac{7}{9} \frac{d}{dr^*} \left(\frac{\delta^*}{r^*}\right) \\ & - \frac{1}{r^{*2}} \frac{7}{8} \frac{d\delta^*}{dr^*} - \beta^2 \frac{(r^{*4} + 7r^{*2} + 28)}{36} \end{aligned} \quad [38a]$$

Combining terms,

$$\begin{aligned} & - \frac{7}{72} \frac{d\delta^*}{dr^*} + \frac{\delta^*}{r^*} \left[\frac{2}{9} (1 + \beta^2) - \frac{7}{36} \beta^2 r^{*2} - \frac{\beta^2}{36} r^{*4} \right] \\ & = 0.0225 \left(\frac{2\pi}{N_{R,F}}\right)^{1/4} \frac{r^{*1/4}}{\delta^{*1/4}} \left[1 + \beta^2 (1 - r^{*2})^2\right]^{3/8} \end{aligned} \quad [38b]$$

Multiplying [38b] by $\delta^{*1/4}$, and recognizing that

$$\delta^{*1/4} \frac{d\delta^*}{dr^*} = \frac{4}{5} \frac{d\delta^{*5/4}}{dr^*}$$

allows [38b] to be written as

$$\frac{d}{dr^*} (\delta^* N_{R,F}^{1/5})^{5/4} + (\delta^* N_{R,F}^{1/5})^{5/4} \left[-\frac{20}{7} \frac{(1+\beta^2)}{r^*} + \frac{5}{2} \beta^2 r^* + \frac{5}{14} \beta^2 r^{*3} \right] = -0.4579 r^{*1/4} \left[1 + \beta^2 (1 - r^{*2})^2 \right]^{3/8} \quad [39]$$

Eq. [39] is a first order differential equation linear in $(\delta^* N_{R,F}^{1/5})^{5/4}$.

It is solved with the aid of the integrating factor:

$$e^{\int \left[-\frac{20}{7} \frac{(1+\beta^2)}{r^*} + \frac{5}{2} \beta^2 r^* + \frac{5}{14} \beta^2 r^{*3} \right] dr^*} = r^*^{-\frac{20}{7}(1+\beta^2)} e^{\frac{5}{4} \beta^2 (r^{*2} + \frac{r^{*4}}{14})}$$

Eq. [39] can then be directly integrated. The initial condition on $(\delta^* N_{R,F}^{1/5})^{5/4}$ is that at $r = r_0$ ($r^* = 1$), $\delta = 0$ ($\delta^* N_{R,F}^{1/5} = 0$).

The hydrodynamic solution is:

$$(\delta^* N_{R,F}^{1/5})^{5/4} = \frac{-0.4579 \int_1^{r^*} \left(\frac{73}{28} + \frac{20}{7} \beta^2 \right) e^{\frac{5}{4} \beta^2 (r^{*2} + \frac{r^{*4}}{14})} dr^*}{r^*^{-\frac{20}{7}(1+\beta^2)} e^{\frac{5}{4} \beta^2 (r^{*2} + \frac{r^{*4}}{14})} \left[1 + \beta^2 (1 - r^{*2})^2 \right]^{3/8}} \quad [40]$$

This is an explicit relation for δ^* as a function of r^* , with $N_{R,F}$

and $\beta = 2 \pi N_{R,M}/N_{R,F}$ as parameters. In general, [40] can

not be integrated analytically, and a numerical solution must be

obtained. For the case of no rotation ($\beta = 2\pi N_{R,M}/N_{R,F} = 0$),

[40] can be directly integrated:

$$\delta^* N_{R,F}^{1/5} = 0.367 r^*^{16/7} \left(r^* - \frac{45}{28} - 1 \right)^{4/5} \quad [41]$$

In Fig. 37, the hydrodynamic boundary layer is shown as a function of radius for various values of $N_{R,M}/N_{R,F}$. The results for $N_{R,M}/N_{R,F}$ greater than zero were obtained using the Burroughs 220 digital computer at the Stanford Computation Center.* The boundary layer thickens conventionally at first, then reaches a maximum and decreases. This unusual decrease in thickness is due to fluid acceleration. As the fluid flows radially inward, the resultant velocity increases. The radial component increases due to area reduction and the tangential component to the free vortex effect. This increasing velocity thins the boundary layer. The boundary layer is thinner at the higher values of $N_{R,M}/N_{R,F}$ as the tangential velocity component is higher.

It was not possible to obtain results for $N_{R,M}/N_{R,F}$ greater than 0.7 on the computer. This resulted from the values of

$r^* - \frac{20}{7} (1 + \beta^2)$ exceeding the computer capacity at high β and low r^* .

C. Heat Transfer Solution

The heat transfer from the rotating disk is obtained using the energy integral equation and the Reynolds analogy relations. The thermal boundary layer thickness is evaluated first. The energy differential equation integrated over the thermal boundary layer is (Appendix F):

$$\frac{q_w''}{\rho C_p} = \frac{1}{r^*} \frac{d}{dr^*} \int_0^{\Delta^*} r^* u (t - t_\Delta) dz^* \quad [42]$$

In this equation, q_w'' and Δ^* are unknown. Another relation is obtained by assuming mechanistic descriptions for the transfer of heat and momentum:

$$\frac{q''}{\rho C_p} = - \epsilon_H \frac{\partial t}{\partial z} \quad [43]$$

$$\frac{g_C \tau}{\rho} = \epsilon_M \frac{\partial V_R}{\partial z} = \epsilon_M \frac{\partial}{\partial z} \sqrt{u^2 + v_R^2} \quad [44]$$

ϵ_H and ϵ_M are the diffusivities for heat and momentum in turbulent flow. The shear stress relation [44], like the Blasius relation, describes the shear in terms of the velocities with respect to the disk (relative velocities).

Because of the axial symmetry of the problem, there is no heat convected from the disk due to flow in the tangential direction. Hence the analogy between heat and momentum transfer must be written in terms of the radial shear stress. The radial component

of the shear stress is

$$\frac{g_C \tau_r}{\rho} = \epsilon_M \frac{\partial V_R}{\partial z} \times \cos \left[\begin{array}{c} \text{angle between } u \\ \text{and } V_R \end{array} \right] \quad [45]$$

$$\frac{g_C \tau_r}{\rho} = \epsilon_M \frac{\partial u}{\partial z}$$

(both u and $\sqrt{u^2 + v_R^2}$ vary as $(\frac{z^*}{\delta^*})^{1/7}$).

The Reynolds analogy assumes that the diffusivity for heat (ϵ_H) equals the diffusivity for momentum (ϵ_M) over the boundary layer. The diffusivities can then be eliminated from [43] and [44], and the wall heat flux can be written in terms of the wall shear stress:

$$\frac{q''_w}{\rho C_p} = - \left(\frac{g_C \tau_{rw}}{\rho} \right) \frac{\left. \frac{\partial t}{\partial z} \right|_{z=0}}{\left. \frac{\partial u}{\partial z} \right|_{z=0}} \quad [46]$$

Note that [46] specifies that near the wall the temperature profile must vary with the same power of distance as the velocity profile. The temperature profile will be assumed to be:

$$\left(\frac{t_w - t}{t_w - t_\Delta} \right) = \left(\frac{z^*}{\Delta^*} \right)^{1/7} \quad [47]$$

where the disk temperature, t_w , and the external fluid temperature, t_Δ , do not vary with radius.

There are now two relations, [42] and [46], for the wall heat flux and the thermal boundary layer thickness. Eq. [46] is

evaluated first. The ratio of the temperature and velocity gradients at the wall is:

$$\left[\frac{\frac{\partial t}{\partial z}}{\frac{\partial u}{\partial z}} \right]_{z=0} = \left(\frac{2\pi}{N_{R,F}} \right) \left(\frac{r_0}{v} \right) (t_w - t_\Delta) r^* \sigma^{-1/7} \quad [48]$$

With [48] and the Blasius relation for shear [34], [46] becomes:

$$\frac{q_w''}{\rho C_p} = 0.0225 \left(\frac{N_{R,F}}{2\pi} \right)^{3/4} \left(\frac{v}{r_0} \right) \frac{(t_w - t_\Delta) \left[1 + \beta^2 (1 - r^{*2})^2 \right]^{3/8}}{r^{*3/4} \delta^{*1/4} \sigma^{1/7}} \quad [49]$$

Using the assumed velocity and temperature profiles, [42] is integrated:

$$\frac{q_w''}{\rho C_p} = - \frac{(t_w - t_\Delta)}{r^*} \left(\frac{N_{R,F}}{2\pi} \right) \left(\frac{v}{r_0} \right) \frac{7}{72} \frac{d}{dr^*} (\delta^* \sigma^{8/7}) \quad [50]$$

Eqs. [49] and [50] can be equated to eliminate q_w'' , and yield a

differential equation for $\sigma = \frac{\Delta^*}{\delta^*}$:

$$- \frac{7}{72} \left[\sigma^{8/7} \frac{d\delta^*}{dr^*} + \delta^* \frac{8}{7} \sigma^{1/7} \frac{d\sigma}{dr^*} \right] = 0.0225 \left(\frac{2\pi}{N_{R,F}} \right)^{1/4} \frac{r^{*1/4} \left[1 + \beta^2 (1 - r^{*2})^2 \right]^{3/8}}{\delta^{*1/4} \sigma^{1/7}} \quad [51a]$$

Multiplying [51a] by $\sigma^{1/7}$, and recognizing that

$$\sigma^{2/7} \frac{d\sigma}{dr^*} = \frac{7}{9} \frac{d\sigma}{dr^*}$$

allows [51a] to be written as:

$$\frac{d\sigma^{9/7}}{dr^*} + \sigma^{9/7} \left[\frac{9}{8} \frac{1}{\delta^*} \frac{d\delta^*}{dr^*} \right] = - \frac{81}{7} (0.0225) \left(\frac{2\pi}{N_{R,F}} \right)^{1/4} \frac{r^{*1/4} [1 + \beta^2 (1 - r^{*2})^2]^{3/8}}{\delta^{*1/4}} \quad [51b]$$

Eq. [51b] is a first order differential equation linear in $\sigma^{9/7}$.

It is solved with the aid of the integrating factor

$$e^{\int \frac{9}{8} \frac{1}{\delta^*} \frac{d\delta^*}{dr^*} dr^*} = \delta^{*9/8}$$

With the initial condition that at $r = r_0$ ($r^* = 1$), $\delta = 0$, the solution for σ is:

$$\sigma^{9/7} = \frac{-0.413}{(\delta^* N_{R,F}^{1/5})^{9/8}} \int_1^{r^*} \frac{n^{1/4} [1 + \beta^2 (1 - n^2)^2]^{3/8} dn}{(\delta^* N_{R,F}^{1/5})^{1/8}} \quad [52]$$

This is an explicit solution for σ as a function of r^* and β only ($\delta^* N_{R,F}^{1/5}$ is a function of r^* and β only). The integral in [52] must be evaluated numerically for all values of β , with the values of $\delta^* N_{R,F}^{1/5}$ determined from the solution of [40]. With σ evaluated, the heat transfer from the rotating disk can be evaluated from either [49] or [50]. Eq. [49] is preferable as [50] involves differentiation of σ . This is considerably less accurate in a numerical solution than raising σ to the 1/7th power.

The solution of [52] yields values of the boundary layer

ratio $\sigma = \Delta^*/\delta^*$ greater than unity. σ is 1 at $r^* = 0$, on the order of 5 at $r^* = 0.5$, and increases indefinitely as r^* decreases toward zero. This contradicts the implicit assumption of [42], where Δ^* is assumed to be less than δ^* so that the 1/7th power velocity profile applies over the range of integration. Eq. [42] could be corrected by integrating from 0 to δ^* using the 1/7th power velocity profile and from δ^* to Δ^* using the velocity u_δ . A nonlinear differential equation in $\sigma^{9/7}$ would then result, and a solution would have to be obtained numerically. The extra effort was not felt worthwhile as the solution is approximate and based on some unverified assumptions. Also, as σ appears to the 1/7th power, large errors in evaluating σ will not affect the heat transfer proportionately.

Defining a local Stanton number,

$$N_{St,1} \triangleq \frac{q''_w}{(t_w - t_\Delta)} \frac{1}{\left(\frac{W}{2\pi r_o z_o}\right) C_p}$$

[49] can be written as:

$$N_{St,1} N_{R,F}^{0.2} = \frac{0.0357}{r^{*3/4}} \frac{\left[1 + \beta^2 (1 - r^{*2})^2\right]^{3/8}}{(\delta^* N_{R,F}^{1/5})^{1/4} \sigma^{1/7}} \quad [53]$$

In this analysis, it has been assumed that $\epsilon_H = \epsilon_M$ everywhere. This implies that $N_{Pr} = 1$. However, a N_{Pr} effect can be included if it is assumed that the effect of N_{Pr} on the

rotating disk heat transfer is the same as on turbulent flat plate heat transfer. This is logical, as both flows are essentially turbulent boundary layer flows. For the N_{Pr} range of gases, the effect of N_{Pr} is felt as $N_{Pr}^{0.4}$. "Correcting" [53] for the N_{Pr} effect yields the final relation for heat transfer:

$$N_{St,l} N_{Pr}^{0.4} N_{R,F}^{0.2} = \frac{0.0357 [1 + \beta^2 (1 - r^{*2})^2]^{3/8}}{r^{*3/4} (\delta^* N_{R,F}^{1/5})^{1/4} \sigma^{1/7}} \quad [54]$$

For air, $N_{Pr} = 0.7$, and [54] becomes:

$$N_{St,l} N_{R,F}^{0.2} = \frac{0.0411 [1 + \beta^2 (1 - r^{*2})^2]^{3/8}}{r^{*3/4} (\delta^* N_{R,F}^{1/5})^{1/4} \sigma^{1/7}} \quad [55]$$

This defines the local heat transfer from a rotating disk.

The right hand side is a function of r^* and $N_{R,M}/N_{R,F}$ only.

$(\delta^* N_{R,F}^{1/5})$ is obtained from the solution of [40], and σ from the solution of [52].

In Fig. 38, $N_{St} N_{Pr}^{0.4} N_{R,F}^{0.2}$ is presented as a function of r^* for various $N_{R,M}/N_{R,F}$. The heat transfer is seen to decrease at first, and then increase indefinitely as the radius decreases. The initial decrease is similar to that for a flat plate; as the hydrodynamic boundary layer thickens, the heat transfer decreases. However, as the fluid flows radially inward, the fluid accelerates, which thins the hydrodynamic boundary layer and increases the heat transfer coefficient. The heat transfer

coefficient increases indefinitely near the disk center as here the fluid velocity becomes indefinitely large.

The average heat transfer is obtained by integrating the local heat transfer coefficient over the disk area. The average Stanton number is thus related to the local Stanton number by:

$$N_{St} N_{Pr}^{0.4} N_{R,F}^{0.2} = \int_0^1 (N_{St,l} N_{Pr}^{0.4} N_{R,F}^{0.2}) d(r^{*2}) \quad [56]$$

Eq. [54] is used to evaluate the integrand, which is a function of r^* and $N_{R,M}/N_{R,F}$ only. The integration is performed numerically.

At the limits of integration, $N_{St,l}$ becomes infinite. At the upper limit, the difficulty is circumvented by simplifying [54]. For r^* close to unity, some of the terms in [54] are small relative to the remaining terms and can be neglected. Eq. [56] can then be analytically integrated over the range $r^* = 0.99$ to 1.00 with an accuracy of about 0.1 per cent. At the lower limit, the effect of the singularity is small for $N_{R,M}/N_{R,F} = 0$, and the integral can be integrated numerically. For $N_{R,M}/N_{R,F}$ greater than zero, the value of the integral from an arbitrary lower limit to $r^* = 1$, normalized by the value of the integral over the same range for $N_{R,M}/N_{R,F} = 0$, can be numerically evaluated and plotted as a function of the lower limit. Extrapolation to $r^* = 0$ allows the evaluation of the average heat transfer behavior.

The average heat transfer results obtained in this manner

are:

TABLE III
ANALYTICAL RADIAL INFLOW HEAT TRANSFER
RESULTS

$N_{R,M}/N_{R,F}$	$N_{St} N_{Pr}^{0.4} N_{R,F}^{0.2}$	$N_{St} N_{R,F}^{0.2}$ ($N_{Pr} = 0.7$)
0	0.0948	0.1089
0.1	0.1018	0.1169
0.3	0.1368	0.1570
0.5	0.1768	0.2030
0.6	0.2000	0.2298
0.7	0.2183	0.2507

The average heat transfer results are presented in Figs. 30, 31 and 32 in comparison with the experimental results. The discrepancies between analysis and experiment are discussed in Section VII.

D. Effect of Shroud-to-Disk Spacing on Heat Transfer

If the disk-to-shroud spacing is finite, the boundary layers on the disk and shroud will increase the velocity of the fluid external to the boundary layers. The boundary layer growth and, consequently, the heat transfer will be affected. The amount of

the velocity increase is determined from continuity considerations. The effect on the heat transfer can be estimated from the increased velocity.

The velocity increase is evaluated from the continuity equation.

The flow rate is given by:

$$W = \int_0^{z_0} 2\pi r \rho u dz$$

$$= -2\pi r \rho \left[\int_0^{\delta_{\text{disk}}} u dz + u_{\delta} (z_0 - \delta_{\text{disk}} - \delta_{\text{shroud}}) + \int_{\delta_{\text{shroud}}}^{z_0} u dz \right]$$

Assuming that $\delta_{\text{disk}} = \delta_{\text{shroud}} = \delta$, as the boundary layer thicknesses are small, and using the 1/7th power velocity profiles inside of the boundary layers, the flow rate becomes:

$$W = -2\pi \rho r r_0 u_{\delta} (z_0^* - \frac{\delta^*}{4}) \quad [57]$$

The velocity of the fluid external to the boundary layer is then:

$$u_{\delta} = - \frac{W}{2\pi \rho r r_0 (z_0^* - \frac{\delta^*}{4})} \quad [58]$$

The velocity assumed in the analysis is:

$$u_{\delta} \Big|_{z_0^* = \infty} = - \frac{W}{2\pi \rho r r_0 z_0^*} \quad [59]$$

The ratio of the two velocities is:

$$\frac{u_{\delta}}{u_{\delta} \Big|_{z_0^* = \infty}} = \frac{1}{(1 - \frac{\delta^*}{4 z_0^*})} \quad [60]$$

The effect of the shroud spacing is largest at the large δ^* which

occur at low $N_{R,M}/N_{R,F}$, and at the small disk-to-shroud spacings.

The effect of the velocity increase on heat transfer can be estimated. The heat transfer coefficient, h , is proportional to $N_{St} N_{R,F}$. From [54], $N_{St} N_{R,F}$ is proportional to $N_{R,F}^{0.8}$. Therefore, h is proportional to $N_{R,F}^{0.8}$. An increase in velocity due to boundary layer growth can be thought of as an increase in velocity due to increased flow rate ($N_{R,F}$). The effect of the shroud-to-disk spacing on the heat transfer can then be estimated as:

$$\frac{h}{h)_{z_O^* = \infty}} = \frac{N_{St}}{N_{St})_{z_O^* = \infty}} = \left(\frac{u_\delta}{u_\delta)_{z_O^* = \infty}} \right)^{0.8} \quad [61]$$

where $u_\delta / u_\delta)_{z_O^* = \infty}$ is evaluated from [60].

For $z_O^* = 0.1$ and $N_{R,F} = 10^5$ (the minimum values to be studied experimentally), and for $N_{R,M}/N_{R,F} = 0$, the increase in heat transfer is about 3 per cent at most. Because δ^* decreases at higher values of $N_{R,M}/N_{R,F}$, the effect will decrease as $N_{R,M}/N_{R,F}$ increases. This leads to the important conclusion that z_O^* may not be an important parameter in the flow and heat transfer studies. Elimination of z_O^* as a parameter would considerably reduce the length of the experimental investigation. This conclusion must be verified experimentally.

E. Conclusions

The conclusions that can be drawn from the results of the analytical investigation are:

1. The problem of heat transfer from a shrouded rotating disk has been attacked using integral techniques. The relation between the nondimensional parameters has been predicted. There is considerable disagreement between the analytical and experimental fluid dynamics and heat transfer behavior.
2. The predicted effect of the shroud-to-disk spacing, z_O^* , on the heat transfer is small. The predicted heat transfer for $z_O^* = 0.1$ is at most only 3 per cent higher than that for $z_O^* = \infty$. The lack of an effect of the disk-to-shroud spacing will have to be verified experimentally.
3. The present analytical results will apply to a rotating disk with closely spaced vanes. If it is assumed that the vanes prevent any relative tangential movement ($v = r\omega$ everywhere), the same solution as for $N_{R,M}/N_{R,F} = 0$ is obtained. However, on a vaned rotating disk there would probably be a secondary flow, although not of the same magnitude as found on the unvaned disk. The effect of vanes on the heat transfer behavior will have to be determined experimentally.

FIGURE 36

PREDICTED FLOW PATHS WITH RESPECT
TO THE DISK

FIGURE 37

ANALYTICAL HYDRODYNAMIC SOLUTION

$\delta^* N_{R,F}^{0.2}$ AS A FUNCTION OF r^*

FIGURE 38

ANALYTICAL HEAT TRANSFER SOLUTION

$N_{St,l} N_{Pr}^{0.4} N_{R,F}^{0.2}$ AS A FUNCTION OF r^*

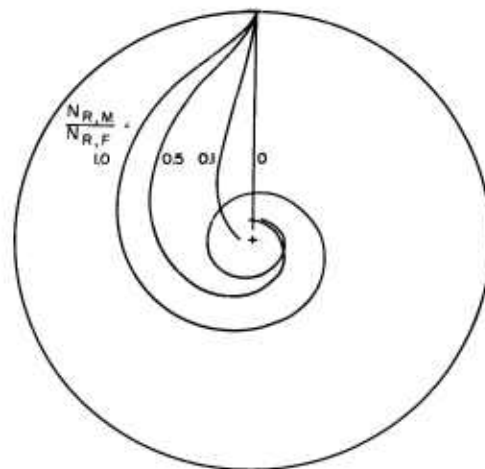


FIG. 36

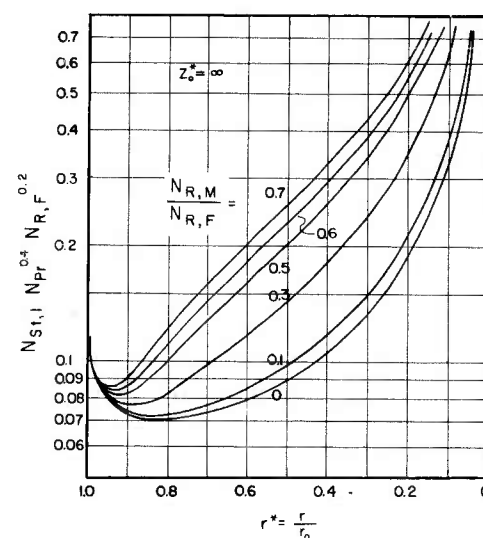


FIG. 37 38

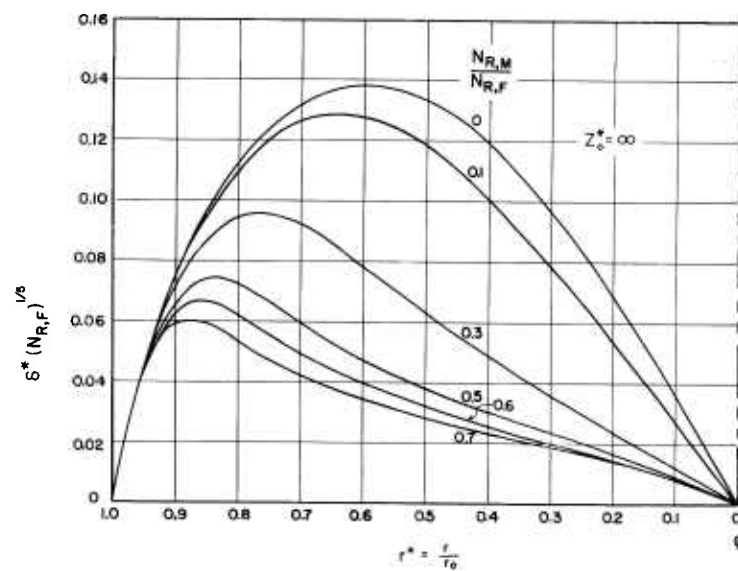


FIG. 38 37

VII DISCUSSION OF RESULTS

The analytical and experimental heat transfer results differ significantly in the magnitudes of the heat transfer coefficients and of the Reynolds number exponents. The discrepancies are due to some oversimplifications made in the analysis. The assumptions will be examined in light of the experimental results.

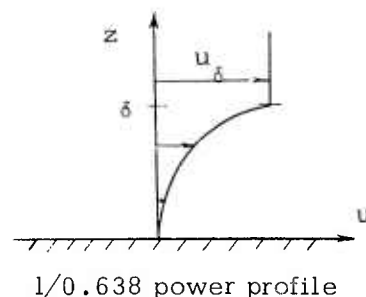
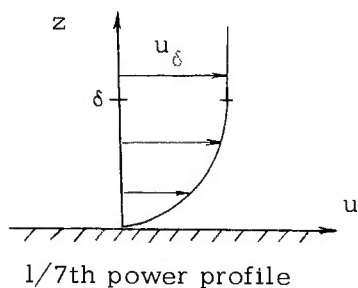
The assumption of axial symmetry is experimentally verified for $N_{R,M}/N_{R,F}$ greater than 0.3. The assumptions concerning the details of the boundary layer flow are quite reasonable. The boundary layer flow is wall dominated; there are no wakes or jets to influence the boundary layer. This implies that the "law of the wall" (1/7th power velocity and temperature profiles) is valid.

The most questionable simplifications are those concerning the influence of the disk and shroud boundary layers on the flow pattern. The assumed influence is an increase in the one-dimensional fluid velocity external to the boundary layers due to the reduced velocities in the boundary layers. The actual effect is that the shear stresses on the disk and shroud reduce the fluid angular momentum near the two surfaces. The resulting unbalance in centrifugal force field across the flow passage forces the fluid to flow radially outward in the passage center, as shown in Fig. 20. This influence of the surfaces is similar to that on the flow between rotating concentric cylinders, in which a system of counterrotating vortices

unexpectedly is formed, (24).

The flow pattern is thus governed by the presence of the disk and shroud. The flow can not be considered as an external flow with boundary layers on the surfaces. While the boundary layer profile is quite probably of the $1/7$ th power form, the radial velocity in the boundary layer does not approach $\frac{N_{R,F}}{2\pi} \frac{v}{r_0} \frac{1}{r^*}$ as assumed (Eq. [29]). This is seen in Figs. 14 to 18, where the external one-dimensional velocity does not characterize the velocity profiles.

This breakdown of the concept of an external flow with boundary layers is reinforced by the comparison between the experimental and the predicted heat transfer. The heat transfer exponent is directly related to the velocity profile power in a boundary layer analysis. A $1/n$ power profile yields a $2/(n+3)$ power on Reynolds number; a $1/7$ th power yields $N_{R,F}^{0.2}$. The velocity profile power corresponding to the experimentally determined 0.55 power on $N_{R,F}$ would be $1/0.638$. This order of magnitude difference in exponent and the reversed curvature of the profile are physically unrealistic.



The heat transfer coefficients are based on the measured temperature difference between the disk and the air stream inlet. At high $N_{R,M}$ and $N_{R,F}$, the disk is rotating rapidly and the relative velocities are quite high. As a result, the difference between the adiabatic wall temperature and the ~~disk~~^{air} temperature is significant for some test conditions. The difference between the two temperatures is given by:

$$(t_{\text{adiabatic wall}} - t_{\text{air}}) = N_{Pr}^{1/3} \frac{V_R^2}{2 g_C C_p} \quad [62]$$

where $N_{Pr}^{1/3} = 0.9$ is the recovery factor for turbulent radial outflow over a rotating disk (23). As the fluid relative velocity V_R is a function of radius, the temperature difference as a function of radius must be evaluated and an area average value obtained.

The maximum computed average difference between $t_{\text{adiabatic wall}}$ and t_{air} is 1.8 F, increasing the heat transfer coefficient by about 4 per cent over the reported values. However, as the temperature difference decreases both as $(N_{R,M})^2$ and $(N_{R,F})^2$ decrease, the effect on the heat transfer coefficients decreases rapidly. For about 90 per cent of the heat transfer data, the effect on the heat transfer coefficient is less than 1 per cent. Therefore, the data was not corrected for this effect.

The fluid dynamics investigation was conducted with the disk and air stream at the same temperature, while in the heat transfer

studies a temperature difference existed. The flow patterns in these two studies were possibly different due to the free convection effect of the centrifugal force field on the density differences present in the heat transfer study.

The parameter characterizing the free convection is the Grashof number:

$$N_{Gr} = \frac{g \beta r_o^3 \rho^2 (t_{disk} - t_{air})}{\mu^2}$$

For the disk tests, the acceleration, g , is the centrifugal acceleration $r_o \omega^2$. Using the ideal gas relation for the coefficient of thermal expansion, $\beta = 1/T$, the Grashof number can be written as:

$$N_{Gr} = N_{R,M}^2 \frac{(t_{disk} - t_{air})}{T_{air}}$$

or

$$N_{Gr} = 0.09 N_{R,M}^2$$

over the rotating disk test range.

The parameter characterizing the through flow in the same manner as does the length Reynolds number for flow over a flat plate is:

$$\frac{N_{R,F}}{2\pi}$$

The flow produced by the free convection effect is in the same direction as the through flow. As the centrifugal force acts

radially outward, the less dense (higher temperature) air next to the disk is forced radially inward. Eckert and Diaguila have established the following criteria for the combined effects of free and forced convection on flat plate heat transfer (5):

For a deviation in the heat transfer of less than 10 per cent from pure free convection:

$$\frac{N_{Gr}}{0.007 (N_{Re})^{2.5}} \geq 1$$

or

$$\frac{1300}{N_{R,F}^{0.5}} \cdot \left(\frac{N_{R,M}}{N_{R,F}} \right)^2 \geq 1 \quad [63]$$

For a deviation in the heat transfer of less than 10 per cent from pure forced convection:

$$\frac{0.0016 (N_{Re})^{2.5}}{N_{Gr}} \geq 1$$

or

$$0.00018 N_{R,F}^{0.5} \left(\frac{N_{R,F}}{N_{R,M}} \right)^2 \geq 1 \quad [64]$$

Evaluating these criteria over the heat transfer test range yields the following flow divisions:

$N_{R,M}/N_{R,F}$	Type of Flow
0.31	Forced convection
0.66	Forced and free convection
0.99	Free convection

At high $N_{R,M}/N_{R,F}$, the flow pattern would be expected to be dominated by the free convection current. However, an attempt to predict the disk heat transfer using flat plate convection correlations was unsuccessful. The predicted free convection coefficients are one-third to one-half those measured, and differ considerably in their dependence on $N_{R,M}$ and $N_{R,F}$. This lack of correspondence at high $N_{R,M}/N_{R,F}$ may imply that the flat plate free convection criteria are not applicable to the rotating disk flow.

The free convection effect on the present heat transfer results is probably small. The heat transfer results of Fig. 31 show essentially the same dependence of N_{St} on $N_{R,F}$ over the entire $N_{R,M}/N_{R,F}$ range. This would not be expected if regimes of forced convection, forced and free convection, and free convection occurred as $N_{R,M}/N_{R,F}$ increased. At high $N_{R,M}/N_{R,F}$, the through flow Reynolds number $N_{R,F}$ would then not be significant, and the heat transfer data would then be correlated by the Grashof number, or $N_{R,M}$. The present correlation of the heat transfer data over the test range of $N_{R,M}/N_{R,F}$ strengthens the acceptance of the present radial inflow heat transfer results as representative of rotating disk heat transfer.

VIII CONCLUSIONS

The following conclusions can be drawn from the results of the present investigation:

1. A test facility has been constructed that will allow determination of the average heat transfer from a rotating disk. The facility is adaptable to studies of various flow configurations.
2. The flow pattern for a rotating disk with a single radial inflow has been experimentally determined. The presence of the disk and shroud have been shown to govern the fluid behavior.
3. The heat transfer from a rotating disk with a single radial inflow has been experimentally determined. At a disk-to-shroud clearance ratio of $z_o^* = 0.113$ and over a $N_{R,F}$ range of 1.5×10^5 to 6.6×10^5 and a $N_{R,M}/N_{R,F}$ range of 0.1 to 1.7, the heat transfer is correlated by

$$N_{St} N_{R,F}^{0.55} = 23.81 + 4.068 (N_{R,M}/N_{R,F}) \quad [14]$$

4. The analytical investigation did not adequately predict the fluid dynamics and heat transfer behavior. The assumptions regarding the interaction between the disk and shroud boundary layers and the main flow were oversimplified.

IX RECOMMENDATIONS FOR FURTHER WORK

The following recommendations for further work are made:

1. The test facility should be improved to eliminate the flow leakage past the rotating screens. The possibility of modifying the facility to permit the determination of local heat transfer coefficients should be considered.
2. The effect of free convection on the rotating disk heat transfer should be determined. This would necessitate obtaining velocity profiles during heat transfer tests.
3. An investigation of the details of the boundary layer flow on the disk should be performed. This study, coupled with a more realistic analytical approach, should yield more insight into the fluid behavior.
4. Other rotating disk flow configurations should be studied in an approach to the modeling of the veil-cooled radial flow gas turbine. A logical sequence is:
 - a) The rotating disk with a veil flow and a main flow.
 - b) A vaned rotating disk with a single radial inflow.
 - c) A vaned rotating disk with a veil flow and a main flow.

X APPENDICES

Appendix A Experimental Uncertainties

The following uncertainties are considered representative for the rotating disk test range.

1. Dimensions

At 20:1 odds, the uncertainty intervals are estimated to be:

r_o	7.979" \pm 0.001"	\pm 0.01%
z_o	0.900" \pm 0.010"	\pm 1.1%
Disk area		\pm 0.02 %

2. Fluid Properties

At 20:1 odds, the uncertainty intervals for the fluid properties are estimated to be:

T	540 R \pm 0.1 R	\pm 0.02%
p	30"Hg \pm 0.05"Hg	\pm 0.2%
ρ	\pm 0.2%	
C_p	\pm 0.2%	
μ	\pm 0.2%	
k	\pm 0.3%	

3. Air Flow Rate, \dot{W}

The air flow metering section was constructed according to the specifications of the A.S.M.E. Power Test Code (1).

The metering section was calibrated against a standard flow metering tank. The metering section orifice coefficient was computed using the flow rates determined from the flow meter tank and the pertinent temperatures and pressures measured at the orifice. The calibrated coefficient was then compared to that tabulated in (1).

At 20:1 odds, the flow rate uncertainty interval is estimated to be:

$$W \quad \pm 1.6\%$$

4. Disk Angular Velocity, ω

The disk angular velocity was measured with a General Radio Strobotac calibrated to $\pm 1\%$. The variation in disk speed during a test is estimated to be $\pm 1\%$. At 20:1 odds, the disk angular velocity uncertainty interval is estimated to be:

$$\omega \quad \pm 1.5\%$$

5. Heat Flux Through the Disk, q''

The uncertainty in the heat flux passing through the disk is estimated from computations of the disk thermal resistance. The thermal resistance is defined as the temperature difference between the heat meter and test surface thermocouples divided by the heat flux. The thermal resistance was continuously

evaluated during calibration and testing. The variation in thermal resistance is assumed to be due solely to heat flux measurement uncertainties.

At 20:1 odds, the heat flux uncertainty interval is estimated to be:

$$q'' \quad \pm 2.0\%$$

6. Temperature Difference Between Disk Test Surface And Air Stream

The copper-constantan thermocouples were calibrated against primary standard thermometers in a controlled temperature oil bath. At 20:1 odds, the air temperature uncertainty is estimated to be:

$$t_{\text{air}} \quad \pm 0.1 \text{ F}$$

The uncertainty in a single disk surface temperature measurement due to extraneous EMF's in the garter spring pickup and to uncertainties in the calibration is $\pm 0.3 \text{ F}$. The test surface temperature variation is on the order of $\pm 1.0 \text{ F}$. The estimated test surface temperature uncertainty is then

$$t_{\text{disk}} \quad \pm 1.3 \text{ F}$$

At 20:1 odds, the estimated uncertainty of the temperature difference between the disk and the air stream is

estimated to be:

$$t_{\text{disk}} - t_{\text{air}} = 50 F \pm 1.4F = \pm 2.8\%$$

7. Nondimensional Parameters

At 20:1 odds, the estimated uncertainties in the non-dimensional parameters are:

$$N_{\text{Nu}} \quad \pm 3.4\%$$

$$N_{\text{R},\text{F}} \quad \pm 1.7\%$$

$$N_{\text{R},\text{M}} \quad \pm 1.5\%$$

$$N_{\text{St}} \quad \pm 3.9\%$$

$$N_{\text{St}} N_{\text{R},\text{F}}^{0.55} \quad \pm 4.0\%$$

Appendix B Fluid Velocity Measurement Errors

The velocity and flow angle measurements are subject to a number of possible errors. The greatest source of error in the velocity determination stems from the method of measuring the dynamic pressure. The velocity probe is equipped to sense total pressure only; the static pressure must be measured separately. With the probe mounted in the flow passage, the wall static pressure can not be measured at the same location as the total pressure. Therefore, to obtain a dynamic pressure measurement, the following procedure was used.

The total pressure tap was connected to one leg of a differential manometer. A wall pressure tap at the same radius as the probe, but at a different circumferential position, was connected to the other leg of the manometer. A velocity traverse across the flow passage was then made, and the pressure difference recorded. At the same test conditions, the difference in static pressure at the wall between the static and total pressure measuring locations was measured. The dynamic pressure was then corrected for this difference so that the total and static pressure were determined at the same location. The correction varied between 1 and 30 per cent of the dynamic pressure. The resulting uncertainty in the velocity is estimated to be ± 3 per cent.

The uncertainty in the dynamic pressure is further increased

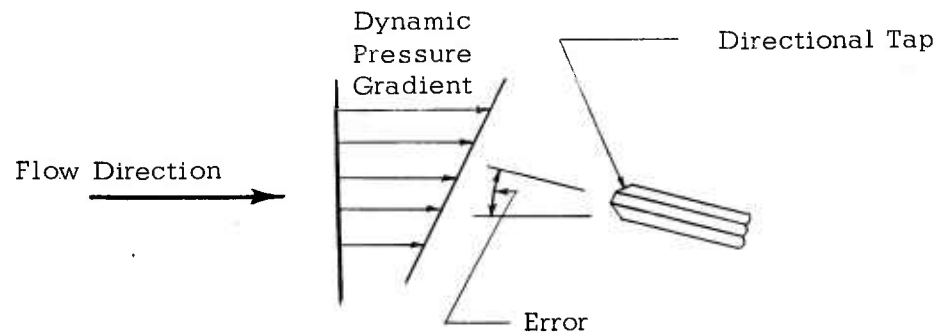
in that the static pressure could not be measured at the same point in the flow passage as the dynamic pressure. As seen in Figs. 14 to 18, the velocity variation across the passage is large, and a static pressure variation would also be expected. No estimation of the static pressure variation was made.

The large velocity variations across the flow passage cause a curving of the streamlines in the vicinity of the probe. The higher velocities shift toward the probe tip; the probe measures a velocity higher than actually exists in the absence of the probe. The fluid displacement is on the order of 0.02", but is not known accurately enough to correct the traverse results.

The probe was calibrated in a wind tunnel for flow angle measurements to $\pm 0.25^\circ$. The uncertainty in reading the protractor is $\pm 0.25^\circ$. The uncertainty interval for flow angle measurements due to instrument uncertainties is $\pm 0.5^\circ$.

The flow angle measurements are sensitive to velocity gradients normal to the probe axis. At high $N_{R,M}/N_{R,F}$, the flow is essentially in the tangential direction, and the velocity gradient in the radial direction is large, as shown in the following figure. Consequently, the two directional taps, which are separated by the probe diameter, may be in regions of different total pressure. At a null pressure indication, the probe is then orientated so that the tap in the low total pressure region measures a higher component

of the dynamic pressure than does the other tap. The probe is thus rotated too far in the direction of the higher velocities. This flow angle error is estimated to be within 2° for the rotating disk tests.



The radial velocity uncertainty is largest at high $N_{R,M}/N_{R,F}$. The radial velocity is obtained from the product of the resultant velocity and the sine of the flow angle. For $N_{R,M}/N_{R,F}$ greater than 0.6, the flow angle is between 80° and 100° . An uncertainty of $\pm 0.5^\circ$ results in a radial velocity uncertainty on the order of ± 25 per cent.

Appendix C Data Reduction Procedure

A Burroughs 220 digital computer was used to reduce the data with the exception of the mean heat transfer data. Separate programs were written for the computation of $N_{R,F}$ and $N_{R,M}/N_{R,F}$, and for the determination of the velocity profiles. These programs are written in the Balgol language.

1. Evaluation of $N_{R,F}$ and $N_{R,M}/N_{R,F}$

The following table gives the translation between the present nomenclature and that used in the computer program.

ATM	denotes atmospheric conditions
D, O, or OR	denotes orifice conditions
I	denotes inlet conditions
DM	density correction factor for humidity
DO	orifice diameter
DPO	pressure drop across the orifice
KO	orifice coefficient
MU	dynamic viscosity
MV	temperature in millivolts
R	density
P	pressure
T	temperature in F
YO	orifice expansion factor

MFLO	W , mass flow rate
NRF	$N_{R,F}$
NRM	$N_{R,M}$
NRM/NRF	$N_{R,M}/N_{R,F}$
RPM	ω , disk angular velocity
RUN	Run number
ZO	z_o

Empirically determined relations for KO, MU, T, and YO were employed. The machine program follows.

```

COMMENT DISK FLOW DATA REDUCTIONS
INTEGER RPM, RUN$
WRITE ($$FMT)$
      FORMAT FMT(B5,*MFLO*,B5,*RPM*,B3,*RHO IN*,B5,*NRF*,B10,*NRM*,B7,
      *NRM/NRF*,B3,*RUN*,W4)$
START..READ ($$DATA)$
      INPUT DATA(PATM,PD,PI,DPO,MVO,MVI,DM,RPM,DO,RUN)$
TOR = (SQRT(MVO + 9.081) - 2.899)/0.003567$
RO = 1.3207(PATM + PD)/(TOR + 459.7)$
MUO = 0.0399 + 0.0000605TOR$
EITHER IF DO GEQ 3.0$ GO BIG$
OTHERWISE$ GO LITL$
BIG..COMMENT 3.351 ORIFICES
      NRD = 6620(SQRT(DPO.RO))/MUO$
      LNRD = LOG(NRD)$
      KO = 0.757254 - 0.0175707LNRD + 0.000645328LNRD.LNRD$
      YO = 1.0 - 0.0234DPO/(PATM + PD)$
      MFLO = 4033KO.YO.DM.SQRT(DPO.RO)$
      GO OUT$
LITL..COMMENT 1.919 ORIFICES
      NRD = 2034(SQRT(DPO.RO))/MUO$
      LNRD = LOG(NRD)$
      KO = 0.692822 - 0.0152481LNRD + 0.000622632LNRD.LNRD$
      YO = 1.0 - 0.0218DPO/(PATM + PD)$
      MFLO = 1321KO.YO.DM.SQRT(DPO.RO)$
OUT..ZO = 0.07580$
TI = (SQRT(MVI + 9.081) - 2.899)/0.003567$
MUI = 0.0399 + 0.0000605TI$
NRF = MFLO/(ZO.MUI)$
RI = 1.3207(PATM + PI)/(TI + 459.7)$
NRM = 166.7RPM.RI/MUI$

```

WRITE (\$\$ANS,HDG)\$

OUTPUT ANS(MFLO,RPM,RI,NRF,NRM,NRM/NRF,RUN)\$

FORMAT HDG(X11.1,I7,X9.5,F13.5,F13.5,X9.4,I6,W4)\$

GO START\$

FINISH\$

2. Evaluation of Velocity Profiles

The following table gives the translation between the present nomenclature and that used in the computer program:

A	measured flow angle
ANG	flow angle relative to the radial direction
AO	protractor angle for radial flow
DPV	dynamic pressure as measured
DPVC	static pressure correction
MVV	temperature in millivolts
PATM	atmospheric pressure
PV	static pressure
ROV	density
TV	temperature in F
V	resultant velocity
VN	radial velocity component
VT	tangential velocity component

The machine program follows.

```

COMMENT VELOCITY PROFILES
INTEGER I,N,RUNS
ARRAY DPV(20), A(20)$
START..READ($$DATA)$
    INPUT DATA(RUN,PATM,PV,MVV,A0,N,DPVC,
        FOR I = (1,1,N)$DPV(I), FOR I = (1,1,N)$A(I))$
TV = (SQRT(MVV + 9.081) - 2.899)/0.003567$
ROV = 1.3207(PATM + PV)/(TV + 459.7)$
WRITE ($$ANS1,HDG1)$
    OUTPUT ANS1(RUN,ROV)$
    FORMAT HDG1(B5,*RUN*,I4,B5,*RHO **,*X7.5,B6,*VEL*,B5,*VTAN*,B5,
        *VRAD *,B4,*ANGLE*,W4)$
FOR I = (1,1,N)$
    BEGIN
        V = SQRT(334.88(DPV(I) + DPVC)/ROV)$
        ANG = A(I) - A0 - 8.25$
        VN = V.COS(0.0174533ANG)$
        VT = V.SIN(0.0174533ANG)$
        WRITE ($$ANS2,HDG2)$
            OUTPUT ANS2(V, VT, VN, ANG)$
            FORMAT HDG2(B33,X6.2,B3,X6.2,B3,X7.2,B3,X6.2,W4)$
    ENDS
GO START$
FINISH$

```

3. Evaluation of Average Heat Transfer

The average Stanton number was obtained from hand calculations. The heat meter temperatures were measured by the heat meter thermocouples. The heat meter calibration curves (Appendix E) were entered to obtain the heat meter calibration factor in $\frac{\text{BTU/hr ft}^2}{\text{mv}}$. The product of the heat meter output in millivolts and the calibration factor determined the heat flux passing through the heat meter. These heat fluxes were plotted as a function of r^2 (proportional to disk area) and the area average heat flux was obtained using a planimeter.

The average disk temperature was obtained as the numerical average of the five test surface thermocouple temperatures. This method was sufficiently accurate as the test surface thermocouples are located in the center of equal disk area sections and the temperature variation across the surface was within $\pm 1^\circ\text{F}$. The air inlet temperature was taken from the averaged readings of the four thermocouples equally spaced around the circumference of the air inlet passage.

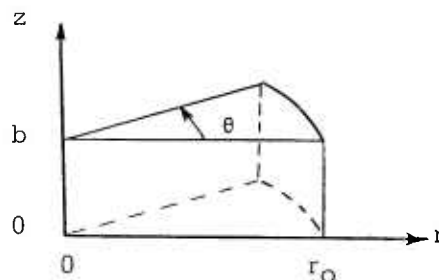
The average heat flux was divided by the temperature difference between the disk test surface and the inlet air to determine the average heat transfer coefficient. The average Stanton number is defined as:

$$N_{St} = \frac{q'' / (t_{disk} - t_{air in})}{\left(\frac{W}{2 \pi r_o z_o} \right) C_p}$$

Appendix D Local Heat Flux Data Reduction

The local Stanton numbers are obtained from the local values of test surface heat flux. The test surface heat flux can be related to the heat meter heat flux and the test surface temperature distribution by the solution for heat conduction through the disk. As this solution for the rotating disk boundary conditions is not available in the literature, it will be presented here.

The coordinate system and notation is:



For steady axisymmetric heat flow with isotropic thermal conductivity, the conduction equation is

$$\frac{\partial^2 t}{\partial r^2} + \frac{1}{r} \frac{\partial t}{\partial r} + \frac{\partial^2 t}{\partial z^2} = 0 \quad [D1]$$

The boundary conditions corresponding to the rotating disk test conditions are:

$$t(r, 0) = t_0 \left(\frac{r}{r_0} \right) = t_0(r^*) \quad [D2]$$

($t_0(r^*)$ is the experimentally determined test surface temperature distribution), and

$$\frac{\partial t}{\partial z}(r, b) = - \frac{q''_b \left(\frac{r}{r_0} \right)}{k} = - \frac{q''_b(r^*)}{k} \quad [D3]$$

$(q''_b(r^*))$ is the experimentally determined heat meter heat flux distribution), and

$$\frac{\partial t}{\partial r}(r_0, z) = 0 \quad [D4]$$

(there is no heat transferred through the outer edge of the disk) .

Assuming a product solution for $t(r, z)$,

$$t(r, z) = R(r) \cdot Z(z)$$

the variables $R(r)$ and $Z(z)$ may be separated, and two ordinary differential equations result.

$$\frac{R''}{R} + \frac{1}{r} \frac{R'}{R} = - \frac{Z''}{Z} = - \beta^2 \quad [D5]$$

where β^2 is a constant. Or:

$$R'' + \frac{1}{r} R' + \beta^2 R = 0 \quad [D6]$$

$$Z'' - \beta^2 Z = 0 \quad [D7]$$

The solution to [D 6] for a disk without a hole in the center is a Bessel function of the First Kind and zero order [(15), p. 39] :

$$R(r) = J_0(\beta r) \quad [D8]$$

The boundary condition at $r = r_0$ [D 4] is applied to obtain the eigenvalues. The Bessel function recursion relation is employed [(15), p. 31]:

$$\frac{d}{dx} J_0(x) = \frac{J_{-1}(x) - J_1(x)}{2} = -J_1(x) \quad [D9]$$

Therefore

$$\left. \frac{dR}{dr} \right|_{r_0} = \beta \left. \frac{d J_0(r \beta)}{d(r \beta)} \right|_{r_0} = - \beta J_1(r_0 \beta) = 0 \quad [D10]$$

The relation [D 10] is satisfied if $(r_0 \beta)$ takes on the values of

the zeros of $J_1(x)$. Denoting the zeros of $J_1(x)$ as α_m , the allowable values of β are:

$$\beta = \frac{\alpha_m}{r_0} \quad m = 0, 1, 2, \dots \quad [D11]$$

The solution [D 8] is then:

$$R(r) = J_0\left(\alpha_m \frac{r}{r_0}\right) = J_0(\alpha_m r^*) \quad [D12]$$

Eq. [D 7] can be directly integrated:

$$Z(z) = A_m e^{\alpha_m \frac{z}{r_0}} + B_m e^{-\alpha_m \frac{z}{r_0}} \quad [D13]$$

where A_m and B_m are constants of integration. The temperature distribution in the disk is thus given by:

$$t(r, z) = \sum_{m=0}^{\infty} J_0(\alpha_m r^*) \left[A_m e^{\alpha_m \frac{z}{r_0}} + B_m e^{-\alpha_m \frac{z}{r_0}} \right] \quad [D14]$$

This is the general solution for the axisymmetric temperature distribution in a circular disk with an insulated perimeter. The constants, A_m and B_m , are evaluated by applying the boundary conditions at the upper and lower surfaces. Applying the test (lower) surface boundary condition [D 2]:

$$t(r, 0) = t_0(r^*) = \sum_{m=0}^{\infty} J_0(\alpha_m r^*) (A_m + B_m) \quad [D15]$$

To evaluate each A_m and B_m , both sides of [D 15] are multiplied by $r^* J_0(\alpha_n r^*) dr^*$ and integrated from $r^* = 0$ to $r^* = 1$.

With n as the dummy variable of integration, [D 15] becomes:

$$\int_0^1 n t_0(n) J_0(\alpha_n n) dn = \sum_{m=0}^{\infty} (A_m + B_m) \int_0^1 n J_0(\alpha_n n) J_0(\alpha_m n) dn \quad [D16]$$

The Bessel function orthogonality relation is (15):

$$\int_0^1 n J_0(\alpha_n n) J_0(\alpha_m n) dn = \begin{cases} 0 & n \neq m \\ \frac{1}{2} [J_0(\alpha_m)]^2 & n = m \end{cases} \quad [D17]$$

Hence [D 16] can be written as:

$$\int_0^1 n t_0(n) J_0(\alpha_n n) dn = \frac{1}{2} (A_m + B_m) [J_0(\alpha_m)]^2 \quad [D18]$$

This is one relation for A_m and B_m . The other relation is similarly obtained by applying the heat meter (upper) surface boundary condition [D 3] :

$$\frac{\partial t}{\partial z}(r, b) = - \frac{q''_b(r^*)}{k} = \sum_{m=0}^{\infty} J_0(\alpha_m r^*) \frac{\alpha_m}{r_0} \left[A_m e^{\frac{\alpha_m b}{r_0}} - B_m e^{-\frac{\alpha_m b}{r_0}} \right] \quad [D19]$$

Multiplying both sides of [D 19] by $r^* J_0(\alpha_n r^*) dr^*$, integrating from $r^* = 0$ to $r^* = 1$, and using the orthogonality

relation [D.17] , yields:

$$- \int_0^l \eta \frac{q''_b(\eta)}{k} J_0(\alpha_m \eta) d\eta = \frac{\alpha_m}{2 r_0} \left[A_m e^{\alpha_m \frac{b}{r_0}} - B_m e^{-\alpha_m \frac{b}{r_0}} \right] \left[J_0(\alpha_m) \right]^2$$

[D20]

The two relations [D.18] and [D.20] can be solved for the constants A_m and B_m separately:

$$A_m = \frac{\left\{ e^{-\alpha_m \frac{b}{r_0}} \int_0^l \eta t_o(\eta) J_0(\alpha_m \eta) d\eta - \frac{r_0}{\alpha_m k} \int_0^l \eta q''_b(\eta) J_0(\alpha_m \eta) d\eta \right\}}{\left[J_0(\alpha_m) \right]^2 \cosh(\alpha_m \frac{b}{r_0})}$$

$$B_m = \frac{\left\{ e^{\alpha_m \frac{b}{r_0}} \int_0^l \eta t_o(\eta) J_0(\alpha_m \eta) d\eta + \frac{r_0}{\alpha_m k} \int_0^l \eta q''_b(\eta) J_0(\alpha_m \eta) d\eta \right\}}{\left[J_0(\alpha_m) \right]^2 \cosh(\alpha_m \frac{b}{r_0})}$$

[D21]

The heat flux at the test surface can now be evaluated. The test surface heat flux is obtained from the temperature distribution by:

$$q''_o(r^*) = -k \frac{\partial t(r, o)}{\partial z}$$

[D22]

or

$$q''_o(r^*) = 2 \sum_{m=0}^{\infty} \frac{J_0(\alpha_m r^*)}{\cosh(\alpha_m \frac{b}{r_o}) [J_0(\alpha_m)]^2} \int_0^1 \left[q''_b(n) - \frac{\alpha_m k}{r_o} \sinh(\alpha_m \frac{b}{r_o}) t_o(n) \right] n J_0(\alpha_m n) dn \quad [D23]$$

Recognizing that for $m=0$, $\alpha_o = 0$ and $J_0(0) = 1$, [D 23] becomes:

$$q''_o(r^*) = 2 \int_0^1 n q''_b(n) dn + 2 \sum_{m=0}^{\infty} \frac{J_0(\alpha_m r^*)}{\cosh(\alpha_m \frac{b}{r_o}) [J_0(\alpha_m)]^2} \int_0^1 \left[q''_b(n) - \frac{\alpha_m k}{r_o} \sinh(\alpha_m \frac{b}{r_o}) t_o(n) \right] n J_0(\alpha_m n) dn \quad [D24]$$

As n , the dummy variable of integration, is written for r^* , the first term can be written as:

$$2 \int_0^1 r^* q''_b(r^*) dr^* = \int_0^1 q''_b(r^*) d(r^*)^2$$

which is the area average heat flux passing through the disk. The remaining terms, then, average to zero. These two requirements provide a check on the numerical solution.

The Burroughs 220 digital computer was employed to solve [D 24] for given heat flux and temperature distributions. The program was entered with 21 values of both heat flux and temperature spaced at equal increments of r^* of 0.05. Values for r^* increments of 0.025 were obtained by linear interpolation. It was found necessary to limit the series summation to the first ten terms, as the integration inaccuracy became unacceptable for the higher terms. As explained in Section V, the present local heat transfer results are inordinately sensitive to uncertainties in the test surface temperature distribution. For this reason, the program was not modified for determination of the higher order terms.

The machine program has two procedures, or subsections. The first is a procedure developed for determining $J_0(x)$, and is labeled JOX. A series solution is used for x less than 10, and an asymptotic expansion for x greater than 10. The accuracy chosen is 0.01 per cent for x less than 10 and 0.1 per cent for x greater than 10. The second procedure performs the integration in [D 24], and is labeled INT. The integration scheme is a simple trapezoidal integration.

The following table gives the translation between the present nomenclature and that used in the computer program.

A	α_m , the zeros of $J_1(x)$
BRO	b/r_o , ratio of disk thickness to radius
COND	disk thermal conductivity
DR	increments of r^* for which the heat flux is to be determined
DS	increments of r^* for performing the numerical integration
ERR	allowable error in summing the series
ING	value of the integral in [D 24]
JO	$J_o(x)$
JOA	$J_o(\alpha_m)^2$
M	number of terms summed
N	number of data points entered
QB	$q_b''(r^*)$, heat meter section heat flux
QO	$q_o''(r^*)$, test surface heat flux
R	r^* at which heat flux is evaluated
RO	disk radius
RUN	Run number
TEO	$t_o(r^*)$, test surface temperature distribution

The machine program follows.


```

COMMENT EVALUATION OF QO BY SERIES$
INTEGER I,J,K,M,N,RUN$
ARRAY TIB(50), TEO(50), QB(50), ING(15)$
ARRAY A(10) = (0.0, 3.83171, 7.01559, 10.17347, 13.32369, 16.47063,
               19.61586, 22.76008, 25.90367, 29.04683)$
ARRAY JOA(10) = (1.0, 0.162215, 0.0900695, 0.0623525, 0.0476808,
               .0378901, 0.0324228, 0.0279507, 0.0245624, 0.0219081)$
PROCEDURE JOX(X$JO)$
BEGIN
  EITHER IF X LSS 10.0$ GO SML$
  OTHERWISE$ GO LRG$
  SML.. F = X.X/4$
      SUM1 = TRM = R = 1.0$
      UNTIL(ABS(TRM/SUM1) LSS 0.0001)$
      BEGIN
        TRM = -TRM.F/(R.R)$
        SUM1 = SUM1 + TRM$
        R = R + 1.0$
      ENDS$
  JO = SUM1$
  RETURNS$
  LRG.. JO = 0.79788(COS(X-0.7854) + (SIN(X-0.7854))/(8X))/SQRT(X)$
  RETURN END JOX()$
PROCEDURE INT(DS,N,Q(),A$$JOX($))$
  COMMENT INTEGRATION OF (S Q JO(A S))$
  BEGIN
    INTEGER I, N$
    EITHER IF A EQL 0.0$
      GO ALPHOS$
    OTHERWISE$
      GO ALPHMS$

```

```

ALPHO..SUMO = 0.5(Q(N))$
FOR I = (2,1,N-1)$
    SUMO = SUMO + (I-1)DS(Q(I))$
INT() = SUMO.DS$
RETURNS$
ALPHM..JOX(A$JO)$
SUMM = 0.5(Q(N))JO$
FOR I = (2,1,N-1)$
    BEGIN
        ARG = (I-1)(DS)A$
        JOX(ARG$JO)$
        SUMM = SUMM + (I-1)DS(Q(I))JO$
    ENDS$
    INT() = SUMM.DS$
RETURN END INT()$
COND = 72.0$ BRO = 0.2109$ RO = 0.6649$
START..READ($$DATA)$
INPUT DATA(DS,N,DR,M,ERR,RUN, FOR I = (1,1,N)$QB(I),
    FOR I = (1,1,N)$TEO(I))$
TERM1 = 2.INT(DS,N,QB(),0.0$$JOX($))$
WRITE ($$ANS1,HDG1)$
OUTPUT ANSI(TERM1)$
FORMAT HDG1(B5,*J = 1*,B24,*TERM = *,F12.6,W4)$
COMMENT COMPUTATION FOR R = 0$
SUMO = 0.0$ TERMO = TERM1$
I = 1$
FOR J = (2,1,10)$
    BEGIN
        SUMO = SUMO + TERMO$
        FOR K = (1,2,2N-1)$
            TIB(K) = QB((K+1)/2) - A(J).COND(SINH(A(J).BRO))

```

```

      TEO((K+1)/2)/RO$
FOR K = (2,2,2N-2)$
      TIB(K) = (TIB(K-1) + TIB(K+1))/2.0$
      ING(J) = INT(DS/2.0,2N-1,TIB(),A(J)$JOX($))$
      TERMO = 2(ING(J))/((JOA(J))COSH(BRO.A(J)))$
      WRITE ($$ANS2,HDG2)$

      OUTPUT ANS2(J,ING(J),TERMO)$

      FORMAT HDG2(B5,*J =*,I2,B3,*ING =*,F13.6,B3,
                *TERM =*,F13.6,W4)$

END$

QO = SUMO + TERMOS$
WRITE ($$ANS3,HDG3)$

OUTPUT ANS3(QO,RUN)$

FORMAT HDG3(B10,*R = 0*,B16,*QO =*,F13.6,B5,*RUN*,I4,W4)$

COMMENT COMPUTATION FOR R GREATER THAN 0$
FOR I = (2,1,M)$
  BEGIN
    SUMM = 0.0$   TERMM = TERM1$
    J = 1$
  ADD..SUMM = SUMM + TERMM$
  IF J EQL 11$ GO QUIT$
  EITHER IF ABS(TERMM/SUMM) GTR ERR$
  BEGIN
    ARG = (A(J))(1-1)DR$
    JOX(ARG$JO1$
    TERMM = 2JO.ING(J)/((JOA(J))COSH(BRO.A(J)))$
    WRITE ($$ANS4,HDG4)$

    OUTPUT ANS4(J,ING(J),TERMM)$

    FORMAT HDG4(B5,*J =*,I2,B3,*ING =*,F13.6,B3,
              *TERM =*,F13.6,W4)$

    J = J + 1$

```

```

        GO ADD$
        ENDS
    OTHERWISE$
QUIT..QO = SUMM$
        WRITE ($$ANS5,HDG5)$
        OUTPUT ANS5((I-1)DR,QO,RUN)$
        FORMAT HDG5(B10,*R =*,F8.2,B10,*QO =*,F13.6,
                    B5,*RUN*,I4,W4)$
    ENDS
GO START$
FINISH$

```

Appendix E Heat Meter Calibration

The heat meters used on the rotating disk are those manufactured by National Instrument Laboratories, Inc., Washington, D.C. The heat meter consists of a fine mesh copper screen bonded to either side of a silver-tellurium wafer. Copper leads are soldered to the screens. The temperature difference between the two copper and silver-tellurium junctions due to heat flow normal to the wafer produces a net EMF output proportional to the heat flux. The constant of proportionality must be determined experimentally. The nominal heat meter specifications are:

Catalog No.	HF - 1 - C
Diameter	0.400"
Thickness	0.060" - 0.065"
K (Calibration factor)	600 - 800 $\frac{\text{BTU/hr ft}^2}{\text{mv}}$
Thermal resistance	0.10 - 0.15 $\frac{\text{F}}{\text{BTU/hr ft}^2}$

The heat meters were calibrated after the disk was bonded together. The disk was inverted and placed over a 16" diameter electrical heater. A cooling flow of water was directed over the test surface (the upper surface during calibration). The direction of the heat flow through the disk was then the same for both calibration and testing. The disk heat flux was determined from the electrical power input to the heater. Energy balance tests

established the heat loss at less than 0.5 per cent. The relatively thick aluminum disks insured a uniform heat flux through the heat meter section (the protective disk was 0.375" thick during calibration and later machined to 0.065").

Model tests established that the heat meter output was not dependent on the temperature level of both junctions over the calibration range. The EMF - temperature relation is only slightly temperature dependent, and a single junction temperature characterized the heat meter output. The maximum operating temperature, dictated by the strength of the bond, is 170 F. The maximum calibration heat flux was 4000 BTU/hr ft².

The heat meter calibration factor is defined as the heat flux per millivolt of electrical output. The calibration factors for the disk heat meters are presented in Fig. E-1. For heat meters 1, 3, 4 and 5, the calibration factor varies linearly with temperature. The effect of temperature is slight; a 100 F rise decreases K by about 8 per cent.

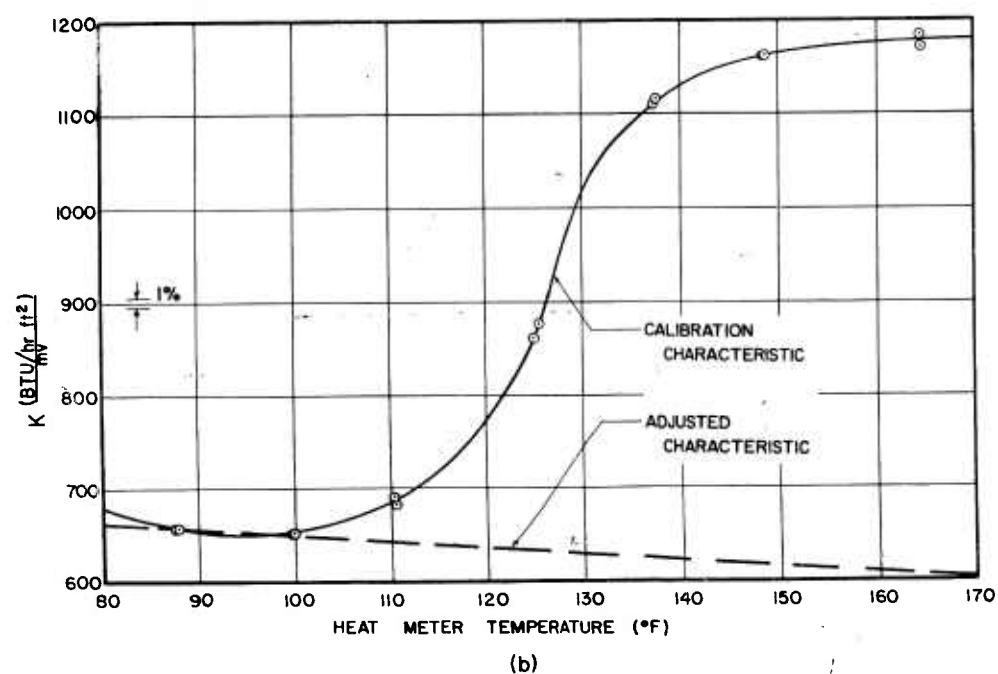
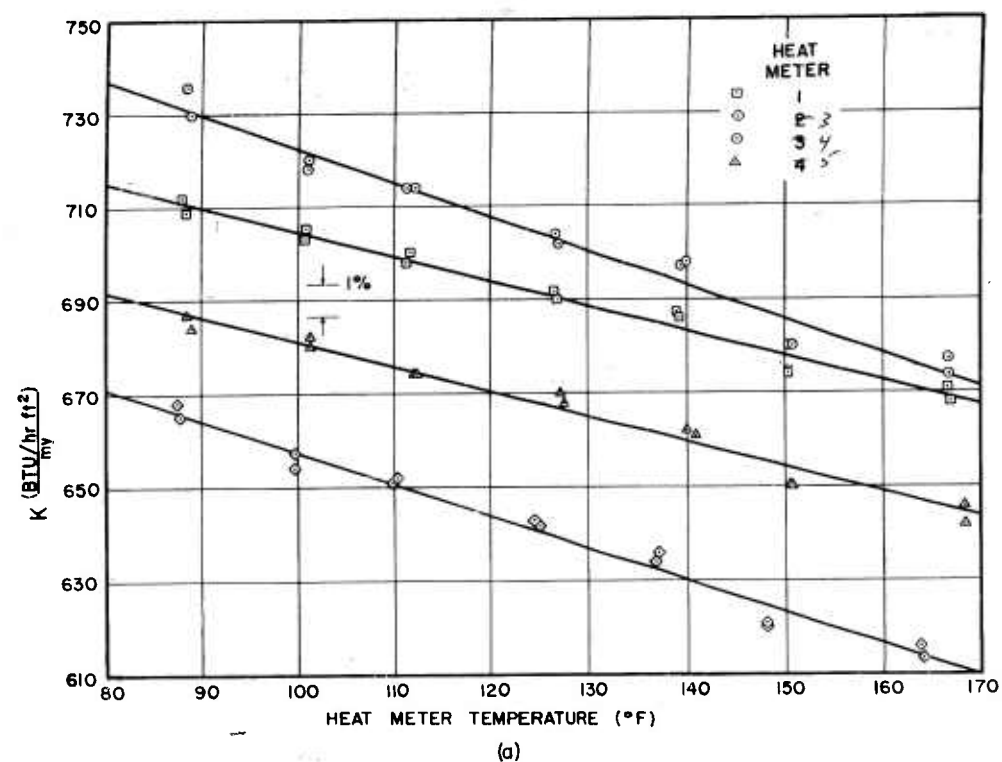
The nonlinear calibration for heat meter 2 can possibly be explained as the presence of a bond failure between the heat meter and the disk. At higher temperatures and/or heat fluxes, a gap between the heat meter and the disk might be produced by differential thermal expansion. The heat flux through the heat meter, and, consequently, the output of the heat meter, would be reduced,

yielding a higher value of K . This calibration did not appear to hold during testing, as the calculated heat flux was about twice that measured by any other heat meter. An adjusted characteristic passing through the two lowest temperature points was used. This gave heat fluxes in good agreement with those obtained by plotting the other heat fluxes as a function of radius and fairing a smooth curve through the data.

FIGURE E - 1

HEAT METER CALIBRATION FACTOR, K, AS A
FUNCTION OF HEAT METER TEMPERATURE

- (a) Heat Meters No. 1, 3, 4, and 5
- (b) Heat Meter No. 2



Appendix F Derivation of Integral Equations

The integral equations for the fluid dynamics and heat transfer from a rotating disk are derived from the governing differential equations. The major assumptions are:

1. The flow and heat transfer are steady and axisymmetric.
2. The fluid pressure is a function of radius only.
3. The fluid behaves as an uncompressed gas.
4. The flow is turbulent.
5. The heat transfer is in the axial (z) direction.

The governing differential equations are:

Continuity equation:

$$\frac{\partial u}{\partial r} + \frac{u}{r} + \frac{\partial w}{\partial z} = 0 \quad [F1]$$

Momentum equation in the radial direction:

$$\frac{g_c}{\rho} \frac{\partial \tau_r}{\partial z} - \frac{g_c}{\rho} \frac{dp}{dr} = u \frac{\partial u}{\partial r} + w \frac{\partial u}{\partial z} - \frac{v^2}{r} \quad [F2]$$

Energy equation:

$$-\frac{1}{\rho C_p} \frac{\partial q''}{\partial z} = u \frac{\partial t}{\partial r} + w \frac{\partial t}{\partial z} \quad [F3]$$

The boundary conditions are:

$$\text{At } z = 0: \quad u = 0, \quad v = r\omega, \quad w = 0, \quad \tau_r = \tau_{rw}$$

$$t = t_w, \quad q'' = q_w''$$

$$\text{At } z = \delta: \quad u = u_\delta, \quad v = v_\delta, \quad w = w_\delta, \quad \tau_r = 0$$

$$\text{At } z = \Delta: \quad t = t_\Delta, \quad q'' = 0$$

The continuity equation [F 1] is first integrated to evaluate the axial velocity component, w , at the edge of the hydrodynamic boundary layer, δ :

$$\int_0^{\delta} \left[\frac{\partial u}{\partial r} + \frac{u}{r} \right] dz + \int_0^{\delta} \frac{\partial w}{\partial z} dz = 0$$

or

$$w_{\delta} = - \int_0^{\delta} \frac{1}{r} \frac{\partial (r u)}{\partial r} dz \quad [F4]$$

Using the mathematical relation for differentiation under the integral sign, [F 4] can be written as:

$$w_{\delta} = - \frac{1}{r} \frac{d}{dr} \int_0^{\delta} r u dz - u_{\delta} \frac{d \delta}{dr} \quad [F5]$$

The momentum differential equation [F 2] is now integrated over the hydrodynamic boundary layer:

$$\begin{aligned} \int_0^{\delta} \frac{g_C}{\rho} \frac{\partial \tau_r}{\partial z} dz - \int_0^{\delta} \frac{g_C}{\rho} \frac{dp}{dr} dz = \\ \int_0^{\delta} u \frac{\partial u}{\partial r} dz + \int_0^{\delta} w \frac{\partial u}{\partial z} dz - \int_0^{\delta} \frac{v^2}{r} dz \end{aligned} \quad [F6]$$

Considering the terms separately and employing the boundary conditions:

$$\int_0^{\delta} \frac{g_C}{\rho} \frac{\partial \tau_r}{\partial z} dz = - \frac{g_C}{\rho} \tau_{rw} \quad [F7]$$

$$- \int_0^{\delta} \frac{g_C}{\rho} \frac{dp}{dr} dz = - \frac{g_C}{\rho} \frac{dp}{dr} \delta \quad [F8]$$

$$\int_0^\delta w \frac{\partial u}{\partial z} dz = w u|_\delta - w u|_0 - \int_0^\delta u \frac{\partial w}{\partial z} dz \quad [F9]$$

Using the continuity equation [F 1] and [F 5], [F 9] can be written as:

$$\begin{aligned} \int_0^\delta w \frac{\partial u}{\partial z} dz &= - \frac{u_\delta}{r} \frac{d}{dr} \int_0^\delta r u dz - \\ &u_\delta^2 \frac{d\delta}{dr} + \int_0^\delta \frac{u}{r} \frac{\partial (r u)}{\partial r} dz \end{aligned} \quad [F10]$$

[F 6] can then be written as:

$$\begin{aligned} - \frac{g_c}{\rho} \left[r_w + \delta \frac{dp}{dr} \right] &= \int_0^\delta \left[u \frac{\partial u}{\partial r} + u \frac{\partial (r u)}{\partial r} \right] dz \\ &- \frac{u_\delta}{r} \frac{d}{dr} \int_0^\delta r u dz - u_\delta^2 \frac{d\delta}{dr} - \int_0^\delta \frac{v^2}{r} dz \end{aligned} \quad [F11]$$

The first integral on the right hand side can be combined:

$$\int_0^\delta \left[u \frac{\partial u}{\partial r} + \frac{u}{r} \frac{\partial (r u)}{\partial r} \right] dz = \int_0^\delta \frac{1}{r} \frac{\partial (r u^2)}{\partial r} dz \quad [F12]$$

Again using the relation for differentiation under the integral sign:

$$\int_0^\delta \frac{1}{r} \frac{\partial (r u^2)}{\partial r} dz = \frac{1}{r} \frac{d}{dr} \int_0^\delta r u^2 dz + u_\delta^2 \frac{d\delta}{dr} \quad [F13]$$

Employing [F 13], the integral momentum equation becomes:

$$-\frac{g_c}{\rho} \left[\tau_{rw} + \delta \frac{dp}{dr} \right] = \frac{1}{r} \frac{d}{dr} \int_0^\delta r u^2 dz + \frac{u_\delta}{r} \frac{d}{dr} \int_0^\delta r u dz - \int_0^\delta \frac{v^2}{r} dz \quad [F14]$$

Normalizing the coordinates and δ by the disk radius yields:

$$-\frac{g_c}{\rho} \left[\tau_{rw} + \delta^* \frac{dp}{dr^*} \right] = \frac{1}{r^*} \frac{d}{dr^*} \int_0^{\delta^*} r^* u^2 dz^* + \frac{u_\delta}{r^*} \frac{d}{dr^*} \int_0^{\delta^*} r^* u dz^* - \int_0^{\delta^*} \frac{v^2}{r^*} dz^* \quad [F15]$$

The energy integral equation is obtained by integrating the energy differential equation [F 3] over the thermal boundary layer:

$$-\int_0^\Delta \frac{1}{\rho C_p} \frac{\partial q''}{\partial z} dz = \int_0^\Delta u \frac{\partial t}{\partial r} dz + \int_0^\Delta w \frac{\partial t}{\partial z} dz \quad [F16]$$

Considering the terms separately:

$$-\int_0^\Delta \frac{1}{\rho C_p} \frac{\partial q''}{\partial z} dz = \frac{q''_w}{\rho C_p} \quad [F17]$$

$$\int_0^\Delta w \frac{\partial t}{\partial z} dz = w(t)_\Delta - w(t)_0 - \int_0^\Delta t \frac{\partial w}{\partial z} dz \quad [F18]$$

Using the continuity equation [F 1] , [F 4] and the boundary conditions to eliminate w_{Δ} , [F 18] becomes:

$$\int_0^{\Delta} w \frac{\partial t}{\partial z} dz = - t_{\Delta} \int_0^{\Delta} \frac{1}{r} \frac{\partial(r u)}{\partial r} dz + \int_0^{\Delta} \frac{t}{r} \frac{\partial(r u)}{\partial r} dz \quad [\text{F19}]$$

This allows [F 16] to be written as:

$$\begin{aligned} \frac{q''_w}{\rho C_p} &= \int_0^{\Delta} \left[u \frac{\partial t}{\partial r} + t \frac{\partial(r u)}{\partial r} - t_{\Delta} \frac{\partial(r u)}{\partial r} \right] dz \\ &= \int_0^{\Delta} \frac{1}{r} \frac{\partial}{\partial r} \left[r u (t - t_{\Delta}) \right] dz \quad [\text{F20}] \end{aligned}$$

Again using the relation for differentiation under the integral sign:

$$\frac{q''_w}{\rho C_p} = \frac{1}{r} \frac{d}{dr} \int_0^{\Delta} r u (t - t_{\Delta}) dz - \left[r u (t - t_{\Delta}) \right]_{\Delta} \frac{d\Delta}{dr}$$

or

$$\frac{q''_w}{\rho C_p} = \frac{1}{r} \frac{d}{dr} \int_0^{\Delta} r u (t - t_{\Delta}) dz \quad [\text{F21}]$$

Normalizing the coordinates and Δ with the disk radius yields

the energy integral equation:

$$\frac{q''_w}{\rho C_p} = \frac{1}{r^*} \frac{d}{dr^*} \int_0^{\Delta^*} r^* u (t - t_{\Delta}) dz^* \quad [\text{F22}]$$

TECHNICAL REPORTS DISTRIBUTION LIST, CONTRACT Nonr 225(23)

[illegible]

TECHNICAL REPORTS DISTRIBUTION LIST. CONTRACT Nonr 225(23)

Aerojet-General Corp. Liquid Engine Division Azusa, California (1) Attn: Mr. C. C. Ross	Argonne National Labs. 9700 S. Cass Ave. Argonne, Illinois (1) Attn: Tech. Library (1) Dr. B. I. Spinrad, Dir. Res. Engrg. (1) Dr. David Miller, ISNE School (1) Mr. N. J. Petrick	Sanderford and Porter 72 Wall Street New York 5, New York (1) Attn: Mr. S. T. Robinson	The Trans Company 2nd and Cameron Avenues La Crosse, Wisconsin (2) Attn: Mr. H. C. Rooks (1) Mr. J. T. McE221
Aerojet-General Nucleonics Postoria Way San Ramon, California (1) Attn: Library (1) Dr. D. L. Cochran (1) Mr. A. V. Lissin	Arnold Equipment Corp. 3080 Main Street Buffalo, New York (1) Attn: Mr. R. G. Tesamer	Shell Development Company Emeryville, California (1) Attn: Dr. C. R. Garbett	Union Carbide Nuclear Co. Oak Ridge Gaseous Diffusion Plant Plant Records Department P. O. Box P Oak Ridge, Tennessee
The Air Preheater Corp. Wellsville, New York (1) Attn: Mr. Hilmer Karlsson Technical Manager	Aro, Inc. Technical Information Branch Tullahoma, Tennessee (1) Attn: Mr. G. E. Randall	Solar Aircraft Company San Diego, 12, California (1) Attn: Mr. P. A. Pitt, Chief Engineer (1) Mr. E. A. Drury Project Engineer	United Aircraft Corp. 400 Main Street East Hartford 8, Conn. (1) Attn: Mr. Robert C. Sele Chief Librarian Mr. Ned C. Rice, Jr. Research Dept.
Airesearch Mfg. Company 9551 9551 Sepulveda Blvd. Los Angeles, 35, California (2) Attn: Mr. S. K. Andersen (1) Dr. J. E. Coppage (1) Mr. A. L. Johnson, Jr. (1) Dr. John Mason	Atlantic Research Corporation Alexandria, Virginia (1) Attn: Dr. M. Markels, Jr.	Stalker Development Company 903 Woodside Avenue Beverly Hills, California (1) Attn: Mr. E. A. Stalker	Vidya Inc. 2626 Hanover Street Palo Alto, Calif. (1) Attn: M. W. Rubelin (1) D. E. Abbott (1) D. C. Briggs
Fairchild Engine and Airplane Corporation Fairchild Astrionics Div. Wyandanch, Long Island, N.Y. (1) Attn: Alex London, Sr., Engineer, Aero Mechanics Div.	General Electric Company General Engineering Lab. Schenectady, 5, New York (1) Attn: Mr. P. F. Buckland (1) Dr. R. H. Norris Thermal Systems Engrg. (1) D.H. Brown Thermal Systems Engrg.	Stanford Research Institute Menlo Park, California (1) Attn: Dr. Nevin K. Hiester (1) Mr. S. H. Clark (1) Mr. W. A. Gasler	Western Supply Co. P. O. Box 1388 Tulsa, 1, Oklahoma (1) Attn: E. D. Anderson.
Fairchild Engine and Airplane Corp. Stratos Division Bay Shore, Long Island, N.Y. (1) Attn: Mr. V.L. Whitney, Jr. Res. Engineer	General Electric Company Design Section, Engrg. Dept. Richland, Washington (1) Attn: Mr. Gardner L. Locke	Worthington Corp. Harrison Division Harrison, New Jersey (1) Attn: Mr. Norman L. Myerson, Dir. of Research (1) Mr. David Aronson	(1) Dr. Robert W. Fox Dept. of Mech. Engrg. Purdue University Lafayette, Indiana
Petrotherm Company 1801 E 65th Street Cleveland, 3, Ohio (2) Attn: Mr. Sven Holm	General Electric Company Small Aircraft Engine Dept. 1000 Western Avenue West Lynn 3, Mass. (1) Attn: Paul C. Setze	Young Radiator Company 709 S. Marquette St. Racine, Wisconsin (1) Attn: Mr. H. P. Brinen Res. Engineer	(1) Mr. Ralph M. Heintz P. O. Box 540 Los Gatos, Calif
Ford Motor Company Dearborne, Michigan (1) Attn: Mr. Paul Klotsch Res. Div. (1) Dr. D. N. Frey Scientific Lab. (1) Mrs. Rachel MacDonald Eng. Staff Library (1) Mrs. L. B. Phillips Superintendent Tech. Info. Sec. Scientific Lab.	General Motors Corp. Allison Division Indianapolis, 6, Indiana (1) Attn: Mr. R.M. Haxson Dir. of Engrg.	(1) Mr. Hector H. Alken 904 Willow Road Menlo Park, Calif. (1) Dr. W. B. Boley Hope Ranch Santa Barbara, Calif. (1) Mr. P. A. Brooks Dept. of Agr. Engrg. Univ. of Calif. Agr. Experiment Station Davis, California	(1) Mr. Albert L. Holliday 550 Lakewood Circle Walnut Creek, Calif. (1) Mr. Robert V. Kleinachmidt 20 East Street Stoneham, 80, Mass. (1) Dr. Milton B. Larson Dept. of Mech. Engrg. Oregon State College Corvallis, Oregon
Poster-Wheeler Corp. 666 Fifth Avenue New York, 6, N.Y. (1) Attn: Mr. John Elizard, Res. Consultant	General Motors Corp. Research Laboratories 12 Mile and Mound Roads Warren, Michigan (2) Attn: Mr. W. A. Turunen, Gas Turbine Dept. (1) Dr. V. C. Smith	(1) Prof. Alberto Coimbra Escola Nacional de Quimica Av. Pasteur 404 Rio De Janeiro, BRASIL (1) Mr. W. H. Comtois 129 Thornberry Drive Pittsburgh, 25, Pa. (1) Mr. Paul Dawson 8320 East Galbraith Cincinnati, 13, Ohio (1) Mr. A. J. Ede Heat Division Mech. Eng. Research Lab. D.S. I.R., East Kilbride Near Glasgow, SCOTLAND SEND TO: Office of the Asst. Naval Attache for Research Naval Attache, American Embassy Navy No. 100, Fleet P.O. New York, New York	(1) Rear Adm. Paul F. Lee, SEN Ret. 14975 Manuella Avenue Los Altos, California (1) Mr. E. J. Le Fevre Dept. of Mechanical Engineering Queen Mary College London E. 1., ENGLAND (1) Mr. Alex London Space Systems Thermal Analysis General Electric Company 3198 Chestnut Street Philadelphia 1, Pa. (2) Mr. R. B. Lundberg Stanford Research Institute Menlo Park, California
The Franklin Institute Laboratories for Research and Development Philadelphia, 3, Pa. (1) Attn: Mr. P. L. Jackson	General Dynamics Corp. General Atomic Division P.O. Box 608 San Diego, 10, Calif. (1) Attn: F. W. Simpson, Document Custodian	(1) Mr. A. J. Ede Heat Division Mech. Eng. Research Lab. D.S. I.R., East Kilbride Near Glasgow, SCOTLAND SEND TO: Office of the Asst. Naval Attache for Research Naval Attache, American Embassy Navy No. 100, Fleet P.O. New York, New York	(1) Dr. J. J. McMullen Mech. Eng. Research Lab. 1114 Clinton Street Hoboken, New Jersey (1) Mr. Frank L. Maker 156 Moraga Highway Orinda 1, California (1) Prof. J. W. Mitchell University of Wisconsin Dept. of Mechanical Engineering Madison 6, Wisconsin (1) Mr. Edward Simons 355 Taraval Street San Francisco 16, California (1) Mr. S. B. Spangler, Jr. 4315 Miranda Avenue Palo Alto, California (1) Mr. Richard L. Stone William Wallace Company Belmont, California (1) Mr. John Cook Wyllie Alderman Library University of Virginia Charlottesville, Virginia (1) Mr. Stanley Wong 1128 West 126th Street Los Angeles 44, California (1) Dr. J. O. Woodroff, Chairman Food Processing Division Georgia Experimental Station Experiment, Georgia (1) Prof. F. L. Schwartz Dept. of Mechanical Engineering University of Florida Gainesville, Florida AMC (AFRC) (1) Attn: RRLA-Library Wright-Patterson AFB Ohio (1) AFIT (AU) (1) Attn: MLI Library Wright-Patterson AFB Ohio (1) AMC (1) Attn: Library Wright-Patterson AFB Ohio (1) David Taylor Model Basin Aerodynamics Laboratory Attn: Library Washington 7, D.C.
Jack and Heintz, Inc. Engineering Dept., Plant 4 Cleveland, 1, Ohio (1) Attn: Mrs. Harriet B. Trinkl Librarian	Mine Safety Appliances Co. Callery Plant Callery, Pennsylvania (1) Attn: Dr. E. B. Jackson	(1) Prof. R. W. Stuart Mitchell Laboratorium Voor Verbrandingsmotoren en Gasturbines Technische Hogeschool Prof. Mekelweg 2 Delft, HOLLAND (1) Dr. Carl A. Moore, Jr. 3307 Sunnywood Drive Fullerton 1, California (1) Mr. A. W. Morris University of Texas Austin, Texas (1) Mr. A. J. Oberg Minneapolis-Honeywell Regulator Company Research Center 500 Washington Avenue, S. Hopkins, Minnesota (1) Mr. R. C. Perrell 5853 Whitefox Drive Palos Verdes Estates California (1) Major Walter E. Rafert Asst. Prof. - Armament Department of Ordnance U.S. Military Academy West Point, New York (1) Mr. D. W. Retzinger Perflex Corporation Heat Transfer Products 500 West Oklahoma Avenue Milwaukee 7, Wisconsin (1) Mr. L. P. Saunders P.O. Box L Carmel, California (1) Mr. Wolfgang Schaechter Thiokol Chemical Corporation Rocket Operations Center P.O. Box 1640 Ogden, Utah (1) Mr. David M. Schoenfeld Marion Road New Canaan, Connecticut	
General Electric Company Atomic Power Equipment Div. San Jose, California (1) Attn: W. A. Sutherland (1) F. E. Tippette	General Motors Corp. Harrison Radiator Div. Lockport, New York (2) Attn: Mr. John W. Godfrey		
Jack and Heintz, Inc. Engineering Dept., Plant 4 Cleveland, 1, Ohio (1) Attn: Mrs. Harriet B. Trinkl Librarian	Mine Safety Appliances Co. Callery Plant Callery, Pennsylvania (1) Attn: Dr. E. B. Jackson		
M. W. Kellogg Company 711 Third Avenue New York, 17, New York (1) Attn: Mr. F. W. Peterson (1) Mr. G. P. Eschenbrenner (1) Mr. Ronald B. Smith, Vice President	Morgantown Research Center Bureau of Mines Morgantown, West Virginia (1) Attn: Mr. J. F. Modes		
The Kraissl Co., Inc. 227 Williams Avenue Hackensack, New Jersey (1) Attn: Mr. P. Kraissl, Jr.	North American Aviation, Inc. International Airport Los Angeles, 45, Calif. (1) Attn: Mr. M. A. Sulkin		
Lockheed Aircraft Co. Burbank, California (1) Attn: B. L. Messinger Engrg. No. 7225	Perflex Corporation 500 West Oklahoma Avenue Milwaukee, 7, Wisconsin (1) Attn: Mr. W. W. Schmid (1) Mr. G. Hazeloop Res. Dev. Engineer		
Stewart-Warner Corp. 1514 Drower Street Indianapolis 7, Indiana (2) Attn: Mr. R. D. Randall Mgr. Research	Westinghouse Electric Corp. Lester Branch P.O. Philadelphia 13, Pa. (1) Attn: Mr. F. K. Fischer, Mgr. Dev. Engrg.		
Sulzer Bros. Ltd. 50 Church Street New York 7, New York (1) Attn: Mr. Richard Herold	Westinghouse Electric Corp. Atomic Power Division P. O. Box 1466 Pittsburgh, 30, Pa. (1) Attn: Technical Library		
Sverdrup and Parcel, Inc. Syndicate Trust Bldg. St. Louis, 1, Missouri	Westinghouse Electric Corp. Research Laboratory East Pittsburgh, Pa. (1) Attn: Dr. Stewart Way		
Sylvania Electric Products, Inc. Electronics Defense Lab. P.O. Box 205 Mountain View, California (1) Attn: Library	Volverine Tube Division 1411 Central Avenue Detroit, 9, Michigan (1) Attn: Mr. F. C. Eddens		
Texas Eastern Transmission Corp. P.O. Box 1612 Shreveport, Louisiana (1) Attn: Mr. C. W. Marvin			